PTB bericht
Wissenschaftliche Veröffentlichungen

Diss-29
April 2026

# Dissertation

Souvaraj De

# Processing of high bandwidth signals with photonic integrated circuits

ISSN 2941-1297
ISBN 978-3-944659-61-9

DOI 10.7795/110.20260421B

Souvaraj De

# Processing of high bandwidth signals with photonic integrated circuits

Dissertation

PTB-Diss- 29

Braunschweig, 21. April 2026

ISSN 2751-6598
ISBN 978-3-944659-61-9

DOI 10.7795/110.20260421B

**Empfohlene Zitierweise/recommended citation**

De, S., 2026. *Processing of high bandwidth signals with photonic integrated circuits*,
Technische Universität Carolo-Wilhelmina zu Braunschweig.
Braunschweig: Physikalisch-Technische Bundesanstalt.
PTB-Bericht Diss-29. ISBN 978-3-944659-61-9.
Verfügbar unter: https://doi.org/10.7795/110.20260421B

**Herausgeber:**
Physikalisch-Technische Bundesanstalt
ISNI: 0000 0001 2186 1887

**Presse und Öffentlichkeitsarbeit**

Bundesallee 100
38116 Braunschweig

Telefon: (05 31) 592-93 21
Telefax: (05 31) 592-92 92
www.ptb.de

# Processing of high bandwidth signals with photonic integrated circuits

Von der Fakultät für Elektrotechnik, Informationstechnik, Physik
der Technischen Universität Carolo-Wilhelmina zu Braunschweig

zur Erlangung des Grades eines Doktors
der Ingenieurwissenschaften (Dr.-Ing.)

genehmigte Dissertation


| | |
|---|---|
| von: | Souvaraj De |
| aus: | Kailashahar, Tripura, Indien |
| Eingereicht am: | 23te. October 2025 |
| Mündliche Prüfung am: | 16te. März 2026 |

1. Referent: Prof. Dr. rer. nat. Thomas Schneider, Technische Universität Braunschweig
2. Referent: Prof. Dr.-Ing. Thomas Kleine-Ostmann, PTB Braunschweig
3. Referent: Prof. Dr.-Ing. Kambiz Jamshidi, Technische Universität Dresden



Druckjahr: 2026

https://doi.org/10.7795/110.20260421B

https://doi.org/10.7795/110.20260421B

# Abstract

The modern world has witnessed a rapid upsurge in the demand for high data rate transmission to support the contemporary technologies and numerous applications such as high-speed global networking, Internet of Things (IoT), etc. across multiple domains including artificial intelligence, machine learning, and cloud services. This demand is expected to only grow exponentially in the coming years, easing the advance of sixth-generation (6G) communications and beyond. Nevertheless, using the electrical domain to process such high-bandwidth signals would be challenging owing to its shortcomings like restricted bandwidth, latency problems, high power consumption, cost, and complexity, and vulnerability to electromagnetic interference (EMI).

Using silicon photonics, it is possible to implement optical signal processing which offers a wider bandwidth, relatively simpler implementation, increased flexibility, low latency and immunity to EMI and environmental radiation. Moreover, with the silicon-on-insulator (SOI) platform in integrated silicon photonics, it is possible to make use of the popular complementary metal oxide semiconductor (CMOS) technology. Optical communication has improved massively as a result of the combination of electronics and photonics on the silicon photonics platform. However, the thermal conductance of the chip constituents leads to thermal crosstalk which reduces the system performance, especially in densely-packed photonic integrated circuits.

This thesis delves into the three fundamental aspects of high-bandwidth signal processing using photonic integrated circuits (PICs), namely, the generation of Nyquist pulse sequences, direct detection (DD) based orthogonal sampling, and thermal crosstalk alleviation. It begins with the generation of sinc-shaped Nyquist pulse sequences with optical frequency combs (OFCs) using Mach-Zehnder modulators. Analysis of practical impairments like comb ripple, unwanted sidebands, and optical filter roll off in the process of sinc-shaped Nyquist pulse sequence synthesis is carried out for three-line, five-line, and nine-line OFCs. This is followed by the performance evaluation of a DD based orthogonal sampling system under the presence of non-idealities and comparison with the conventional DD system with electronic analog to digital converters. Finally, the thesis explains the issue of thermal crosstalk and provides mitigation techniques to minimize the same in PICs.

All in all, this thesis lays a comprehensive and practical groundwork for developing thermally



https://doi.org/10.7795/110.20260421B

efficient, scalable, and metrologically precise photonic systems capable of performing high bandwidth signal processing.



https://doi.org/10.7795/110.20260421B

# Kurzfassung

Die moderne Welt erlebt einen rasanten Anstieg der Nachfrage nach Hochgeschwindigkeitsübertragungen zur Unterstützung moderner Technologien und zahlreicher Anwendungen wie globaler Hochgeschwindigkeitsnetzwerke, dem Internet der Dinge (IoT) und anderen in verschiedenen Bereichen, darunter künstliche Intelligenz, maschinelles Lernen und Cloud-Dienste. Es wird erwartet, dass dieser Bedarf in den kommenden Jahren exponentiell wächst und die Entwicklung der sechsten Mobilfunkgeneration (6G) und darüber hinaus vorantreibt. Die Nutzung des elektrischen Bereichs zur Verarbeitung solch breitbandiger Signale wäre jedoch aufgrund von Nachteilen wie eingeschränkter Bandbreite, Latenzproblemen, hohem Stromverbrauch, hohen Kosten, Komplexität und Anfälligkeit für elektromagnetische Störungen (Electromagnetic Interference - EMI) eine Herausforderung.

Mithilfe der Siliziumphotonik ist die optische Signalverarbeitung realisierbar. Diese bietet eine größere Bandbreite, eine vergleichsweise einfache Implementierung, erhöhte Flexibilität, geringe Latenzzeiten und Unempfindlichkeit gegenüber elektromagnetischen Störungen und Umwelteinstrahlung. Darüber hinaus ermöglicht die SOI-Plattform (Silicon-on-Insulator) in der integrierten Siliziumphotonik die Nutzung der gängigen CMOS-Technologie (Complementary Metal Oxide Semiconductor). Die optische Kommunikation hat sich durch die Kombination von Elektronik und Photonik auf der Siliziumphotonik-Plattform deutlich verbessert. Die Wärmeleitfähigkeit der Chipkomponenten führt jedoch zu thermischem Übersprechen, das die Systemleistung insbesondere bei dicht gepackten photonischen integrierten Schaltkreisen reduziert.

Diese Arbeit befasst sich mit drei grundlegenden Aspekten der Signalverarbeitung mit hoher Bandbreite mithilfe von photonisch integrierten Schaltkreises (PICs): der Erzeugung von Nyquist-Pulssequenzen, der orthogonalen Abtastung auf Basis von Direktdetektion (DD) und der Reduzierung von thermischem Übersprechen. Sie beginnt mit der Erzeugung von sincförmigen Nyquist-Pulssequenzen mit optischen Frequenzkämmen (OFCs) unter Verwendung von Mach-Zehnder-Modulatoren. Die Analyse praktischer Beeinträchtigungen wie Kammwelligkeit, unerwünschter Seitenbänder und optischer Filterabfall bei der Synthese von sincförmigen Nyquist-Pulssequenzen wird für drei-, fünf- und neunlinige OFCs durchgeführt. Anschließend folgt die Leistungsbewertung eines auf DD basierenden orthogonalen Abtastsystems unter Berücksichtigung von Nichtidealitäten und ein Vergleich mit dem konventionellen DD-



https://doi.org/10.7795/110.20260421B

System mit elektronischen Analog-Digital-Wandlern. Abschließend erläutert die Arbeit das Problem des thermischen Übersprechens und bietet Abhilfemaßnahmen zu dessen Minimierung in PICs.

Alles in allem legt diese Arbeit eine umfassende und praktische Grundlage für die Entwicklung thermisch effizienter, skalierbarer und metrologisch präziser photonischer Systeme, die eine Signalverarbeitung mit hoher Bandbreite ermöglichen.



https://doi.org/10.7795/110.20260421B

# Acknowledgments

First and foremost, I want to extend my heartfelt gratitude to both of my advisors, Prof. Dr. Thomas Schneider and Prof. Dr. Thomas Kleine-Ostmann, for their guidance, wisdom, constant encouragement, and elaborate support throughout my Ph.D. journey. I am extremely grateful that they gave me the freedom to work at both the Terahertz Photonics Group (TPG) at TU Braunschweig and also at the Department of High Frequency and Electromagnetic Fields at Physikalisch-Technische Bundesanstalt (PTB) Braunschweig.

I am immensely grateful to Dr. Ranjan Das for his invaluable guidance and support right from the period I started my research as a master's student at TPG in TU Braunschweig. His passion for research motivated me to work harder and fostered my interest in Silicon photonics.

I sincerely appreciate the member of my doctoral committee, Prof. Dr.-Ing. Kambiz Jamshidi, for his valuable insights, constructive criticism, encouragement, and taking his valuable time to evaluate my work. I am very grateful to Prof. Dr.-Ing. Thomas Küerner, who generously accepted to chair the examination committee. I would like to thank Prof. Dr. J Christoph Scheytt of Paderborn University and Prof. Dr. Linjie Zhou of Shanghai Jiao Tong University for their collaboration. I am indebted to the financial support provided by the German Research Foundation (DFG) through the Meteracom project. Special thanks go to the German Academic Exchange Service (DAAD) for allowing me to do my master thesis in Germany.

I greatly appreciate the support of my colleagues at the THz Photonics Group throughout my Ph.D. journey. I am grateful to our former colleagues Dr.-Ing Stefan Preußler, Dr. Karanveer Singh, Dr. Arijit Misra, and Dr. Cheng Feng for their support in the laboratory, discussions, and guidance. I am immensely grateful to Dr. Janosch Meier, Dr. Younus Mandalawi, Dr. Khaleda Mallick, Deepanshu Yadav, and Abhinand Venugopalan for their help, fruitful discussions, and a memorable time at the university.

I am grateful to my colleagues at the Department of High Frequency and Electromagnetic Fields at Physikalisch-Technische Bundesanstalt (PTB) Braunschweig for their support. I would like to thank Dr. Nora Meyne and our group leader, Dr.-Ing. Kai Baaske for the fruitful discussions and support in the Waveform Metrology meetings. I want to thank Mohanad Al-Dabbagh, David Ulm, and Tessina Kotschy-Scholz for their support and help. I extend my sincere gratitude to Prof. Dr. Ravendra K. Varshney from IIT Delhi, who introduced me to the world of photonics.

Finally, I am deeply grateful to my family and friends for their love, support, and constant



https://doi.org/10.7795/110.20260421B

words of encouragement throughout the journey.

Furthermore, I want to acknowledge the use of AI-assisted tools, including ChatGPT, that provided me with a lot of support in refining the language and polishing the grammar in the thesis writing process. These tools were merely utilized for improving the readability of the thesis and not to develop the scientific content of the thesis.



https://doi.org/10.7795/110.20260421B

# Contents





https://doi.org/10.7795/110.20260421B

https://doi.org/10.7795/110.20260421B

# 1 Introduction

Over the last few decades, the world has witnessed a tremendous growth in data-intensive applications, including high-speed communications, advanced sensing, and real-time signal processing [1–3]. Even for emerging fields such as quantum computing, edge computing, autonomous systems, and biological monitoring, there is an immense demand for faster and more efficient signal processing technologies, owing to the colossal amount of data flowing worldwide [4, 5]. Global internet traffic is growing at an exponential pace each year and will continue to do so in the upcoming years [6]. Consequently, the rising demand for bandwidth-intensive applications has put huge pressure on the current network infrastructure, especially the physical hardware accountable for the algorithmic tasks.

The conventional electrical signal processing is vital for supporting the current infrastructure. With the help of useful techniques like digital signal processing (DSP), Fourier Transform (FT), Fast Fourier Transform (FFT), machine learning, etc, it is possible to have advanced operability like error correction, quantum or homomorphic encryption, lossy data compression, data masking which further enhances data security, efficiency, and reliability [7–9]. As a result, the quality of signal transmission and reception is vastly improved. Nevertheless, traditional electrical systems are limited by finite bandwidth, high power consumption, noticeable signal deterioration over a transmission line, system latency, and susceptibility to electromagnetic interference (EMI) [10, 11].

In this context, the optical signal processing offers a much higher bandwidth than the traditional electrical methods [12, 13]. The data processing and data transmission occur at a faster pace as the light waves can transport a vast quantity of information at the same time, thus resulting in fast and effective data processing and transmission. It is also suitable for long-haul communication, as the optical fibers can transmit signals over a long distance without any major signal deterioration [14]. Optical devices are best suited for easy-to-carry and space-efficient applications, as they are small-scale and low-weight [15]. Further advantages include immunity to EMI [16], lesser power consumption, multifunctionality, better noise immunity, and most importantly, the integration with photonic devices on photonic integrated circuits (PIC) based on the silicon photonics technology [17].

The silicon photonics technology is also compatible with the popular, scalable, and mature complementary metal oxide semiconductor (CMOS) fabrication process, which facilitates the



https://doi.org/10.7795/110.20260421B

integration of electronic and optical components on the same chip [18]. Consequently, this technology allows for the development of compact, functional, energy-efficient, and high-speed photonic devices for numerous applications, particularly in data communication, sensing, and signal processing. Additionally, it makes it possible to process signals at high frequencies, even at the terahertz (THz) range [19]. A typical photonic system includes electro-optic (E/O) converters to perform all-optical signal processing with PICs, after which the signal is converted back into the electrical domain using opto-electric (O/E) converters [20]. A majority of such PICs are designed on the silicon platform as it allows for CMOS compatibility, coupled with the huge abundance and affordability [21, 22]. Further, it allows for high integration density due to its high refractive index which is around 3.48 at 1550 nm [23], thus allowing densely-packed photonic circuits, which are widely used for high-speed data communication applications. One major limitation of silicon is its indirect bandgap, which accounts for its inefficiency as a light emitter, restricting the integration of on-chip lasers and other active optical sources [24, 25]. Moreover, the optical loss in waveguides and couplers can lead to some performance degradation in complex circuits. Despite its challenges, silicon photonics is a highly attractive and innovative technology considering its scalability, performance potential, and integration capacity.

Now, for processing signals at high data and symbol rates in an optical communication system, sinc-shaped Nyquist pulses are excellent as they are orthogonal, have rectangular shape in the frequency domain, and comply with the Nyquist criterion of zero inter-symbol interference (ISI), thus ensuring error-free transmission of overlapping pulses coupled with minimum spectral bandwidth. Moreover, sinc pulse sequences can be employed for signal processing applications in analog-to-digital converters (ADC) and digital-to-analog converters (DAC). For ADC, it helps in anti-aliasing and in modeling the ideal sampling process, thus making the signal conversion more accurate. For DAC, such pulses help in avoiding distortion and sustaining the signal integrity, especially at higher symbol rates. These Nyquist pulses can be generated with a phase-locked and rectangular frequency comb which is produced by the sinusoidal modulation of cascaded MZMs [26]. Based on this idea, lately, many designs for Nyquist pulse generation have been implemented [27–29]. Nonetheless, in real-world scenarios, the system imperfections introduce non-idealities like optical sideband suppression, comb ripple, etc. [30–32] which affects the temporal and spectral fidelity of the pulses, eventually degrading the system performance. Now, for high-speed optical communication systems it is of utmost importance to characterize and quantify such imperfections, especially from a system metrology point of view [33], which provides the basis for evaluating and ensuring the precision and reliability of the entire communication system. In this context, waveform metrology is vital, since it helps to establish the measurement results, especially the time-domain waveforms which can be traced to the International System of Units (SI). This traceability confirms that each measurement has a certain uncertainty, thus ensuring precise system evaluation across different measurement environments.

With orthogonal sampling using flat frequency combs, it is feasible to down-convert a high-bandwidth signal into parallel low-bandwidth signals, which are then suitably processed uti-



https://doi.org/10.7795/110.20260421B

lizing low-bandwidth electronics [34–36]. With ideal equipments, this method can sample the signal error-free with no aperture jitter as the down-conversion method is entirely based on multiplying the signal with a sinc-pulse sequence in the time domain. This enhances the quality of the sampled signal, expressed in terms of parameters like the effective number of bits (ENOB) and signal-to-noise and distortion ratio (SINAD). Several works have used coherent detection to convert the sampled optical signal to electrical domain [34, 35, 37]. Nevertheless, in applications like data centers and short-reach interconnects, access networks, consumer devices, low-cost metro networks, sensor networks and distributed sensing, etc., a DD scheme is preferred [38, 39]. When compared to the coherent detection, the DD offers a cost-effective and simplified system, with reduced power consumption. Further, it does not need a local oscillator (LO), optical hybrids and phase-diverse receivers, making it feasible for applications where cost, size and energy efficiency is vital. Now, in such a DD-based optical sampling system, it is important to analyze the non-idealities to understand the system performance bottlenecks and making design improvements. The thesis focuses on two major sources of non-idealities, namely, the comb ripple and the roll-off factor of the optical filter used for DD. From a system metrology perspective [33], analyzing such impairments is crucial for evaluating the measurement integrity and operational reliability of high-speed optical channels.

The final segment of the thesis delves into the analysis of thermal crosstalk for integrated photonics systems. With the silicon photonics technology, it is possible to integrate a multitude of electronic and photonic components on the same chip, and hence undergo high bandwidth signal processing [18]. However, as the chip material will have a certain thermal conductance, it will lead to thermal crosstalk [40–42]. Consequently, the performance will be hampered for integrated devices like optical modulators, switches, photodetectors, attenuators, etc [43–46]. Hence, it is of paramount importance to alleviate the crosstalk, especially in densely packed photonic chips, where multiple devices are packed together very closely. The thesis provides a thorough study on the technique of deep trenches [47–49] to mitigate thermal crosstalk for several photonic components. Further, the study is extended to the amorphous silicon platform [50, 51] which further alleviates the thermal crosstalk, owing to its lower thermal conductivity as compared to crystalline silicon. With these techniques, for a complete communication system, it results in enhanced performance, as evidenced by a reduction in the bit error rate (BER) and improvement in the eye diagram quality.

The thesis is structured in the following manner:

**Chapter 2** This chapter gives a brief introduction to the importance of metrology in communication systems followed by a discussion of the methods used for optical frequency comb (OFC) generation with sinc-pulse sequences. Considering that the sinc-pulse sequence is not ideal, the chapter provides an introduction to the non-idealities present in an optical system which are the comb ripple, undesired sidebands, and the roll-off of the optical filter. This is followed by a discussion of signal detection techniques, specifically, direct and coherent detection. Finally, the chapter investigates thermal crosstalk and



https://doi.org/10.7795/110.20260421B

its mitigation techniques in compact integrated photonic circuits which is essential for processing the high bandwidth signals.

**Chapter 3** This segment deals with the investigation of the non-idealities in the process of generation of the sinc-shaped Nyquist pulses. Two major non-idealities are investigated, in particular, the comb ripple and optical sideband suppression for three-line, five-line and nine-line OFCs. For integrated silicon modulators, the effect of optical filter roll-off on Nyquist pulses is analyzed experimentally for a three-line OFC.

**Chapter 4** This section concentrates on the DD technique with a single photodiode for orthogonal optical sampling system with a three-line OFC. Two key error sources are investigated, concretely, the comb ripple and the optical filter roll-off and the signal deterioration is examined for sinusoidal signals and broadband signals using parameters like the root-mean-square error (RMSE), SINAD, ENOB, Q-factor etc.

**Chapter 5** This portion of the thesis addresses the issue of thermal crosstalk in compact photonic circuits for high bandwidth signal processing. Alleviation techniques for the same are discussed emphasizing the usage of integrated doped heaters and the geometrical isolation technique of deep trench for many on-chip devices like modulators, photodetectors, switches, etc. Additional methods like usage of amorphous silicon to further mitigate crosstalk are discussed. All in all, this chapter demonstrates effective crosstalk mitigation technique to achieve a complete optical communication system with densely packed PICs which support high bandwidth signal processing with enhanced performance.

**Chapter 6** The concluding chapter presents the summary and outlook of the research presented in the thesis. The investigation of the error sources for OFC generation and optical sampling in a DD system is vital for the metrological analysis of an optical system. Finally, the crosstalk mitigation techniques discussed here can be integrated into the silicon photonics platform with densely-packed devices to have a high-performance optical communication system capable of processing high bandwidth signals.



https://doi.org/10.7795/110.20260421B

# 2

# General Principles

With the rapid increase in the requirement for high bandwidth and high data rate communication, the importance of accuracy in signal generation, measurement, and detection has risen tremendously. This is especially true for optical systems which have emerged as the forefront in modern signal processing due to its inherent superior bandwidth, lower signal degradation over a long distance [14], scalability [15], immunity to EMI [16], and a multitude of other reasons. Therefore, it is of paramount importance to perform a system level metrological analysis [33] of the complete system which ensures precision, traceability and reliability of the optical communication system.

This chapter dives into the intersection of metrology and integrated photonics while focusing on the generation and detection of optical signals with sinc-pulse sequences. Firstly, the significance of metrology in optical communication systems is analyzed which is followed by the generation techniques of OFCs [26–29, 34–36], the nature of the sinc-pulse sequences, and their constraints. Then the two main signal detection schemes, namely, the coherent detection [34, 35], and the direct detection (DD) [38, 39], are discussed and the error sources are analyzed in DD systems. Finally, the issue of thermal crosstalk [40–42], and techniques for mitigating the same [47–51], are discussed for compact photonic circuits.

## 2.1 Metrology in High-Speed Optical Signal Transmission

With the rising tendency of optical communication systems to scale towards higher data rates and greater spectral efficiency, it is crucial to ensure the accuracy and reliability of signal detection and transmission. In this context, metrology [33] serves as the pillar for trustable and reproducible measurements necessary for performance evaluation and standardization of communication systems. In optical communication systems, accurate characterization of signal sources, modulators, detectors, and complete signal path is indispensable for affirming data integrity. Tracability, or the process of relating measurement results to internationally accepted standards, is extremely important in the field of photonic-assisted ADCs, where sub-picosecond timing accuracy and high signal fidelity are given tremendous importance. Accordingly, waveform metrology [52] plays a key role in enabling precise characterization and



https://doi.org/10.7795/110.20260421B

validaton of signal properties against standard references.

Accurate waveform generation and measurement are critical for the effective operation of high-end oscilloscopes and arbitrary waveform generators [53]. Beyond instrumentation, the metrological evaluation of waveforms has a wide range of applications across wireless, wired, and optical communication systems. To precisely characterize modern communication systems, it is imperative to analyze waveforms while accounting for temporally and spectrally correlated error sources. Prior work on uncertainty estimation [54–60], and sampling oscilloscope calibration [61–65] has laid the foundation for establishing waveform traceability in both photonics and high-frequency electronics industries. Within this framework, the Guide to the Expression of Uncertainty in Measurement (GUM) [66] and its supplements are vital in developing a basis to assess and express measurement uncertainties related to time domain waveform measurements.

To enable a comprehensive analysis of photonic systems, it is important to undergo full waveform metrology [67], where the entire waveform across both time and frequency domains is designated as the primary measurement target. This methodology allows for the derivation of the conventional parametric descriptions from the full-field signal, enabling accurate system characterization. Accordingly, in the realm of integrated silicon photonics and high-speed optical communication, it takes into account the time domain measurements with the high-bandwidth sampling oscilloscopes and frequency domain measurements with the vector network analyzers, while also considering the critical effects such as the time-base corrections [58] and bandwidth restrictions subject to the measurement setup. Consequently, to ensure an accurate and reliable mapping between the temporal and spectral representations of the signal, it is crucial to establish metrological traceability alongside a correlated uncertainty analysis which can be propagated across each stage of the optical measurement chain. Hence, to realize the first step towards the full waveform metrology, it is essential to quantify the imperfections that arise in the generation of sinc-shaped Nyquist pulses in the optical domain.

## 2.2 Generation of Optical Frequency Combs

At the heart of an optical communication system lies an energy-efficient integrated optical comb source, which is a compact and reliable alternative to the conventional oversized setups that rely on numerous lasers in parallel and complicated non-linear mixing levels. Consequently, the generation of OFCs has completely transformed the domain of optical metrology, communications, and ultra-fast signal processing by facilitating a broadband source of phase-coherent light with accurately defined frequency spacing. An OFC comprises of a sequence of discrete, evenly spaced spectral lines, generally spanning tens to hundreds of nanometers in bandwidth [68, 69]. These spectral lines act as an optical ruler in the frequency domain delivering an unparalleled degree of precision in applications involving timing, synchronization or spectral synthesis. Generating such OFCs can be realized by various means, each having its own set of advantages and trade-offs in terms of stability, coherence and scalability.

The standard method for OFC generation involves mode-locked lasers (MLLs) [70, 71],



https://doi.org/10.7795/110.20260421B

where femtosecond pulses are obtained with active or passive mode-locking methods in a laser cavity, resulting in a comb structure in the frequency domain stemming from the Fourier relationship between the pulse trains and the spectral components. Fiber-based and solid-state MLLs, in particular, demonstrate remarkable coherence and low phase noise, which is ideal for metrology and optical clock applications. Recently, it was demonstrated that the quantum dot MLLs operating at 60 GHz repetition rate with a broad optical bandwidth of 2.2 THz can generate both amplitude-modulated and frequency-modulated combs with large bandwidth and spectral coherence [72]. It has tremendous potential for dense wavelength division multiplexing (DWDM), on-chip communications and coherent signal detection, thus acting as a practical, scalable, and power-efficient solution for integrated OFC applications. Nevertheless, due to the bulky size, high power consumption, limited tunability, and limited integration potential due to fabrication complexity, it is not suited for chip-level implementations.

To address these shortcomings, recent developments have focused on microresonator-based Kerr frequency combs [73, 74], also called microcombs, which takes advantage of the third-order non-linear phenomenon like four-wave mixing within high quality optical microresonators. When such systems are driven by a continuous wave (CW) laser tuned to a specific resonance, they generate a cascade of new frequencies through parametric oscillation yielding in a comb-like spectral structure. Owing to the many-fold suitable properties of the microcombs like compact size, easy integration, and energy efficiency, such structures are convenient for on-chip PICs. The major platforms advancing the microcomb generation encompass silicon nitride ($Si_3N_4$), lithium niobate ($LiNbO_3$), and silica. These materials are broadly chosen due to numerous key features: $Si_3N_4$ offers exceptionally low optical propagation losses, which paves the way for high-quality resonances and effective non-linear interactions [75]. $LiNbO_3$ is distinguished by its elaborate E/O capabilities, making it very suited for active tuning and modulation within the integrated photonic devices [76]. Silica, which is a staple in the optical fiber technology, provides outstanding transparency and stability, enhancing the reliability of frequency comb generation [77]. Additionally, all the three platforms are consistent with the widely-adapted CMOS fabrication process, allowing scalable and cost-efficient manufacturing and seamless integration with the current semiconductor technologies, which is an essential factor for developing practical on-chip photonic systems. Managing parameters like pump wavelength detuning, dispersion design, and thermal stability is very essential for stabilizing the comb into preferred states such as dissipative Kerr solitons, that produce coherent, mode-locked pulse trains and low-noise frequency spacing. Nevertheless, these compact and power-efficient Kerr frequency combs can have certain shortcomings like sensitive operating conditions subject to thermal effects and limited tunability in comb spacing.

Alternatively, the E/O modulation method to generate OFC [78, 79] offers many advantages such as tunable comb spacing with modulation frequency adjustment, high coherence and excellent phase noise performance, more control over individual comb lines, and reduced sensitivity to environmental perturbations contributing to enhanced operational stability and robustness. Here, a CW laser is modulated with a series of E/O phase and amplitude modulators, usually driven by high-frequency radio frequency (RF) signals. The modulation results



https://doi.org/10.7795/110.20260421B

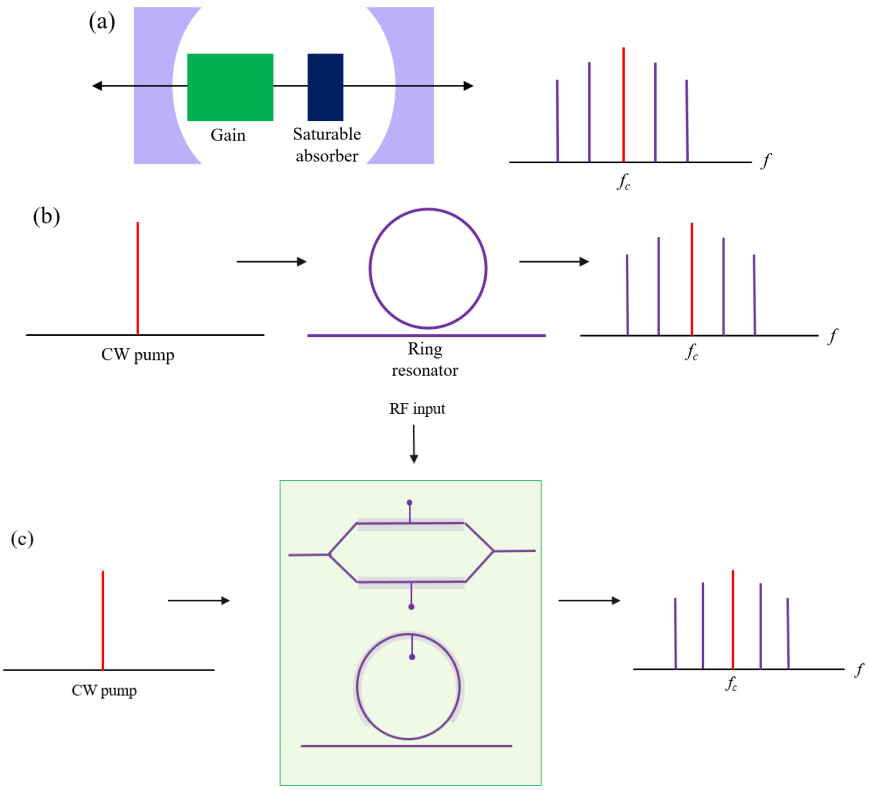


**Figure 2.1:** Various approaches to optical frequency comb (OFC) generation including (a) mode-locked laser systems [80], (b) Kerr-comb generation using an integrated ring resonator, and (c) electro-optic modulation driven by a radio-frequency (RF) source.

in a series of spectral sidebands with uniform spacing outlined by the RF signal, resulting in a comb-like pattern in the frequency domain. Adjusting the RF drive can tune this highly stable comb spacing which allows for fine spectral resolution and outstanding coherence across the comb lines, making E/O-based OFCs indispensable for applications like generation of arbitrary optical waveforms, high-resolution spectroscopy, microwave photonic technologies, and coherent optical data transmission, all of which requires precise line-by-line control, noteworthy stability, and high repeatability. Beyond E/O modulation, non-linear optical processes like optical parametric oscillation (OPO) and second-harmonic generation (SHG) in non-linear crystals [81] enable efficient wavelength conversion and spectral broadening, thus covering a broad spectrum ranging from near-infrared (NIR) to the visible and mid-infrared (MIR) regions. Collectively, E/O modulation and harmonic generation offers a multitude of advantages while compromising power efficiency, ease of integration, or bandwidth scalability. To summarize, Fig. 2.1 provides an overview of all the three major techniques employed for OFC generation.

In modern communication systems, OFCs enable a broad spectrum of advanced technologies, including high-order modulation formats, DWDM, optical arbitrary waveform generation (OAWG), and synthesis of coherent signals. OFCs can facilitate multi-channel data transmission by producing a densely spaced array of mutually coherent spectral lines, eventually resulting in improved spectral usage and minimal power consumption per bit. Hence, OFCs



https://doi.org/10.7795/110.20260421B

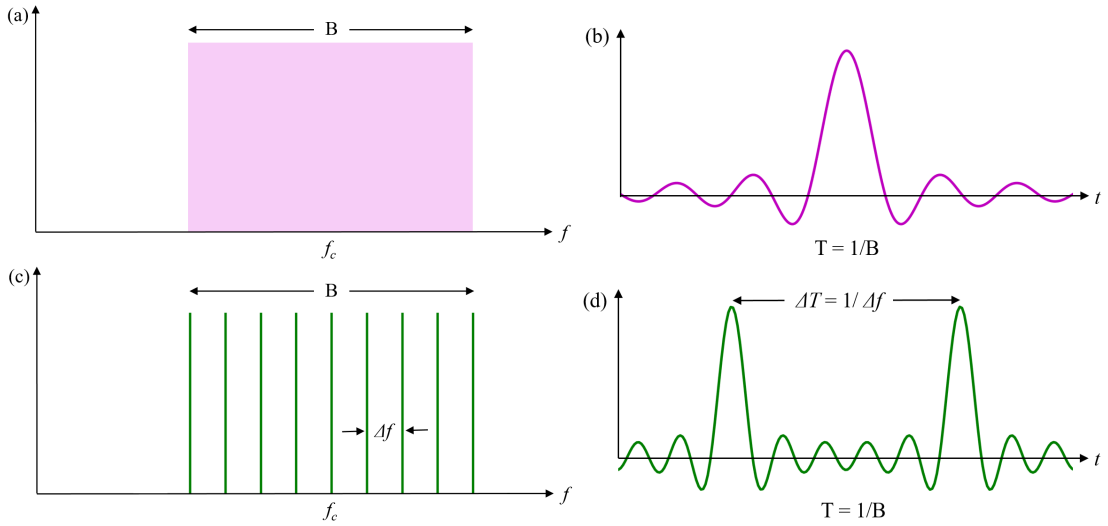


**Figure 2.2:** The frequency and time domain representations of an ideal isolated sinc-pulse with a continuous rectangular optical spectrum of bandwidth B (a, b), and (b) a sinc-shaped Nyquist pulse sequence of bandwidth $B = \Delta f \times N$ with corresponding frequency comb ($N = 9$) of spectral spacing $\Delta f$. (c, d)

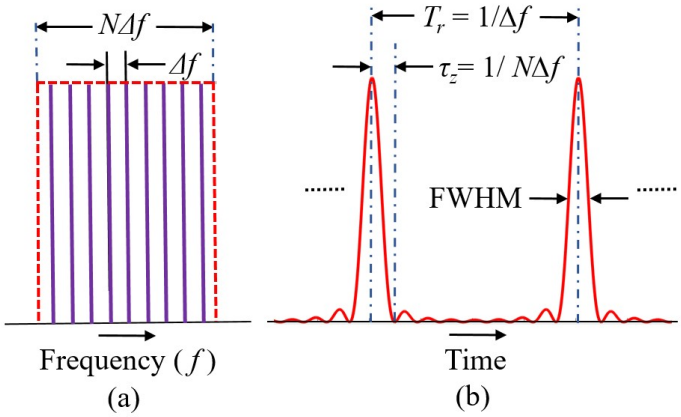


**Figure 2.3:** Schematic diagram of an $N$-line: (a) rectangular frequency comb with linearly phase-locked components, (b) the respective time-domain pulse sequence with the defined parameters taken from [82].

are a vital tool to approach the ever-increasing demands of high-throughput and power-efficient optical infrastructures.

## 2.3 Generation of Sinc-pulse Sequences

An ideal rectangular shaped frequency domain distribution translates to a sinc-shaped Nyquist pulse that spans infinitely across the time domain. As such it offers several advantages like zero ISI, orthogonality in the time domain with maximum spectral efficiency and enhanced signal integrity. However, such an ideal and isolated sinc-pulse is entirely a mathematical construct as shown in Fig. 2.2 (b) and it is not feasible to generate the same practically. Nevertheless, a phase-stabilized and spectrally flat frequency comb with uniform spectral spacing translates to a train of sinc-pulses in the time domain. Such sinc-pulse sequences can be expressed as



https://doi.org/10.7795/110.20260421B

the sum of ideal sinc pulses over an infinite time duration that are temporally offset. With increasing repetition rates, the sequences approach towards a single sinc-pulse with the same bandwidth and duration of the single pulse. A phase-locked and flat frequency comb and its corresponding sinc-pulse Nyquist sequence in the time domain is shown in Fig. 2.2 (c, d).

Such sinc-shaped Nyquist pulse sequences can be produced by a variety of techniques including filtering and shaping the spectrum of optical frequency combs produced with MLLs [70–72], Nyquist lasers [83], and by Kerr microcombs [73, 74]. Nonetheless, the generation of Nyquist pulses is a challenge owing to the limitation in the achievable roll-off steepness which is constrained by the finite sharpness of the edges of the optical filter. As a result, ideally abrupt spectral transitions are prevented, which are very important in order to generate high-quality Nyquist pulses with minimal ISI. Also, filters with an ideal rectangular spectral shape are unavailable generally. Other limitations are discussed briefly in Section 2.2.

To overcome these challenges, the sinc-shaped Nyquist pulses can be generated with E/O modulators [26, 78, 79] which can be easily integrated into a photonic system. Further, the generated Nyquist pulses are of exceptional quality with a rectangular frequency spectrum and in certain scenarios have a bandwidth three to four times higher than the modulator bandwidths.

Considering a system with two coupled intensity modulators, where the first and second modulators generate $(2n_{y1} + 1)$ and $(2n_{y2} + 1)$ spectral lines, respectively, and are phase-locked to one another, the resulting spectrally flat and phase-locked frequency comb [26, 84] has $M = (2n_{y1} + 1)(2n_{y2} + 1)$ uniformly spaced frequency components. The total bandwidth of the comb is $B = N\Delta f$, where $\Delta f$ is the frequency spacing between the adjacent comb lines. For cascaded MZMs, the OFCs are phase-locked as long as the RF signals driving the modulators are phase locked in the RF domain. The full width at half maximum (FWHM) duration of the respective sinc-shaped Nyquist pulse sequence is expressed as $\text{FWHM} = \frac{0.89}{N\Delta f}$, the pulse repetition period is given by $T_r = \frac{1}{\Delta f}$, and the pulse duration which is measured from the peak to the first zero crossing is given by $\tau_z = \frac{1}{N\Delta f}$, as illustrated in Fig. 2.3. By exerting proper control over the number of comb lines $N$ and the frequency spacing $\Delta f$, the repetition rate and pulse duration can be adjusted actively, ensuring flexible reconfiguration of the optical Nyquist pulses for specific requirements. Additionally, by fine-tuning the phase of the electrical signals driving the modulators, the sinc-pulse sequences can be temporally adjusted, giving extra control over the pulse timings.

## 2.4 Non-idealities in Sinc-pulse Sequences

In real-world scenarios, any imperfections in the process of sinc-pulse sequence generation can result in deterioration of the performance of the entire system. Hence, characterizing the performance of the system with the presence of non-idealities is critical, especially for the metrological analysis of the integrated optical sampling system as outlined as the final goal of the optical sampling analysis within the research study *Metrology for THz Communications (Meteracom)* [85]. Three major non-idealities are discussed in the thesis:



https://doi.org/10.7795/110.20260421B

### 2.4.1 Comb Ripple

In practical scenarios, comb ripple in the frequency spectrum of a sinc-pulse sequence occurs due to a multitude of practical shortcomings. In the process of sinc-pulse sequence generation with frequency comb filtering with an optical bandpass filter, ripples can arise from the finite passband ripple of the filter itself. If the pulse sequence is generated with modulators, these ripples are a consequence of suboptimal bias settings or inadequate RF drive power. For an optimal system performance, controlling the ripple is of utmost importance as even small discrepancies can ensue into drastic imperfections in the time-domain response, thus impacting system performance visible in terms of parameters like BER, ENOB, SINAD, etc. This comb ripple is given in decibels (dB) which denotes the spectral flatness of the comb and is expressed as $R_{\mathrm{dB}} = 20\log_{10}\left(\frac{A_{\mathrm{max}}}{A_{\mathrm{min}}}\right)$, where $A_{\mathrm{max}}$ and $A_{\mathrm{min}}$ are the maximum and minimum comb line amplitudes.

### 2.4.2 Sideband Suppression Ratio (SSR)

The sideband suppression ratio (SSR) is defined by the ratio of the power of the main spectral lobe ($P_{\mathrm{main}}$) to that of the undesired sidebands ($P_{\mathrm{side}}$) that usually arise from improper modulation or defective signal synthesis,and is expressed in decibels (dB) as $\mathrm{SSR\,(dB)} = 10\log_{10}\left(\frac{P_{\mathrm{main}}}{P_{\mathrm{side}}}\right)$. For sinc-pulse sequence generation with OFCs produced with MZMs, SSR is a very critical attribute as the unwanted sidebands can compromise the integrity of the intended rectangular spectral profile. For a high-performing system, the SSR is on the higher end, suggesting a strong suppression of the unwanted sidebands, ensuring the spectral purity of the comb and curtailing the leakage of noise into the adjacent channels thus resulting in an SSR ranging from 25 dB to 40 dB. On the other hand, a low SSR reveals the presence of prominent sidebands which interfere with the nearby comb lines, resulting in spectral overlap causing temporal jitter and distortion of the points of zero-crossing in the time domain, thus deteriorating the sharpness and orthogonality of the sinc pulse-sequences, consequently dropping the SSR to less than 20 dB.

### 2.4.3 Optical filter roll-off

In order to eliminate the unwanted higher order sidebands in the frequency domain produced during the process of sinc-shaped Nyquist pulse sequence generation with MLL [70–72] or Kerr microcombs [73, 74], it is critical to use a rectangular optical filter with a very steep out-of-band suppression. Theoretically, a perfect rectangular spectrum in the frequency domain will have infinitely steep transitions at the edges and translate to ideal sinc pulses in the time domain. Nevertheless, in real-world scenarios, such ideal filters do not exist and practical filters obtained with silicon-based Bragg gratings [86], arrayed waveguide grating structures [87], or ring resonators on silicon photonics [88] platform have a finite roll-off $\beta$. This roll-off factor indicates the surplus bandwidth of the pulse relative to an ideal sinc pulse with $\beta = 0$ and suggesting the presence of many higher-order sidebands in the frequency domain. These unwanted sidebands arise as the transition from the passband to the stopband occurs



https://doi.org/10.7795/110.20260421B

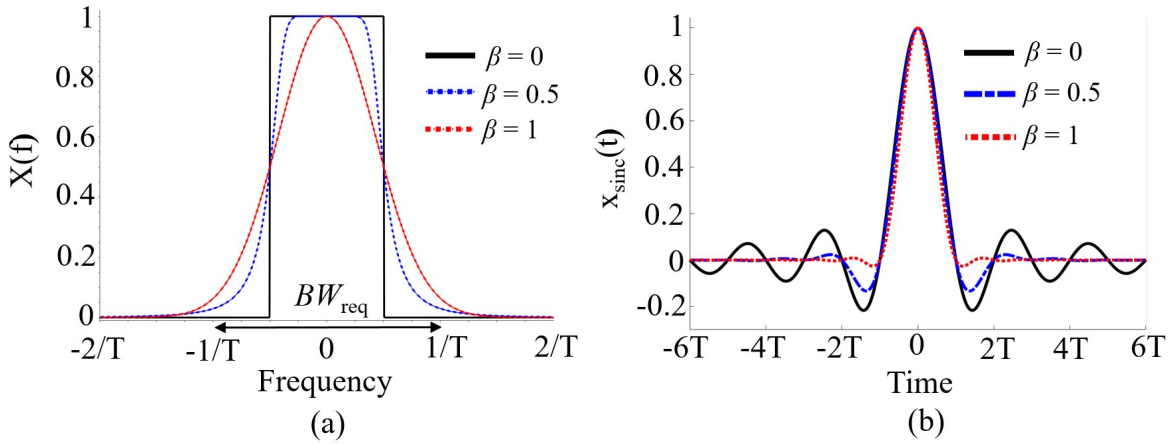


**Figure 2.4:** Schematic diagrams of sinc-shaped Nyquist pulses with roll-off factors $\beta = 0$, 0.5, and 1 are depicted in (a) the frequency domain and (b) the time domain taken from [82], where the required bandwidth ($BW_{\text{req}}$) is defined by equation (2.2).

progressively rather than suddenly which leads to a tapered spectral edge. The time domain expression for a single sinc-shaped Nyquist pulse with a roll-off $\beta$ and established system parameters is given by:

$$x_{\text{sinc}}(t) = \text{sinc}\left(\frac{t}{\tau_z}\right) \cdot \frac{\cos\left(\beta\pi\frac{t}{\tau_z}\right)}{1 - \left(\frac{2\beta t}{\tau_z}\right)^2} \tag{2.1}$$

The influence of the roll-off $\beta$ in the bandwidth of the pulse and the time-domain shape is depicted in Fig. 2.4. For ideal scenario, $\beta = 0$ and the sinc-shaped Nyquist pulse is expressed as: $x_{\text{sinc}}(t) = \text{sinc}\left(\frac{t}{\tau_z}\right)$ and the bandwidth required ($BW_{\text{req}}$) is just $\frac{1}{\tau_z}$. However, for practical scenarios with a finite roll-off $\beta$, the bandwidth required ($BW_{\text{req}}$) is expressed as [89]:

$$BW_{\text{req}} = \frac{1+\beta}{\tau_z} \tag{2.2}$$

Hence, it is clear that optical filtering in functional applications will always have some spectral leakage which compromises the ideal rectangular spectral shape and deteriorates the temporal response of the pulse visualized as higher sidelobes with wider temporal spread.

## 2.5 Signal detection methods in optical systems

A complete optical communication system fundamentally consists of transmitter and receiver modules as depicted in Fig. 2.5. Previous sections have discussed the generation of sinc-shaped Nyquist pulses at the transmitter side using E/O modulators that translates the data signals from electrical to optical domain. The optical carrier generated with the laser is modulated with the data signal originating from a DAC with E/O conversion, which performs up-conversion on the electrical signal into optical carrier frequencies. To enable data transmission at high speeds, the electrical signals are operated with DSP techniques and the modulated optical output is eventually guided through an optical waveguide that acts as the transmission



https://doi.org/10.7795/110.20260421B

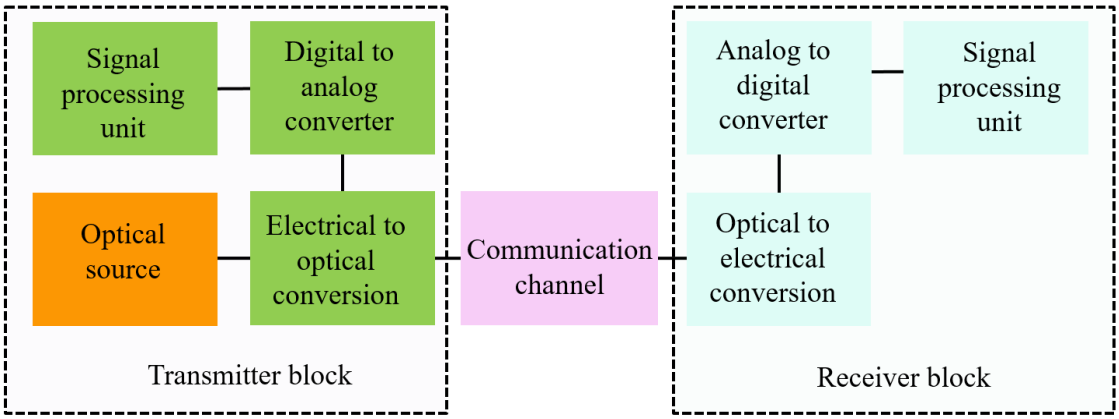


**Figure 2.5:** Block diagram of a silicon photonic-based system for optical communication application. At the optical transmitter side, the integrated laser source provides an optical carrier. The electrical signal (data pattern) is up-converted to optical carrier frequencies using electrical-to-optical conversion. The transmission medium, usually a silica-based optical fiber, is used as a transmission link between the optical transmitter and receiver. The optical receiver down-converts the optical signal to the electrical domain, and the received signal is analyzed by digital signal processing. The digital-to-analog converter on the transmitter side and the analog-to-digital converter on the receiver side act as the link between electrical and optical interfaces.

channel. The primary function of the DAC is to translate the digital signals into respective analog voltages or currents. To ensure signal integrity and avoid aliasing, the Nyquist theorem mandates that the sampling frequency $f_s$ should be at least twice the highest signal frequency. Hence, the output frequency of a conventional DAC extends from direct current (DC) to just below half the sampling frequency or $f_s/2$. Concurrently, the modulated optical signal propagates through an optical waveguide which serves as the transmission medium. The type of the optical network is determined by the length of the link and is classified as access (1 to 10 km), metro (10 to 100 km), and core network (around 100 km). For core networks, high-speed and long-distance transmission technologies are important to support data rates ranging up to 1 Tbit/s and meet with the constantly growing data demands. The receiver module uses digital detection technologies for translating the signal back into the electrical domain with O/E conversion, ADC and DSP techniques, where the ADC processes the analog signal into digital form. Depending on the distance of the transmission link and the format chosen for modulation, an appropriate detection technology is chosen. The coherent detection (CD) [34, 35, 37] is usually preferred for long-haul links prioritizing the recovery of amplitude and phase information with a LO as the phase reference. For shorter links like in data centers, direct detection DD [38, 39] is generally adopted to get back the intensity-modulated signals. The performance of the optical links is largely determined by the bandwidth and efficiency of the photonic devices enabling O/E and E/O conversions.

Along with the photonic elements, the capacity of the optical transmission link is influenced by the performance of the DAC to generate the data signal, the ADC to digitize the signal, and the DSP techniques used. Therefore, to enhance the link performance, the components must operate with high sampling frequencies and wide analog bandwidths. Nevertheless, traditional electronic ADCs and DACs suffer from declined resolution at elevated sampling rates which is measured in terms of ENOB as a consequence of multiple issues like electronic jitter, thermal



https://doi.org/10.7795/110.20260421B

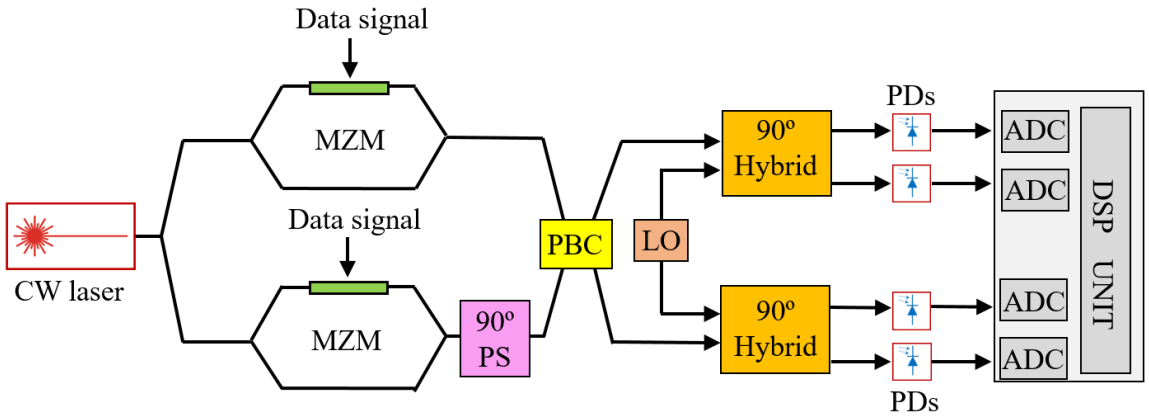


**Figure 2.6:** The schematic diagram for coherent detection (CD). MZM: Mach-Zehnder modulator, CW laser: continuous wave laser, PBC: polarisation beam combiner, PS: phase shifter, LO: local oscillator, PD: photodetector, ADC: analog-to-digital converter, DSP: digital signal processing.

fluctuations, circuit non-linearities, etc. To overcome these challenges, photonic-assisted ADCs and DACs are well-suited considering the faster operation, simplified architecture, reduced power consumption and wider bandwidth of operation. But the highest achievable sampling rate is still limited by the bandwidth of the E/O equipments utilized. A promising solution can be integrating sinc-shaped Nyquist pulse sequences [26, 84] into such systems to allow for a fully integrated and reconfigurable architecture capable of high-speed operation. Based on the sampling theorem, a band-limited signal can be reconstructed with a linear combination of temporally shifted sinc-pulses. Practically, sinc-shaped Nyquist pulse sequences, obtained with silicon modulators, can be used for precise signal generation and detection in the optical domain. This enables high-bandwidth conversion through optical sampling and time-domain interleaving, while using low-bandwidth components. The two main detection techniques in an optical communication system, namely, coherent detection CD and direct detection DD are discussed below.

### 2.5.1 Coherent detection (CD)

The coherent detection (CD) allows for the complete recovery of the amplitude, phase, and polarization information of the optical signal. Here, the incoming optical signal is combined with a CW local oscillator (LO) laser inside a 90° optical hybrid to generate in-phase (I) and quadrature (Q) components, and these are eventually detected with the balanced photodetectors as depicted by the block diagram in Fig. 2.6. Complicated and higher-order modulation schemes like binary phase shift keying (BPSK), quadrature phase shift keying (QPSK), and higher-order quadrature amplitude modulation (QAM) can be received with this setup thus enhancing the spectral efficiency and capacity of the optical link. Moreover, as briefly mentioned in the previous section, CD is indispensable for long-haul and ultra-long-haul communications owing to its sophisticated DSP techniques to alleviate impairments like chromatic dispersion, polarization mode dispersion, and frequency offsets. As such, for high-performance and demanding applications requiring high sensitivity like submarine cables, core networks,



https://doi.org/10.7795/110.20260421B

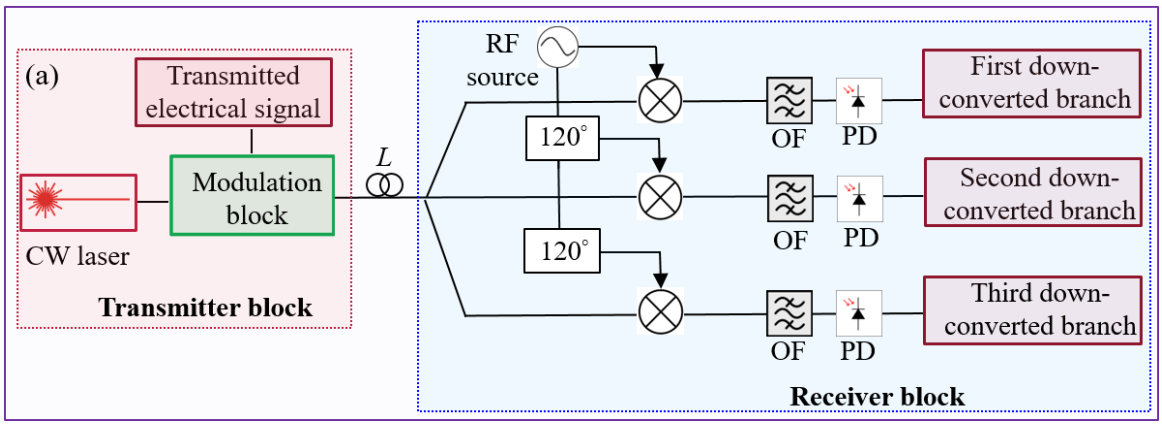


**Figure 2.7:** The schematic diagram for direct detection (DD) consisting of a single photodiode based on [90].

and data center interconnects, CD offers higher sensitivity, reach and capacity. With the recent advancements in integrated silicon photonics technology, the coherent components can be miniaturized and integrated into the system along with advanced DSP chips, enhancing their usage in metro and access networks. Consequently, several of the recent works have used the CD scheme for translating the sampled electrical signal to the optical domain [34, 35, 37]. However, for several applications like server-to-server communication links, access networks, economical urban optical links, etc., a cost-effective, simplified, and power efficient detection system is preferred rather than coherent receivers which are costly with complicated designs.

### 2.5.2 Direct detection (DD)

Direct detection (DD) is immensely useful in short-reach and cost-effective applications like data centers, access networks, and handheld consumer devices. Unlike the CD, the DD offers a economical and simplified system with a lower power consumption without using a LO [38, 39]. Additionally, these systems are easily integrable in compact transceivers and also in the silicon photonics platform [18]. In this approach, the detected photocurrent is proportional to the optical power collected at the photodiode, allowing only the amplitude information of the signal to be retrieved as per the schematic diagram for DD shown in Fig. 2.7 [90]. Consequently, the phase and frequency information is not preserved, and hence only relatively simple intensity-based modulation formats like on-off keying (OOK), pulse amplitude modulation (PAM), or some multilevel amplitude schemes can be used. In such DD-based optical sampling systems, evaluating the imperfections is critical to identify the performance limitations and guiding design enhancements. The thesis primarily investigates the effect of two primary impairments, namely, comb ripple and the roll-off $\beta$ of the optical filter used in DD. As emphasized in the system metrology literature [33], understanding such non-idealities is pivotal for assessing the measurement accuracy and ensuring reliable operation in high-speed optical communication links.



https://doi.org/10.7795/110.20260421B

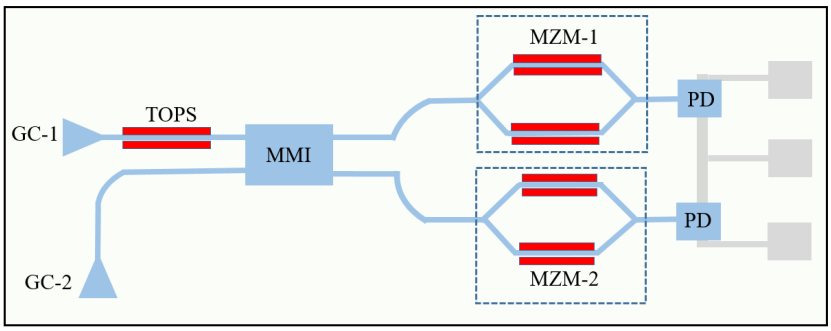


**Figure 2.8:** The schematic diagram for a simple PIC consisting of Mach-Zehnder modulator (MZM)s and photodetectors based on [91]. GC: grating coupler, MZM: Mach-Zehnder modulator, MMI: multimode interferometer, PD: photodetector, TOPS: thermo-optic phase shifters. Here, light is coupled into the chip using the two grating couplers and the anode and cathode of the top and bottom photodetectors are common so as to ease the flow of differential current into the transimpedance amplifier (TIA).

## 2.6 Thermal Crosstalk in Integrated Photonic Circuits

The integrated silicon photonics technology enables the integration of a variety of electronic and photonic components on the same chip, thus realizing a multitude of optical functions like modulation, wavelength filtering, multiplexing, etc. to build a complete photonic system. While optical fibers for long-distance communication are usually composed of silica, integrated photonic circuits are conventionally fabricated with silicon. Silicon (Si), being transparent at infrared wavelengths, is widely used in telecommunications, with silicon-on-insulator (SOI) emerging as the most popular platform considering the compatibility with CMOS technology [18, 92]. Thus, a variety of photonic functionalities can be densely integrated on a single chip with CMOS circuitry enabling precise control over the photonic elements in the chip. In such silicon PICs, thermo-optic phase shifters (TOPS) [93–97] are vital components which enable dynamic optical phase control with localized heating. A simple PIC with TOPS, MZM, $2 \times 2$ Multi-mode interferometer (MMI), and photodetectors is shown in Fig. 2.8 [91]. Such TOPS operate by using a micro-heater to heat the waveguide, altering the refractive index of silicon and thus inducing a phase shift in the guided optical signal. While TOPS are CMOS compatible with low insertion loss and easy fabrication, their performance is sometimes limited by high power consumption and slow modulation speeds when compared to E/O alternatives [98, 99]. Nevertheless, the simple and scalable design of TOPS render them valuable in silicon PICs for a multitude of applications like optical switching, filtering, sensing, advanced communications, quantum photonics, wavelength division multiplexing (WDM) systems, programmable photonic processors, and neuromorphic computing, often implemented with structures like microring resonators, photonic mesh networks, Mach-Zehnder interferometer (MZI)s, and modulator arrays.

Now, in such PICs the components are very densely integrated where multiple devices are packed very closely to each other. The chip materials like silicon have very high thermal conductivity around 148 W/m·K and they tend to propagate heat laterally across the chip elevating the risk of undesired temperature rise in the adjoining components. This heat diffusion and the unavailability of active cooling mechanism at the chip level results in thermal



https://doi.org/10.7795/110.20260421B

crosstalk which is a huge problem in circuits where the spacing between the waveguides and devices ranges in the nanometers to micrometers scale. On the other hand, materials with low thermal conductivity like silicon dioxide ($SiO_2$) (1.4 W/m·K) alleviates the lateral thermal coupling by localizing the heat. However, due to the inability to transfer the heat effectively across the low-conductivity materials, the heat remains trapped for an extended period resulting in heat retention and slower thermal response.

### 2.6.1 Effects of Thermal Crosstalk on System Performance

For high-bandwidth and high accuracy operations in PICs, the prevalence of thermal crosstalk acts as a major setback which can extensively deteriorate the system performance. In photonic chips, this affects the passive waveguides and interferometers ensuing undesired phase shifts eventually resulting in phase errors and instability in components like MZIs [100], where it is critical to have precise control of phase to undergo interference-based switching and modulation. Photonic resonators like microring-based modulators [101] and filters are extremely sensitive to thermal crosstalk which changes the resonance wavelengths. Consequently, this mismatch degrades the precision of optical filtering, elevating the insertion losses and interchannel crosstalk in WDM networks. In sensitive photonic applications that require high-precision optical processing, such as Nyquist pulse shapers or ADCs, thermal crosstalk can result in grave signal deterioration causing phase and resonance instabilities that degrade the fidelity of signal reconstruction with higher ISI and BER. In optical switching arrays [102], undesired thermal activation results in lowered contrast levels, elevating the probability of routing errors. For systems applied in precision metrology and quantum photonics [103], adherence to rigid thermal and phase stability is essential, and even minor thermal crosstalk can compromise system functionality or faulty measurements. Consequently, addressing the thermal crosstalk is vital in optical platforms, especially in PICs focusing on high-bandwidth and precision operations, where the crosstalk can directly influence several performance metrics like stability, precision and scalability.

### 2.6.2 Thermal Crosstalk mitigation

Due to the perilous impact of thermal crosstalk on compact PICs as discussed in the previous section, it is of utmost importance to address the issue using schemes targeting both improvements in heater efficiency as well as innovations in thermal isolation using the design layout and material properties. Consequently, many approaches have been investigated to alleviate the crosstalk. The integrated doped heaters [96, 104, 105] have a compact size, are CMOS compatible, and can be integrated easily along optical waveguides owing to their precise fabrication. Nevertheless, the high thermal conductivity of crystalline silicon results in the lateral diffusion of heat facilitating undesired thermal effects. To enhance the thermal isolation, oxide trenches [96, 106, 107] act as insulating barriers, while deep trench isolation techniques [104, 105, 108, 109] help in insulating against both vertical and lateral flow of heat with the drawback of reduced mechanical stability. Additionally, choosing amorphous silicon with lower thermal conductivity [110] than crystalline silicon results in efficient thermal tun-



https://doi.org/10.7795/110.20260421B

ing at less power levels with reduced lateral heat diffusion. All in all, addressing the issue of thermal crosstalk requires an orchestrated involvement of many different methods. Integrated doped silicon heaters ensure precise thermal tuning, air-filled oxide and deep trench structures prevent thermal diffusion, and amorphous silicon (a-Si) improves the thermal efficiency and isolation even further. Realizing all of these approaches can lead to scalable, thermally stable, and high-performing optical systems.

## 2.7 Conclusion

To summarize, this chapter has delved into the generation of optical frequency combs (OFCs) with sinc-pulse sequences. As such, the role of system imperfections like comb ripple, unwanted sidebands, and filter roll-off are discussed in order to characterize the system for stable performance. Signal detection methods, namely, coherent and direct detection are examined to understand their effect on signal accuracy. Moreover, the general principles underlying the investigations presented in this thesis have been outlined to give a foundation for the analyses given in the following chapters. Eventually, the issue of thermal crosstalk and the respective mitigation strategies is discussed while emphasizing the criticality of managing heat in compact and densely packed PICs. Collectively, the insights elaborated here serve as the basis for addressing the critical challenges and design strategies necessary for developing reliable and high-performance optical communication systems for high-bandwidth signal processing.



https://doi.org/10.7795/110.20260421B

# 3

# Non-idealities in Sinc-shaped Nyquist Pulse Generation

The rising global demand for data-intensive applications like high-speed communications, sensing, and real-time signal processing can be satisfied by optical signal processing owing to its broader bandwidth, easier implementation, immunity to EMI, low power consumption, and above all, seamless integration with silicon photonics-based PICs. In this context, the optical sinc-shaped Nyquist pulses [26, 83, 111–117] comply with the Nyquist criterion by eradicating the ISI, thus ensuring transmission of temporally overlapping data pulses without any error. Further, these pulses conserve the spectral bandwidth and exhibit higher tolerance to channel non-linearities and fiber dispersion [111]. Such pulses are promising candidates for all-optical signal processing and high data rate transmission systems.

Such Nyquist pulses can be produced by several techniques discussed in the previous chapter in section 2.3. This chapter focusses directly on the examination of the assosiated non-idealities in the process of Nyquist pulse generation.

## Supporting Publications

### Journal Articles

- **S. De**, A. Misra, R. Das, T. Kleine-Ostmann and T. Schneider, "Analysis of Non-Idealities in the Generation of Reconfigurable Sinc-Shaped Optical Nyquist Pulses," in *IEEE Access*, vol. 9, pp. 76286-76295, 2021, [82].

- **S. De**, K. Singh C. Kress, R. Das, T. Schwabe, S. Preußler, T. Kleine-Ostmann, J. C. Scheytt, and, T. Schneider "Roll-Off Factor Analysis of Optical Nyquist Pulses Generated by an On-Chip Mach-Zehnder Modulator," in *IEEE Photonics Technology Letters*, vol. 33, no. 21, pp. 1189-1192, 2021, [118].

### Book Chapters

- **S. De**, Y. Mandalawi, R. Das, and T. Schneider, “Metrological Analysis of Non-idealities for Photonics Assisted Signal Processing,” in T. Kürner, T. Doeker, T. Kleine-Ostmann,



https://doi.org/10.7795/110.20260421B

T. Schneider, D. Humphreys (editors), *Metrology for THz Communications - Findings from DFG FOR 2863 Meteracom, Springer Nature*, November 28th, 2025 [119].

- **S. De**, Y. Mandalawi, R. Das, and M. Weizel, "Integrated Photonics Assisted Signal Processing and Thermal Crosstalk," in T. Kürner, T. Doeker, T. Kleine-Ostmann, T. Schneider, D. Humphreys (editors), *Metrology for THz Communications - Findings from DFG FOR 2863 Meteracom, Springer Nature*, November 28th, 2025 [120].

#### Conference Proceedings

- **S. De**, R. Das, T. Kleine-Ostmann and T. Schneider, "Characterization of non-idealities in optical Nyquist pulses for THz signal sampling metrology," *46th International Conference on Infrared, Millimeter and Terahertz Waves (IRMMW-THz)*, Chengdu, China, 2021, pp. 1-2, [121].

## 3.1 Examination of non-idealities

In real-world scenarios, the presence of non-idealities in sinc-pulse sequence generation can deteriorate the system performance. Therefore, it is necessary to characterize the performance of the system considering the presence of non-idealities, particularly for the metrological evaluation of integrated optical sampling systems [85]. Three major non-idealities are discussed in the thesis, namely, comb ripple, SSR, and optical filter roll-off which have been described briefly in the previous chapter in Section 2.4. All simulations of non-idealities for sinc pulse sequence generation were done with INTERCONNECT Solver of Lumerical [122], where the required component models were taken from the library. These models were modified as per the experimental parameters to ensure that the experimental and simulation results are congruent. For investigating the comb ripple and SSR, three-line frequency combs with 5 GHz frequency spacing were considered and the simulation outcomes were benchmarked against the experiments [82]. For simulations with higher order frequency combs, like five-line and nine-line combs, the frequency spacing ($\Delta f$) is considered to be 50 GHz [82]. For optical filter roll-off analysis, experiments have been performed considering an integrated on-chip silicon MZM with a repetition frequency of 8.4 GHz [118]. For all the scenarios, the RMSE is evaluated as per [118]:

$$RMSE = \sqrt{\frac{1}{N}\sum_{k=1}^{N}(M_k - I_k)^2} \tag{3.1}$$

where $RMSE$ represents the total root-mean-square error, $M_k$ and $I_k$ are the $k^{\text{th}}$ samples of the measured and ideal signals, and $N$ denotes the total number of sampling points. For the study of comb ripple and SSR, the data is computed over a single pulse repetition period, spanning from one peak to the next with a total of 10000 sampling points ($N$) [82] and for roll-off analysis the data is evaluated over 80000 sampling points ($N$) spanning four pulse periods



https://doi.org/10.7795/110.20260421B

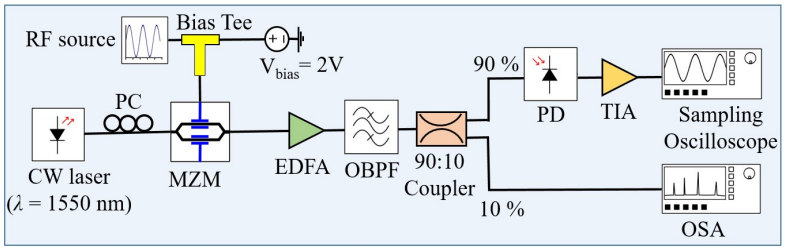


**Figure 3.1:** Schematic diagram of the experimental configuration to generate the three-line comb [82]. EDFA: Erbium-doped fiber amplifier, RF source: Radio Frequency source, OBPF: Optical Bandpass filter, PD: Photodetector, TIA: Transimpedance Amplifier, OSA: Optical Spectrum Analyzer, Sampling Oscilloscope.

[118]. The subsequent sub-sections provide an in-depth analysis of the three key non-idealities: comb ripple, SSR, and optical filter roll-off.

### 3.1.1 Impact of comb ripple

The reason behind the presence of comb ripple in frequency spectrum in the process of Nyquist pulse generation with frequency comb filtering is discussed in the previous chapter in Section 2.4.1. Additionally, the $LiNbO_3$ modulator has a certain amount of residual chirp along with a restricted extinction ratio, and other electronic non-linearities which leads to amplitude variations across the comb. These imperfections also contribute to ripple in the frequency domain and corresponding deviations of the sinc-shaped Nyquist pulses in the time domain. As shown in the experimental setup in Fig. 3.1, the continuous-wave (CW) laser is modulated at 1550 nm using a 5 GHz RF signal produced with a RF generator (ANRITSU MG3692A) and a $LiNbO_3$ based electro-optic MZM which results in a three-line OFC. The polarization controller (PC) aligns the input light polarization to the MZM, and the MZM is biased with a DC source for optimal performance. The modulated output signal is amplified with an Er-doped fiber amplifier (EDFA) and filtered with an optical band-pass filter (OBPF) centered at 1550 nm with a bandwidth of 50 GHz to suppress the amplified spontaneous emission noise. A 90:10 fiber coupler is then used to divert 10 % of the signal power into the optical spectrum analyzer (OSA) (YOKOGAWA AQ3670C) for spectral analysis and the remaining 90 % of the power goes into a Finisar photodetector (PD) which is connected to an electrical sampling oscilloscope (Agilent 86100C) to observe the signal in the time domain. In this setup, the combs are examined in both the frequency and time domains for different positive ripple values by modifying the bias voltage applied across the MZM. Increasing the ripple ($R_p$) values causes the sinc-shaped Nyquist pulses to stray further from the ideal shape, which reduces the zero-crossing duration $\tau_z$ and the FWHM in the time domain, while the repetition rate of the pulse remains identical. At a ripple ($R_p$) of 0.5 dB for a three-line OFC (peak-to-peak passband variation, with the main carrier higher than the sidebands), as shown in Fig. 3.2 (a, b), the main lobe of the measured pulse aligns well with the ideal sinc-shaped Nyquist pulse, with minor sidelobe discrepancies in the time domain. As the ripple increases, destructive interference is altered, reducing the zero-crossing duration $\tau_z$ and broadening the FWHM. While the main lobe remains close to the ideal shape, the sidelobe amplitude decreases significantly, degrading the pulse quality.



https://doi.org/10.7795/110.20260421B

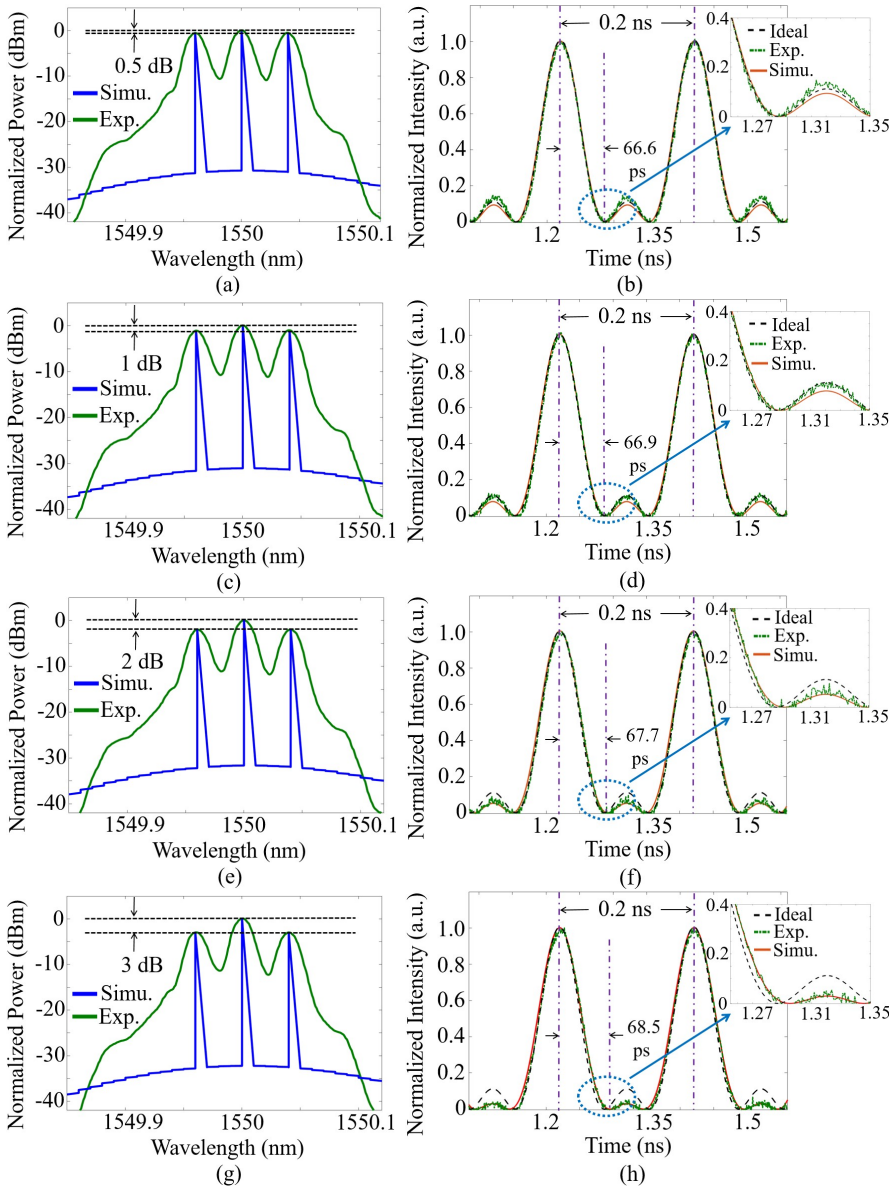


**Figure 3.2:** Three-line optical comb and the respective sinc-shaped Nyquist pulse sequences for different levels of ripple: 0.5 dB (a, b), 1 dB (c, d), and 2 dB (e, f) taken from [82]. The ideal sinc-shaped Nyquist pulse train without ripple and with a high sidelobe suppression ratio (SSR) of approximately 35 dB is shown in black. The simulated pulses and experimental pulses corresponding to each ripple level ($R_p$) are depicted in orange and green, respectively.

Now when the comb lines are increased, it results in a system more robust against ripple. For five-line and nine-line combs with a frequency spacing of 50 GHz, the ripple analysis was carried out in the frequency and time domains starting at $R_p = 0.5$ dB for visualization as depicted in Figures 3.3 and 3.4, respectively. It is worth noting that for nine-line OFCs, the frequency domain profile has a flatter envelope and in the time domain, the pulses follow very closely to the ideal sinc profile. Eventually, the RMSE was calculated for three-line, five-line and nine-line combs starting at a ripple ($R_p$) of 0.05 dB as shown in Fig. 3.5. With higher comb lines, the bandwidth of the optical frequency comb increases. Further, every extra line boosts the interference that shapes the time domain Nyquist pulse. Eventually, the influence



https://doi.org/10.7795/110.20260421B

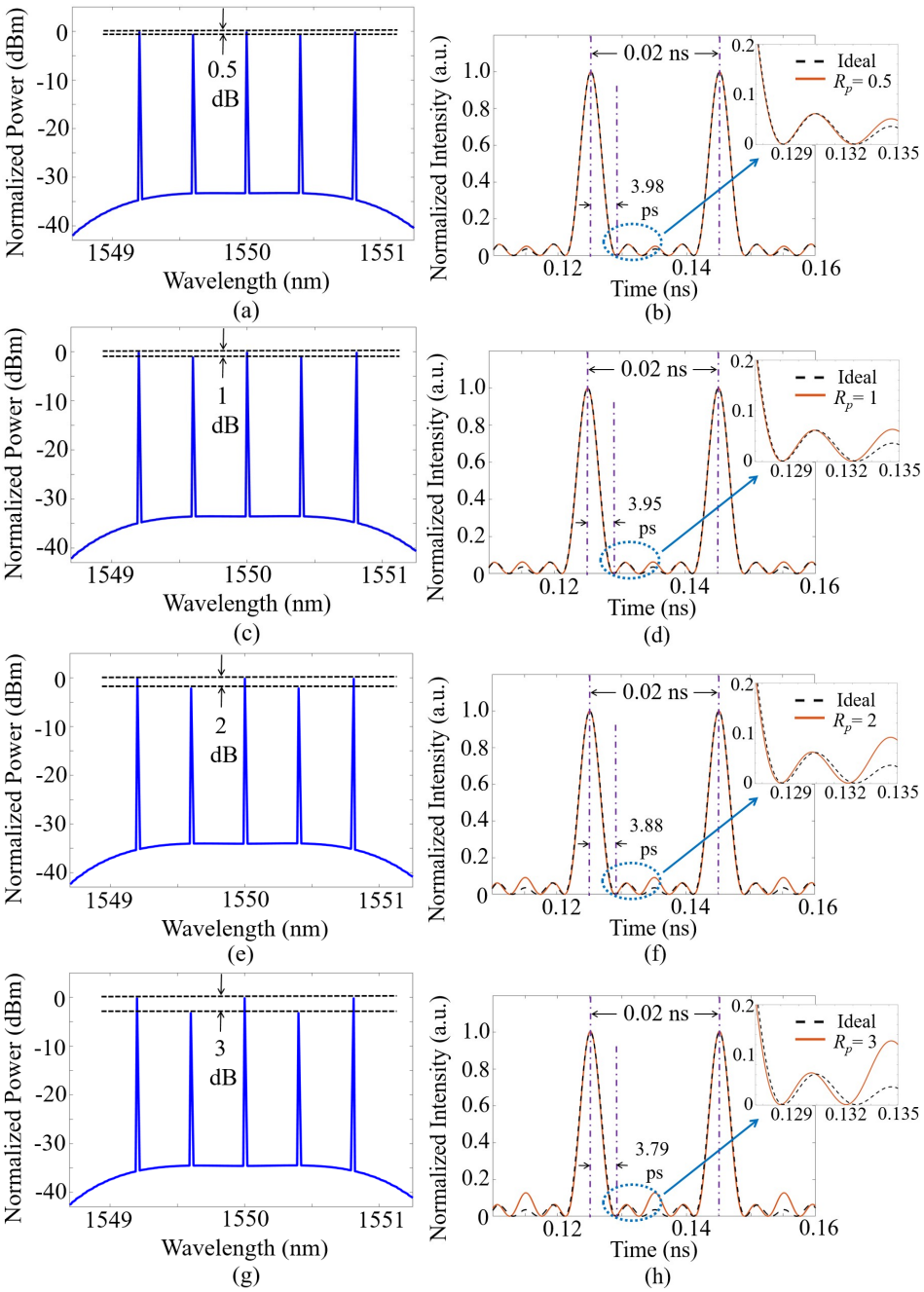


**Figure 3.3:** Five-line optical comb and the respective sinc-shaped Nyquist pulse sequences for different levels of ripple: 0.5 dB (a, b), 1 dB (c, d), 2 dB (e, f), and 3 dB (g, h) taken from [82]. The ideal sinc-shaped Nyquist pulse train without ripple and with a high sidelobe suppression ratio (SSR) of approximately 35 dB is shown in black. The simulated pulses corresponding to each ripple level ($R_p$) are depicted in orange.

of imperfections in individual lines reduces with more comb lines, thus improving the overall shape of the spectrum. Consequently, the pulse has sharper zero crossings with reduced distortion of the sidelobes, while the main lobe is closer to the ideal sinc, resulting in high fidelity and lower RMSE. Therefore, it is observed that the nine-line comb has a better performance than the five-line comb followed by the three-line comb. Further curtailment of comb ripple is possible by MZM bias control with feedback circuits, improving RF linearity,



https://doi.org/10.7795/110.20260421B

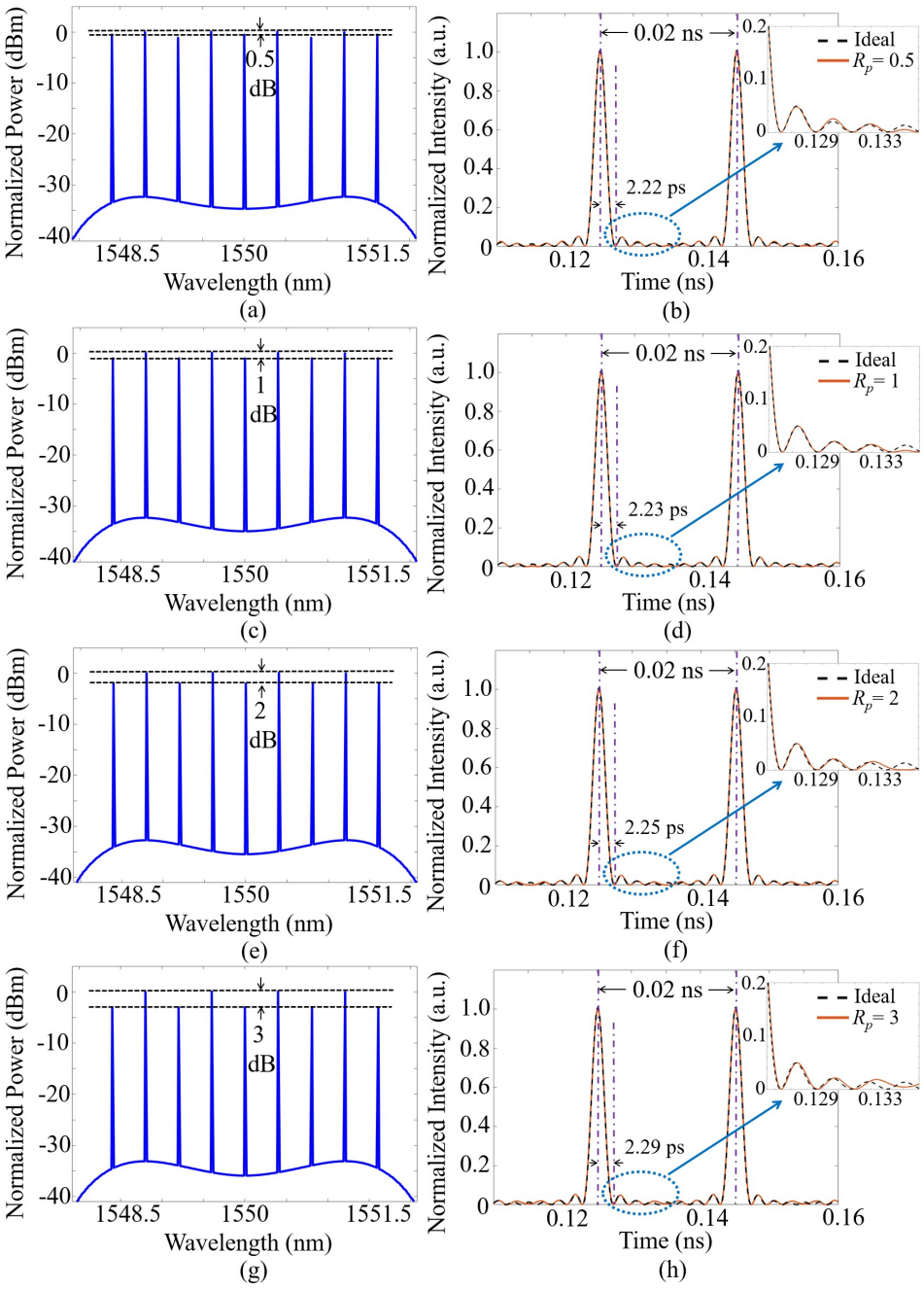


**Figure 3.4:** Nine-line optical comb and the respective sinc-shaped Nyquist pulse sequences for different levels of ripple: 0.5 dB (a, b), 1 dB (c, d), 2 dB (e, f), and 3 dB (g, h) taken from [82]. The ideal sinc-shaped Nyquist pulse train without ripple and with a high sidelobe suppression ratio (SSR) of approximately 35 dB is shown in black. The simulated pulses corresponding to each ripple level ($R_p$) are depicted in orange.

and flattening the spectrum with filters or pre-distortion to ensure flatter comb and higher-quality Nyquist pulses.

### 3.1.2 Impact of Sideband Suppression ratio (SSR)

In the process of generation of sinc-pulse sequences with OFCs, undesired sidebands can compromise the signal integrity and reduce the spectral purity. For Nyquist pulse generation with



https://doi.org/10.7795/110.20260421B

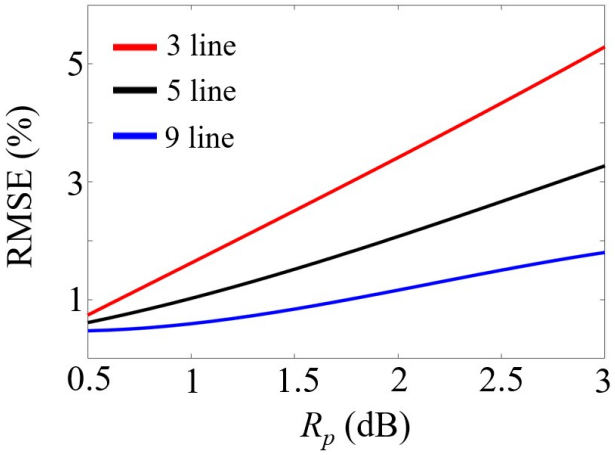


**Figure 3.5:** Comparative analysis of the root-mean-square errors (RMSE) (in %) for three-, five-, and nine-line combs across various ripple levels ($R_p$) taken from [82].

broadband sources like MLLs, additional optical filtering can reduce the undesired sidebands and augment the SSR. Conversely, when cascaded MZMs are used for Nyquist pulse generation, the higher order sidebands are suppressed with precise bias adjustment and optimized RF driving conditions. In any case, for better system performance, it is important to suppress the unwanted sidebands which ensures the spectral purity of the comb and reduces the leakage of noise into the adjacent channels. Consequently, higher SSR, as defined in Section 2.4.2, leads to an improved system performance. For the experimental analysis, the same setup is used as given in Fig. 3.1 where a three-line comb is generated with a CW laser at 1550 nm with a 5 GHz RF signal modulated with a $LiNbO_3$ based electro-optic MZM. Additionally, for SSR examination, extra sidebands are generated at 10 GHz with a secondary sinusoidal source which is kept in sync with the main RF source, and fed together to the MZM with a bias-T circuit after combination with an RF power combiner. Varying the power across the secondary sinusoidal source modifies the SSR across the three-line OFC which is analyzed in frequency and time domain as depicted in Fig. 3.6. Under near-ideal conditios where the Nyquist pulse train has a high sideband suppression ratio (SSR) of approximately 40 dB, the sinc-shaped Nyquist pulses exhibit a 0.2 ns periodicity, a FWHM of 59.33 ps, and a pulse duration $\tau_z$ of 66.67 ps. Experimental results with 5 GHz frequency spacing depicted in Fig. 3.6 confirm that increasing the SSR enhances the quality of the pulses by increasing the FWHM and pulse duration $\tau_z$ close to the ideal values. Higher SSR diminishes the effect of the unwanted higher-order sidebands, thus reducing the waveform distortion.

Small deviations between the experimental and simulation results can be attributed to the non-ideal electro-optic response of the $LiNbO_3$ based MZM. It is observed in Fig. 3.6 that for a lower SSR of 6 dB there is a poor agreement between the generated sinc-shaped Nyquist pulse sequences and the ideal signal. However, with 12 dB SSR, the sidelobes are significantly suppressed and the generated pulse sequences closely resemble the ideal signal. Even with a higher frequency spacing in the three-line comb of 200 GHz [121] as seen in Fig. 3.7, increasing the SSR leads to more resemblance in the generated pulse sequences to the ideal pulses. Here, the additional lines depict the higher-order sidebands which are intentionally introduced to



https://doi.org/10.7795/110.20260421B

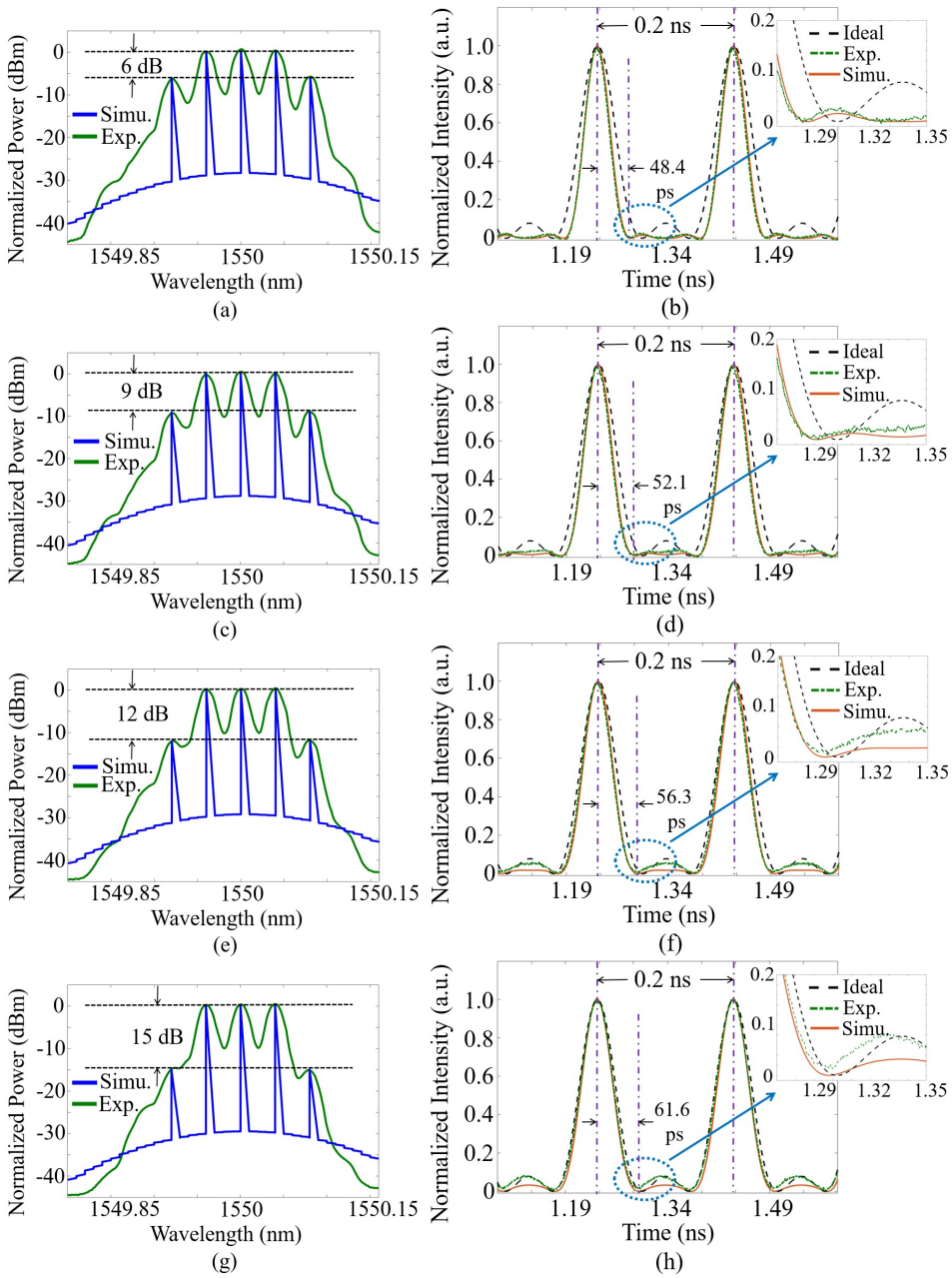


**Figure 3.6:** Three-line optical frequency combs (OFCs) and their respective sinc-shaped Nyquist pulses for different sideband suppression ratios (SSR): 6 dB (a, b), 9 dB (c, d), and 12 dB (e, f) taken from [82]. Additional 10 GHz lines are added to observe how the performance is limited at a lower SSR. In the frequency domain, the simulated spectra are illustrated in blue, while the experimentally measured spectra are depicted in green. The ideal sinc-shaped Nyquist pulse train without ripple and with a high sideband suppression ratio (SSR) of approximately 35 dB is shown in black. The simulated pulses and experimental pulses corresponding to various SSR levels are depicted in orange and green, respectively.

observe the effect of SSR at its limits.

The SSR for five-line and nine-line OFCs with a frequency spacing of 50 GHz and 0.02 ns repetition period $T_r$ is analyzed through simulations as illustrated in Fig. 3.8 and Fig. 3.9, respectively. The five-line OFC was generated by modulating two sinusoidal signals with a MZM at 50 GHz and 100 GHz, respectively. The nine-line OFC was produced with two cascaded MZMs, with the first MZM being modulated at 50 GHz and the second MZM at 150 GHz



https://doi.org/10.7795/110.20260421B

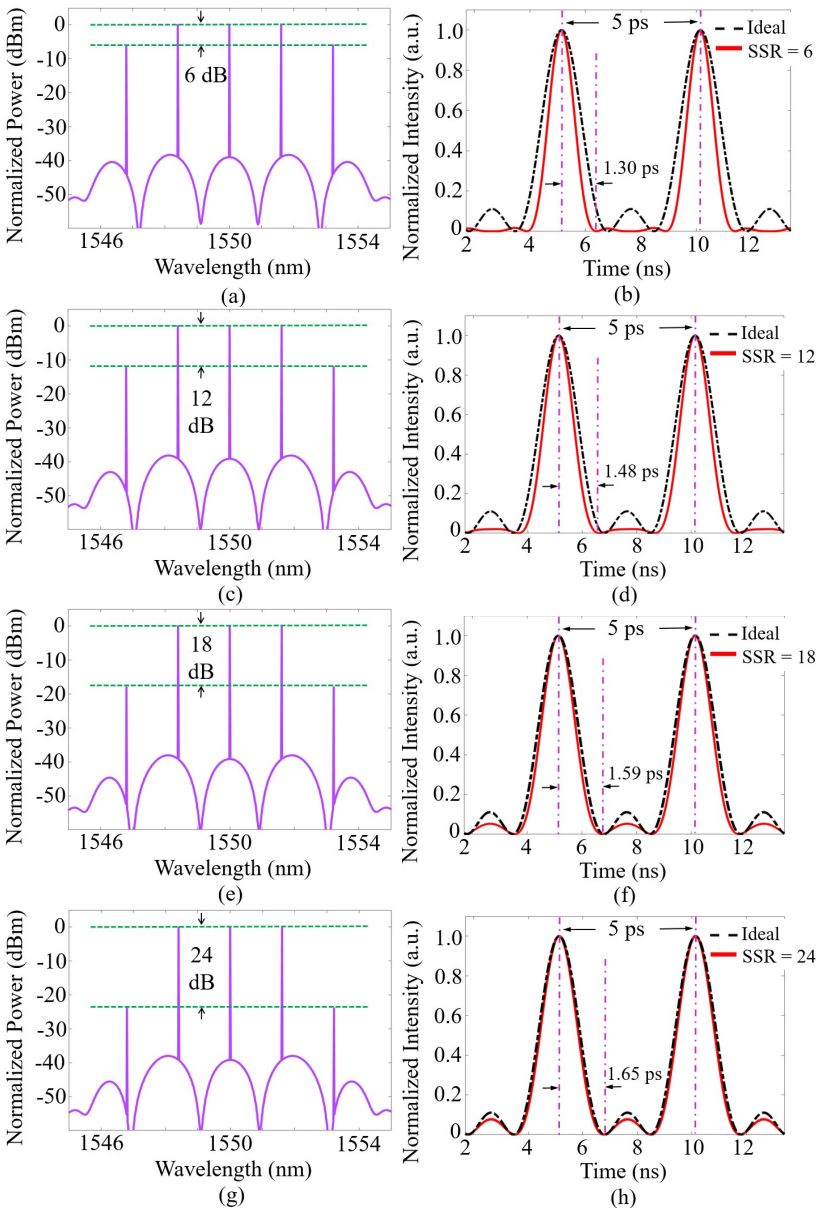


**Figure 3.7:** Three-line optical frequency combs (OFCs) and their respective sinc-shaped Nyquist pulses for different sideband suppression ratios (SSR): 6 dB (a, b), 12 dB (c, d), and 18 dB (e, f). In the frequency domain, the simulated spectra are illustrated in blue, while the experimentally measured spectra are depicted in green. The ideal sinc-shaped Nyquist pulse train without ripple and with a high sideband suppression ratio (SSR) of approximately 40 dB is shown in black. The simulated pulses corresponding to various SSR levels are depicted in red based on [121].

while being phase-locked to the first. The resulting sinc-shaped Nyquist pulses had FWHMs of 3.56 ps and 1.97 ps, and pulse durations $\tau_z$ of 4 ps and 2.22 ps for the five-line and nine-line combs, respectively. When the SSR is improved from 5 dB to higher values as depicted in Fig. 3.8 and Fig. 3.9, the FWHMs and the pulse durations $\tau_z$ are enhanced leading to more congruence of the simulated pulse sequences to the ideal signal. The RMSE was evaluated for increasing SSR values in Fig. 3.10 (a, b) suggesting a better performance for a nine-line OFC as compared to a five-line and three-line OFC; and a gradual reduction of RMSE even at 200 GHz frequency spacing for three-line combs. This occurs because as the number of comb lines



https://doi.org/10.7795/110.20260421B

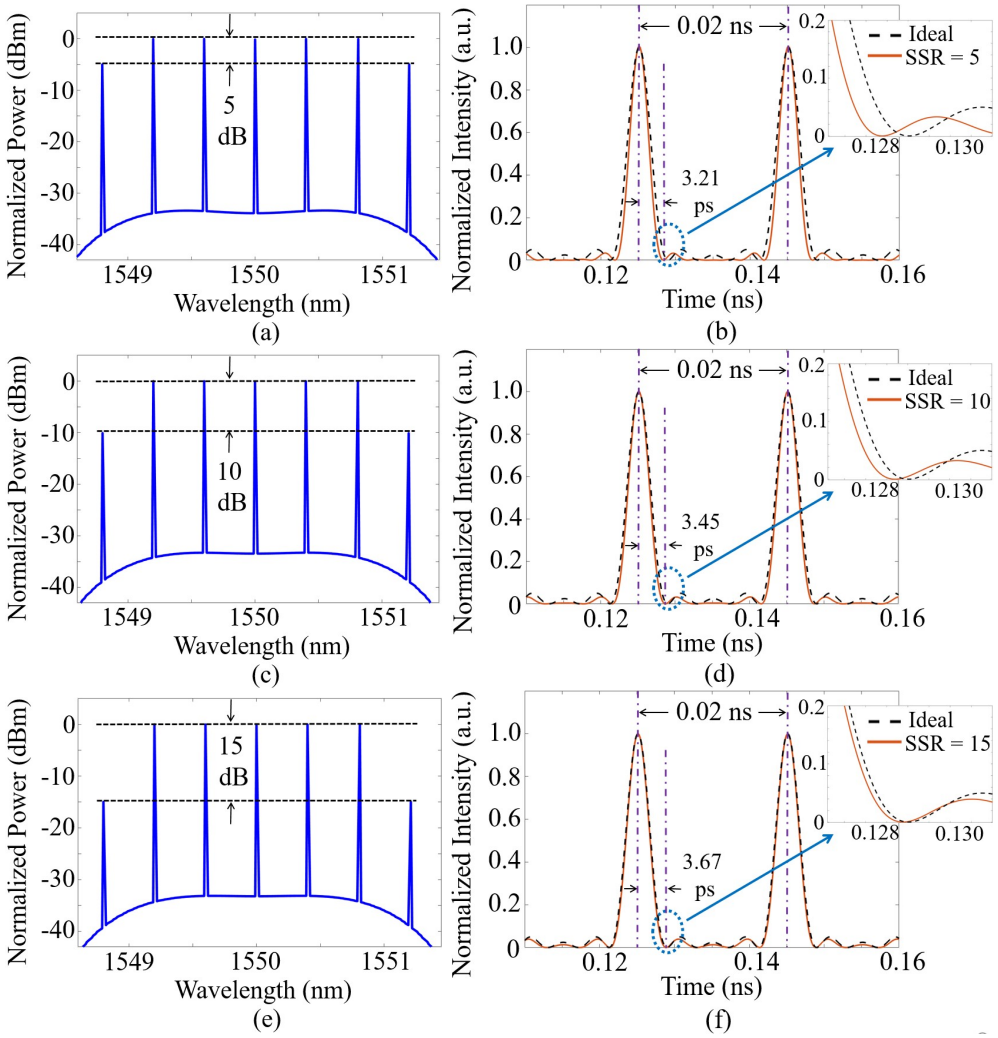


**Figure 3.8:** Five-line optical frequency combs (OFCs) and their respective sinc-shaped Nyquist pulses for different sideband suppression ratios (SSR): 5 dB (a, b), 10 dB (c, d), and 15 dB (e, f) taken from [82]. In the frequency domain, the simulated spectra are illustrated in blue, while the experimentally measured spectra are depicted in green. The ideal sinc-shaped Nyquist pulse train without ripple and with a high sideband suppression ratio (SSR) of approximately 35 dB is shown in black. The simulated pulses corresponding to various SSR levels are depicted in orange.

increases, the pulse width narrows down and the number of side lobes rises, contributing to a significant reduction of RMSE at higher SSR values.

One important factor to note here is that for the case of Nyquist pulse generation with MLLs, as the unwanted higher order sidebands are filtered out, there is a certain amount of power penalty as a consequence of the resulting optical power loss, that is being monitored at the input and output of the optical filter. This is clearly demonstrated through simulations in Fig. 3.11 for three-line, five-line, and nine-line OFCs denoted by red, green, and blue colors, respectively. Raising the SSR reduces the RMSE and improves the shape of the pulses. On the other hand, with increasing SSR the loss in power also increases, resulting in reduced optical power at the output. Hence, for an optimized system, the power efficiency should be balanced with signal accuracy, ensuing in a trade-off between the RMSE and the optical power loss. Notably, the nine-line OFC delivers the best pulse quality with the lowest RMSE at the



https://doi.org/10.7795/110.20260421B

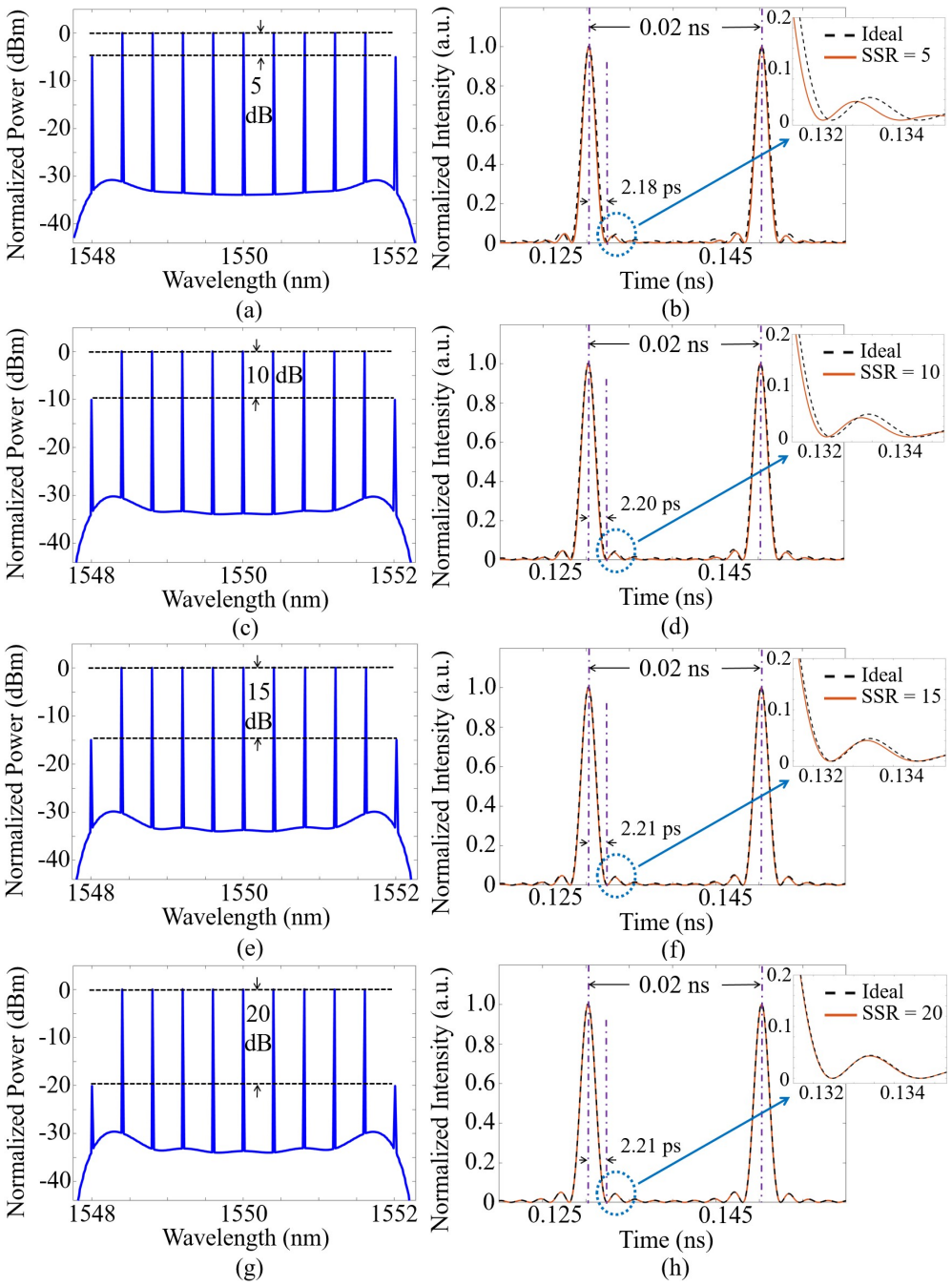


**Figure 3.9:** Nine-line optical frequency combs (OFCs) and their respective sinc-shaped Nyquist pulses for different sideband suppression ratios (SSR): 5 dB (a, b), 10 dB (c, d), 15 dB (e, f) and 20 dB (g, h) taken from [82]. In the frequency domain, the simulated spectra are illustrated in blue, while the experimentally measured spectra are depicted in green. The ideal sinc-shaped Nyquist pulse train without ripple and with a high sideband suppression ratio (SSR) of approximately 35 dB is shown in black. The simulated pulses corresponding to various SSR levels are depicted in orange.

cost of the largest power penalty. The optimal operating conditions for thee-line, five-line and nine-line OFCs can be identified with Fig. 3.11. In order to have an RMSE of less than 5 %, a three-line comb would need an SSR of around 15 dB with a power penalty of 2.5 dB. In case the RMSE preferred is even lower, then five-line combs and nine-line combs can offer optimal operating points. Importantly, for normal MZM based comb generation, recent experimental



https://doi.org/10.7795/110.20260421B

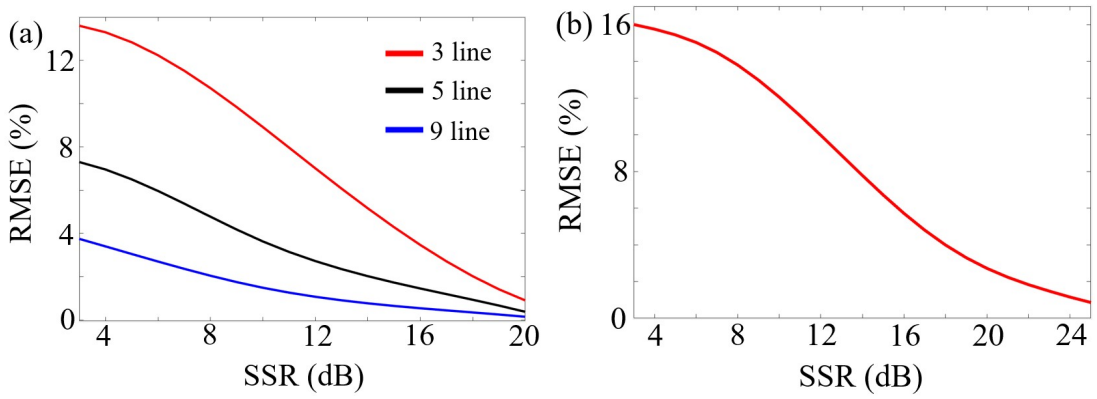


**Figure 3.10:** Comparative analysis of the root-mean-square errors (RMSE) (in %) for (a) three-, five-, and nine-line combs, and (b) for three-line comb at a frequency spacing of 200 GHz across various SSR levels taken from [82], [121].

works have demonstrated an SSR higher than 35 dB [123] and even for integrated modulators, the SSR is higher than 20 dB [124].

### 3.1.3 Impact of Optical filter roll-off

To ensure high quality in the sinc-shaped Nyquist pulses produced with MLLs, the higher-order sidebands are often filtered out with optical filters (OBPF) having a certain roll-off $\beta$; an overview of which is provided in the previous chapter in Section 2.4.3. Such Nyquist pulses can also be generated on an integrated platform using on-chip silicon MZMs [118] which does not need external optical filters as the unwanted sidebands are suppressed with modified modulator design and biasing. Nevertheless, with on-chip MZMs, we can still benchmark the system performance for scenarios that require an optical filter.

The on-chip silicon modulator as depicted in Fig. 3.12 (a, b) was designed on BiCMOS platform that combines advanced optical and electronic constituents on a single platform. This chip was developed by the System and Circuit Technology Group, Heinz Nixdorf Institut,

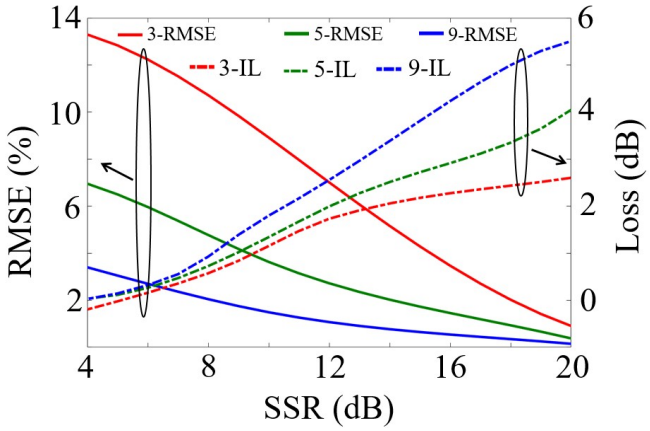


**Figure 3.11:** Diagram comparing RMSE and power penalty (in dB) as a function of sideband suppression ratio (SSR). The solid lines in red, green, and blue represent the simulated RMSE for the three-, five-, and nine-line combs, respectively, while the corresponding dotted lines indicate the power penalty (PP). Solid circles depict the optimum operating points for the corresponding frequency comb configuration.



https://doi.org/10.7795/110.20260421B

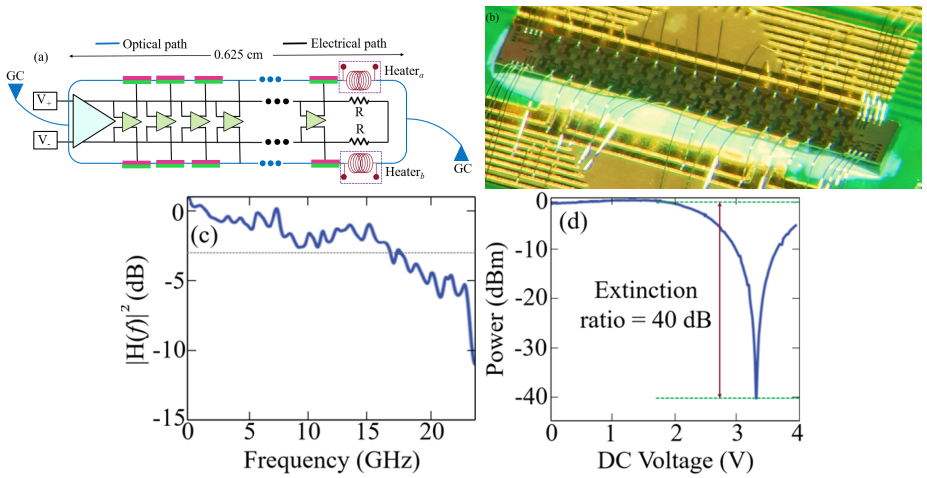


**Figure 3.12:** (a) Schematic block diagram of the modulator chip architecture. GC: Grating coupler. (b) PCB design of the fabricated on-chip Mach–Zehnder Modulator (MZM). (c) AC response of the modulator in frequency domain, showing a −3 dB bandwidth of 18 GHz. (d) DC transfer curve of the modulator based on [118], [120].

University of Paderborn [125] and in this thesis we have used it for the experiments. This includes multimode interferometers, grating couplers, Germanium photodiodes to check the bias points, and bipolar transistors operating at high frequencies ranging up to 220 GHz [125–127]. The integrated amplifier has a two-stage driver; where the first is used to provide a 50 Ω matching stage with amplification and the second is a distributed push-pull driver embedded along the transmission line along with interleaved driver-phase-shifter units. The measured eletro-optic response shows a 3 dB bandwidth of 18 GHz with an extinction ratio of 40 dB as per Fig. 3.12 (c, d). The modulator achieves a low $V_\pi$ of 420 mV [125], outperforming several designs made previously, while having a total power consumption of 1.8 W, supplied by the dual DC voltages of 3.5 V and 5 V. Here, $V_\pi$ represents the half-wave voltage or the voltage required to induce a phase shift of $\pi$ between the two arms of the interferometer in a MZM.

The experimental analysis was performed using the setup shown in Fig. 3.1, where the continuous wave (CW) laser is modulated at 1550.1 nm with an RF signal of 8.4 GHz produced with an RF generator (ANRITSU MG3692A). The modulation is carried out with the on-chip silicon MZM, where the ground-signal-signal-ground (GSSG) probe is used to provide the RF signal across the chip. An input optical power of 12 dBm was introduced into the system, and the total optical loss was measured to be 19 dB, accounting for 13 dB contribution from the grating couplers and the coupling interface. To evaluate the influence of roll-off on the Nyquist pulse quality, higher sidebands of second order were introduced at 16.8 GHz with a second RF source, in sync to the primary RF generator. The two RF signals were combined with a RF combiner and fed into the MZM with a bias-T. Nevertheless, as the bandwidth of the electrical combiner was limited up to 18 GHz, the first order sidebands were confined to 8.4 GHz spacing leading to a three-line frequency comb with a bandwidth of 25.2 GHz. The on-chip driver received an RF power of around 0 dBm, and the modulator was operated at a bias voltage ($V_{\text{bias}}$) of 2.7 V to generate a flat three-line OFC. Then an EDFA is used to boost the signal before passing through a Finisar Waveshaper 1000A tuned to 1550.1 nm which acts as



https://doi.org/10.7795/110.20260421B

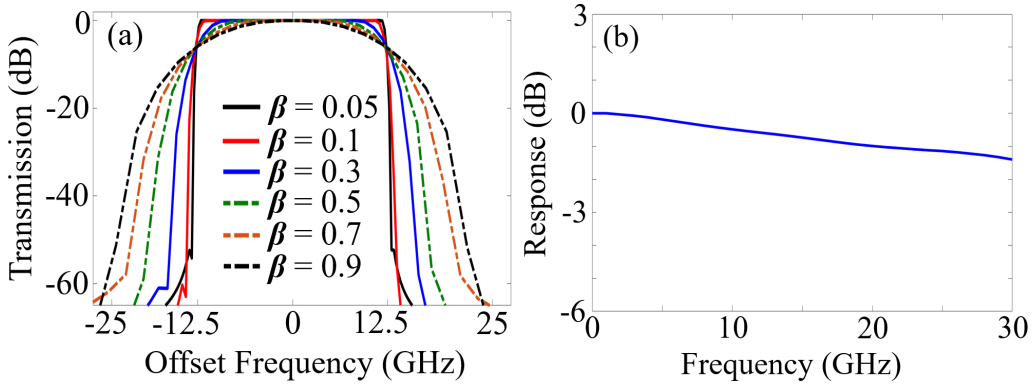


**Figure 3.13:** (a) Frequency-domain response of the optical bandpass filter (OBPF) measured for various roll-off factor values. (b) Measured response of the photodiode employed in the experimental setup [118].

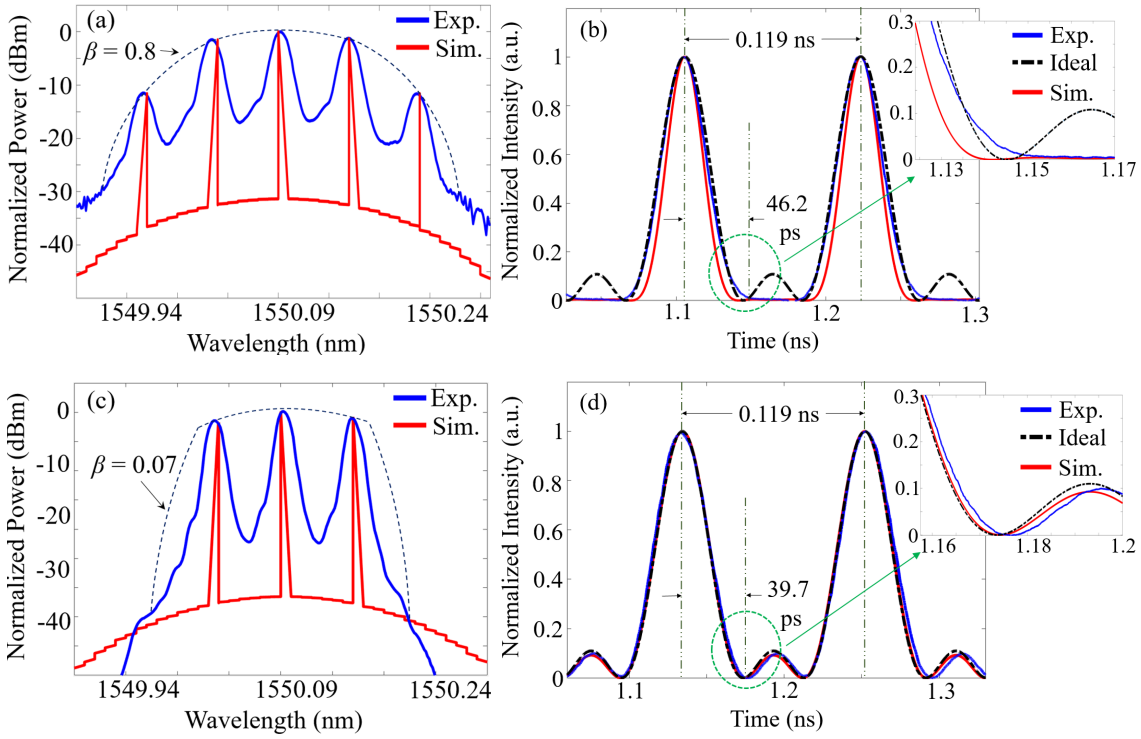


**Figure 3.14:** Three-line optical frequency combs (OFCs) and their respective Nyquist pulses for roll-off factors of 0.8 (a, b) and 0.07 (c, d). The ideal optical Nyquist pulses (i.e., $\beta = 0$) are depicted as dashed black lines in the time domain, and the simulated pulses for $\beta = 0.8$ and $\beta = 0.07$ are depicted in red [118].

the OBPF. The filter profile for different roll-off factors $\beta$ were generated using Lumerical [122] and loaded into the OBPF. For different values of roll-off $\beta$, the frequency response of the filter for a bandwidth of 25.2 GHz was measured as shown in Fig. 3.13 (a). The coupler was used to direct a majority of the power into the photodetector (Finisar XPDV21×0(RA)) with a 3 dB bandwidth of 50 GHz, which has a measured photodiode response as shown in Fig. 3.13 (b) and is connected to the electrical sampling oscilloscope (Agilent 86100C) to observe the signal in the time domain. The remaining power was applied into the optical spectrum analyzer (OSA) (YOKOGAWA AQ3670C) for spectral analysis. The experimental results were compared with the simulation results in the frequency and time domain for different roll-off values as



https://doi.org/10.7795/110.20260421B

| Reference | Type of modulator | Number of OFC lines | Frequency spacing (GHz) | Pulse duration (ps) | RMSE (%) | Effect of roll-off $\beta$ |
|---|---|---|---|---|---|---|
| [26] | C-MZM[a] | 9 | 10 | 11.11 | 0.98 (SSR[d] > 27 dB) | U.A.* |
| [128] | $LiNbO_3$-DP-MZM[c] | 5 | 10 | 20 | 1.10 (SSR[d] = 31.2 dB) | U.A.* |
| [129] | Si-MZM | 3 | 12 | 27.77 | U.A.* | U.A.* |
| [130] | C-MZM[a] | 9 | 5 | 22.22 | 3.68 ($Rp^b$ = 2.92 dB) | U.A.* |
| [131] | Si-DP-MZM[c] | 5 | 10 | 20 | 3.8 ($Rp^b$ = 1.9 dB) | U.A.* |
| [132] | Si-DP-MZM[c] | 5 | 3.2 | 62.50 | 2.8 ($Rp^b$ = 0.8 dB) | U.A.* |
| [82] (This work) | $LiNbO_3$-MZM | 3 | 5 | 66.66 | 0.81 ($Ri^b$ = 0.5 dB) | Yes (Sim.) |
| [118] (This work) | ePIC-MZM[e] | 3 | 8.4 | 39.68 | 0.7 ($\beta$ = 0.07, $Ri^b$< 0.1 dB) | Yes (Exp.) |

C-MZM[a] = Cascaded MZM, $Rp^b$ = Ripple, DP-MZM[c] = Dual-parallel MZM,
SSR[d] = Sideband Suppression Ratio, U.A.* = Unavailable, Sim. = Simulation, Exp. = Experiment.

**Table 3.1:** Tabulation of parameters for sinc-shaped Nyquist pulse sequence generation with a variety of modulators.

illustrated Fig. 3.14.

For the three-line OFC having a frequency spacing of 8.4 GHz, the ideal Nyquist pulses have a FWHM of 35.31 ps, pulse repetition period $T_r$ of 119 ps, and a pulse duration $\tau_z$ of 35.31 ps. The roll-off $\beta$ of the filter is changed to see the impact on the Nyquist pulses in the time domain considering an optical filter bandwidth of 25.2 GHz. For $\beta$ values close to zero, the filter follows the rectangular shape more closely eliminating the higher order sidebands enhancing the pulse quality in the time domain as per Fig. 3.14 (c, d). For such a three-line OFC, the influence of the sidebands become more visible when $\beta > 0.33$. For a higher roll-off $\beta$ of the filter, the pulse quality is degraded as depicted in Fig. 3.14 (a, b). This high roll-off $\beta$ can lead to ripple in the comb spectrum that can be countered by proper modulator bias adjustment thus enhancing carrier suppression.



https://doi.org/10.7795/110.20260421B

## 3.2 Conclusion

To summarize, this chapter provides a thorough investigation of the critical non-idealities that impact the generation of sinc-shaped Nyquist pulses. Considering the generation of Nyquist pulses with MLLs, the comb ripple and SSR were examined for three-line, five-line, and nine-line combs and it was ascertained that the nine-line OFCs have the best performance with the lowest RMSE. Additionally, for an optimized performance, a trade-off was obtained between the RMSE and the optical power loss. Using integrated platform involving the use of on-chip silicon MZMs as a benchmark for scenarios that need an optical filter, the effect of roll-off $\beta$ was analyzed revealing the best performance for lowest $\beta$ values.

A tabulation of our works [82, 118] to analyze the effect of non-idealities along with previous studies demonstrating Nyquist pulse generation is provided in Table 3.1. Two cascaded silicon MZMs were employed in [26] and [130] to generate Nyquist pulses, reporting a frequency spacing of 10 GHz and 5 GHz with an RMSE of 0.98 % and 3.68 %, respectively. Dual-parallel $LiNbO_3$ MZMs can support the generation of Nyquist pulses with an RMSE of 1.10 % [128]. On silicon platform, high quality Nyquist pulses can be produced with dual-parallel MZMs [130, 131] with a minimum RMSE of 2.8 %. In our works [82, 118], the influence of non-idealities such as comb ripple, sideband suppression, and optical filter roll-off $\beta$ is analyzed. To achieve this, the experimental setup was purposely configured to make the impairments measurable. For $LiNbO_3$ MZMs, our work [82] has produced high-quality Nyquist pulse sequences with low comb ripple and high SSR. With an integrated on-chip silicon MZM, our study [118] of optical filter roll-off $\beta$ has demonstrated a minor RMSE of 0.7 %.

Therefore, for processing high-bandwidth signals at the transmitter side, generating high-quality Nyquist pulse sequences with a low ripple and high SSR is possible with proper bias control of the MZM. For Nyquist pulse generation with MLLs, having a lower roll-off $\beta$ of the optical filter helps in improving the quality of the pulses. In the following chapter, such system imperfections are analyzed in detail for a direct detection (DD) based optical sampling systems which employ a simple system with only a single photodiode at the receiver.



https://doi.org/10.7795/110.20260421B

# 4

# Non-idealities Investigation in Direct Detection Systems

Based on the findings obtained from evaluating the non-idealities in Nyquist pulse generation, it is evident that the system non-idealities should be investigated thoroughly to transmit signals effectively at very high data rates [133–138] in the current and future networks, including transmission up to 1 Tbps [139]. With conventional electrical methods, processing such high bandwidth signals is quite challenging. A feasible alternative is to down-convert [140, 141] these signals into parallel low-bandwidth signals, making them easier to handle with the existing low bandwidth electronics. It is possible to undergo high-bandwidth signal measurements with a multitude of sampling techniques involving electrical samplers, like the electrical sample-and-hold circuits or the optical samplers [142–144]. Nevertheless, with increasing bandwidths the performance deteriorates for the electronic samplers owing to the clock jitter [145] and increased sampling errors. In order to correct these systematic errors, it is necessary to perform additional signal processing, which further expands the system complexity and energy consumption.

A viable alternative to conventional sampling involves the use of flat optical frequency combs (OFC)s in optical modulators for orthogonal sampling thus ensuring high bandwidth and error-free performance under ideal conditions [84, 146]. Integrated optical modulators have demonstrated bandwidths as high as 176 GHz while keeping the thermal crosstalk [96, 105] at a minimum. Such devices are able to perform the sampling of signals up to three times their own bandwidth while utilizing a three-line flat OFC [130, 131]. This design inherently eliminates any aperture jitter, enabling the low-jitter characteristics of the integrated oscillators to directly translate to a remarkably higher effective number of bits (ENOB) [34, 37].

Previous research has relied on coherent detection (CD) schemes [37, 147–152] to convert the sampled optical signals into electrical form. An overview of the coherent detection method is provided in Section 2.5.1. A viable, cost-effective, and simpler alternative to CD is direct detection (DD) [38, 39] which is very popular in data centers, access networks, and handheld consumer devices. In DD systems, the hardware is much simpler with no requirement of LO as discussed in Section 2.5.2.

Nevertheless, nonlinearities and noise remain critical sources of error in optical signal processing, particularly in DD systems. Hence, for a comprehensive metrological assessment of



https://doi.org/10.7795/110.20260421B

the complete sampling system, it is necessary to compute the response of the system to such imperfections. In this thesis, the effect of comb ripple on the performance of orthogonal sampling is analyzed for a three-line OFC system [119, 153]. Additionally, in DD systems, an optical filter having a bandwidth equal to the comb frequency spacing is essential for signal detection with a photodiode [90, 154], which might deteriorate the signal quality. To examine this signal degradation, the sampling quality is studied for sinusoidal [90] and broadband input signals [154] for different roll-off factors of the optical filter. All in all, the effect of comb ripple and optical filter roll-off $\beta$ on a DD-based orthogonal sampling system is examined in terms of error parameters like RMSE, SINAD, and ENOB [90, 119, 153, 154].

## Supporting Publications

### Journal Articles

- Y. Mandalawi, J. Meier, K. Singh, M. I. Hosni, **S. De** and T. Schneider, "Analysis of Bandwidth Reduction and Resolution Improvement for Photonics-Assisted ADC," in *Journal of Lightwave Technology*, 41(19), 6225–6234, 2023, [37].

- Y. Mandalawi, M. I. Hosni, J. Meier, K. Singh, **S. De**, R. Das, and T. Schneider, "Integrated segmented IQ-modulator for orthogonal sampling and multi-level high-bandwidth signal generation," *Optics Letters*, vol. 49, no. 9, pp. 2193–2196, 2024, [147].

### Book Chapters

- **S. De**, Y. Mandalawi, R. Das, and T. Schneider, "Metrological Analysis of Non-idealities for Photonics Assisted Signal Processing," in T. Kürner, T. Doeker, T. Kleine-Ostmann, T. Schneider, D. Humphreys (editors), *Metrology for THz Communications - Findings from DFG FOR 2863 Meteracom, Springer Nature*, November 28$^{\text{th}}$, 2025 [119].

- **S. De**, Y. Mandalawi, and R. Das, "Error Metrics for Photonics Assisted Signal Processing," in T. Kürner, T. Doeker, T. Kleine-Ostmann, T. Schneider, D. Humphreys (editors), *Metrology for THz Communications - Findings from DFG FOR 2863 Meteracom, Springer Nature*, November 28$^{\text{th}}$, 2025 [155].

### Conference Proceedings

- **S. De**, J. Meier, Y. Mandalawi, K. Singh, A. Venugopalan, D. Yadav, R. Das, N. Meyne, K. Baaske, T. Kleine-Ostmann, and T. Schneider, "Comb flatness dependence for orthogonally sampled high bandwidth signals," in *Proc. SPIE 12994, Terahertz Photonics III*, paper 1299407, 18 June 2024, [153].

- **S. De**, J. Meier, Y. Mandalawi, A. Venugopalan, P. Mandal, R. Das, N. Meyne, K. Baaske, T. Kleine-Ostmann, and T. Schneider, "Optical Filter Roll-off Analysis for Orthogonal Sampling in a Direct Detection System," in *Proc. 2025 16th German Microwave Conference (GeMiC)*, pp. 45–48, 2025, [90].



https://doi.org/10.7795/110.20260421B

- **S. De**, J. Meier, Y. Mandalawi, R. Das, N. Meyne, K. Baaske, T. Kleine-Ostmann, and T. Schneider, "Orthogonal Sampling with a Single Photodiode," in *Proc. 2025 Conference on Lasers and Electro-Optics Europe & European Quantum Electronics Conference (CLEO/Europe-EQEC)*, Munich, Germany, 2025, (accepted) [154].

- Y. Mandalawi, **S. De**, M. I. Hosni, L. Zhou, and T. Schneider, "Integrated Wideband Wireless Signal Receiver Based On Cascaded Ring Modulators," accepted at *50th International Conference on Infrared, Millimeter, and Terahertz Waves (IRMMW-THz)*, 2025, [148].

- Y. Mandalawi, J. Meier, M. I. Hosni, K. Singh, **S. De**, E. Baidoo, and T. Schneider, "Photonics Assisted Analog-to-Digital Conversion of Wide-Bandwidth Signals by Orthogonal Sampling," in *Proc. 2023 53rd European Microwave Conference (EuMC)*, pp. 464–467, 2023, [149].

- Y. Mandalawi, J. Meier, K. Singh, M. I. Hosni, **S. De**, S. Preußler, and T. Schneider, "High-Bandwidth Signal Reception with Improved ENOB by Frequency-Time Coherence Photonics Sampling," in *Optica Advanced Photonics Congress 2022, Technical Digest Series* (Optica Publishing Group, 2022), paper SpTu4J.4, [150].

- Y. Mandalawi, M. I. Hosni, J. Meier, **S. De**, L. Zhou, and T. Schneider, "Integrated Ring Modulator Based High-Speed Optical Sampler for Wireless Signals," in *Proc. 2025 16th German Microwave Conference (GeMiC)*, Dresden, Germany, pp. 37–40, 2025, [151].

- Y. Mandalawi, M. I. Hosni, K. Singh, J. Meier, **S. De**, R. Das, and T. Schneider, "Segmented Mach-Zehnder Modulator for Orthogonal Sampling Based High Bandwidth THz Transmitters," in *Proc. 2024 15th German Microwave Conference (GeMiC)*, pp. 45–48, 2024, [152].

## 4.1 Error parameters for the investigation of non-idealities

The effective number of bits or ENOB [156–158] acts as a key metric to express the resolution of both ADCs and DACs. It is derived from the signal-to-noise and distortion ratio or SINAD measured for the sampled and digitized signal and formulated as [37, 155, 158, 159]:

$$ENOB = \frac{SINAD - 1.76}{6.02} \tag{4.1}$$

The SINAD is evaluated from the frequency domain representation of the sampled signal which necessitates transforming the trace in the time domain into frequency domain with a Fast Fourier Transform or FFT. Thereafter, the ratio of the desired signal component to all the other spectral components, taking into account the noise and distortion, is evaluated. As specified by the Institute of Electrical and Electronics Engineers (IEEE) standards to characterize the ADC, the input signal utilized for testing or the signal-to-be-sampled should be a sine wave [160]. Additionally, the SINAD can be computed in the time domain with the



https://doi.org/10.7795/110.20260421B

RMSE of the sampled time-domain data as compared to the fitted sine wave, and expressed as [34]:

$$SINAD = \frac{A}{\sqrt{2} \cdot RMSU} = \frac{1}{\sqrt{2} \cdot 2 \cdot RMSE} \tag{4.2}$$

Here, $A$ represents the signal amplitude of the reference waveform, $RMSU$ denotes the unnormalized root-mean-square noise and distortion in the time domain, and RMSE stands for the normalized root-mean-square error. As the normalization is performed taking into consideration the difference between the maximum and minimum values of the signal, the factor 2 appears in front of the RMSE. The method for RMSE evaluation is illustrated in Section 3.1.

## 4.2 Direct detection concept and orthogonal sampling

A brief overview of the direct detection (DD) system is provided in Section 2.5.2. An architectural representation of a three-branch DD optical sampling system is illustrated here in Fig. 4.1 (a). At the transmitter side, the system has a CW laser which acts as the optical source and it is modulated with the input electrical signal using the modulation block. The modulated optical signal is then transmitted over a length ($L$) of the optical fiber and then divided into three branches with a power splitter. Each branch undergoes optical sampling utilizing sinusoidal RF signals that are phase shifted by 0°, 120°, and 240°, respectively [34, 37, 84, 90]. These phase offsets allow for orthogonal sampling across the three branches, ensuring precise reconstruction of the original signal. Orthogonal sampling is implemented by using phase-shifted RF signals such that every branch captures complementary components of the input signal. The 120° phase separation ensures linear independence of the samples, ensuring precise reconstruction of the original signal with reduced electronic bandwidth. Thereafter each of the sampled signals is passed through an optical filter (OF) followed by its consequent detection with a photodetector (PD). This OF restricts the spectral width of the signal before detection, thus decreasing noise and mitigating the effects of aliasing. For coherent detection (CD), such additional optical filter is not important as the system has build-in selectivity and can capture amplitude and phase directly. Under ideal circumstances, the optical filter should exhibit a rectangular spectrum. Nonetheless, practical implementations typically use raised cosine filters with a certain roll-off $\beta$, the frequency domain of which is shown in Fig. 4.1 (b) for different roll-off values: $\beta = 0$, 0.5, and 1 [82, 90].

A comprehensive theoretical framework for high bandwidth signal detection with low bandwidth electronics via orthogonal sampling without additional optical filtering using coherent detection (CD) systems has been presented by our working group in [34]. For computing the key performance parameters like ENOB, SINAD, a sinusoidal input signal with frequency $f_i$ can be taken into consideration. This signal is then convoluted with a $N$-line OFC characterized by $\Delta f$ frequency spacing and an overall bandwidth $B = 3\Delta f$, where $N$ is the number of comb lines taken as three for the simplest scenario. With a CD scheme, the down-converted signal after multiplication can be directly detected with electronics operating at a reduced bandwidth of $\frac{B}{2N}$. In contrast, DD-based systems use a single photodiode with an optical filter with a bandwidth $B_f = \frac{B}{N} = \Delta f$ before the photodiode as illustrated in Fig. 4.2 (a)



https://doi.org/10.7795/110.20260421B

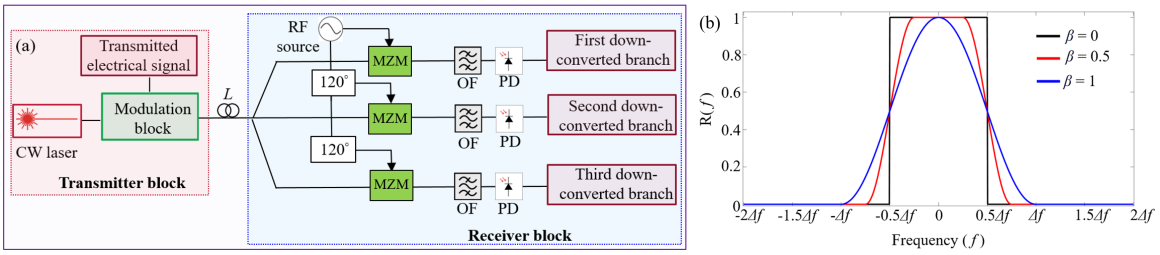


**Figure 4.1:** (a) Structural representation of a DD system considering a three-branch sampling system. (b) Raised cosine filter (OF) characteristics for various roll-off values ($\beta$) based on [90].

[119, 153]. With this scenario, the comb ripple analysis is performed considering an ideal rectangular optical filter with $f_i = 12$ GHz and $\Delta f = 16$ GHz. For the optical filter roll-off $\beta$ analysis the convolution illustration is shown in Fig. 4.2 (b), considering an input frequency $f_i$ of 12 GHz and a $\Delta f$ of 10 GHz with the optical filter having a bandwidth of $B_f = (1+\beta)\Delta f$ [90]. As depicted in the Figures 4.2 (a) and (b), the convolution operation demonstrates the interaction of the input spectrum with the frequency response of the filter. In each case, the colored box in the rightmost figure represents the signal that is filtered by the optical filter after convolution, thereby showcasing the effect of different roll-off values on the transmitted signal constituents in the frequency domain.

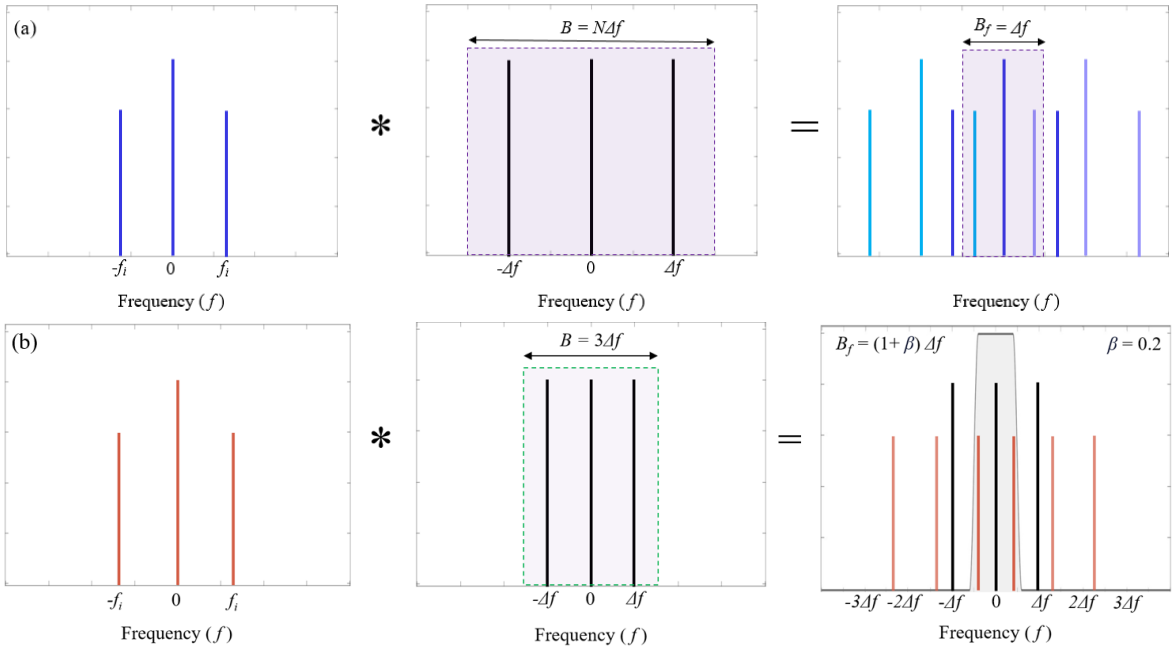


**Figure 4.2:** (a) Convolution illustration of the signal to be sampled having a frequency $f_i$ with a 3-line frequency comb incorporating a spacing of $\Delta f$ based on [119], [153]. Here, a rectangular optical filter is assumed. (b) The sinusoidal signal to be sampled having a frequency $f_i$ (left) is convoluted with a 3-line frequency comb incorporating a spacing of $\Delta f$ (middle), and the outcome is shown at the right. The grey box (bottom right) depicts an optical filter having a roll-off of 0.2 and a bandwidth of $1.2\Delta f$. It is important to observe that for the single branch, $f_i$ is greater than $\Delta f$. Therefore, all three branches are necessary for complete sampling of the signal content [90].



https://doi.org/10.7795/110.20260421B

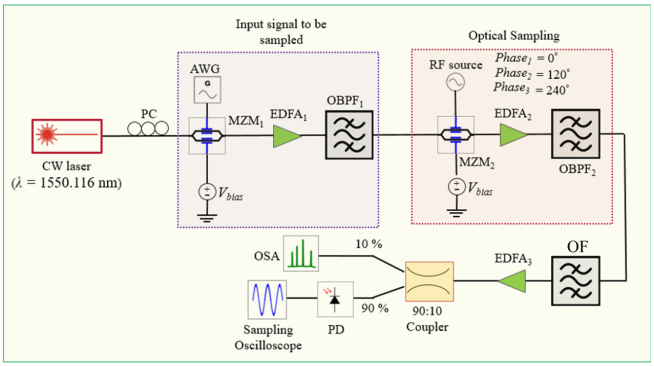


**Figure 4.3:** Experimental setup illustrating orthogonal sampling of the generated sinusoidal signal using the Mach-Zehnder Modulator ($MZM_1$), where the filter/waveshaper (OF) with a roll-off $\beta$ has a bandwidth of $(1+\beta)\Delta f$ where $\Delta f$ represents the frequency spacing of the comb lines produced by the $MZM_2$ based on [90]. For the comb ripple analysis, a rectangular filter is considered with $\beta$ as 0 and a bandwidth of $\Delta f$ [119], [153].

## 4.3 Comb Ripple Analysis

### 4.3.1 Experimental Results

The experimental configuration for orthogonal sampling is depicted in Fig. 4.3 and it serves as the proof of concept for DD-based systems [119], [153]. For producing the signal to be sampled, the CW laser is externally modulated at 1550.116 nm with a 12 GHz RF signal given by an arbitrary waveform generator (AWG) (Tektronix AWG700001A) and a $LiNbO_3$-based $MZM_1$ (Optilabs IMC-1550-20-PM). Subsequently, the $EDFA_1$ (LiComm OFA-TCH) is used to amplify the modulated optical signal followed by $OBPF_1$ in order to suppress the amplified spontaneous emission (ASE) noise. The orthogonal sampling is performed by modulating the resulting signal using $MZM_2$ (Thorlabs LNA6213) with a 16 GHz RF signal. To carry out complete orthogonal sampling, the RF signal is phase shifted to 0°, 120°, and 240°, respectively, followed by filtering with the optical filter (OF, Finisar WaveShaper 1000s) which is tuned to have a passband of $\Delta f = 16\,\text{GHz}$. The 90:10 fiber coupler splits 90 % of the signal to be detected by the photodetector (PD, Thorlabs DX50AF) in the time domain with a sampling oscilloscope; and the remaining 10 % of the signal is detected in the frequency domain with an OSA. For each of the three digitally acquired phases-shifted signals, post-processing is performed to reconstruct the high frequency waveform. The frequency domain information for an OSA with $\Delta f = 16\,\text{GHz}$ with a comb ripple of 0.1 dB is depicted in Fig. 4.4 (a) and the reconstructed 12 GHz signal (blue) from the sampling points of the red, gray, and orange sinc pulse sequences is plotted in Fig. 4.4 (b) [119], [153]. The signal is reconstructed by a linear combination of the orthogonally sampled signals from each branch and the phase-induced orthogonality results in accurate recovery of the original waveform. These results affirm that orthogonal sampling can be used to reconstruct waveforms with less distortion provided the ripple is very low.

### 4.3.2 Simulation Results

Simulations were executed with [161] to evaluate the effect of comb ripple on the quality of



https://doi.org/10.7795/110.20260421B

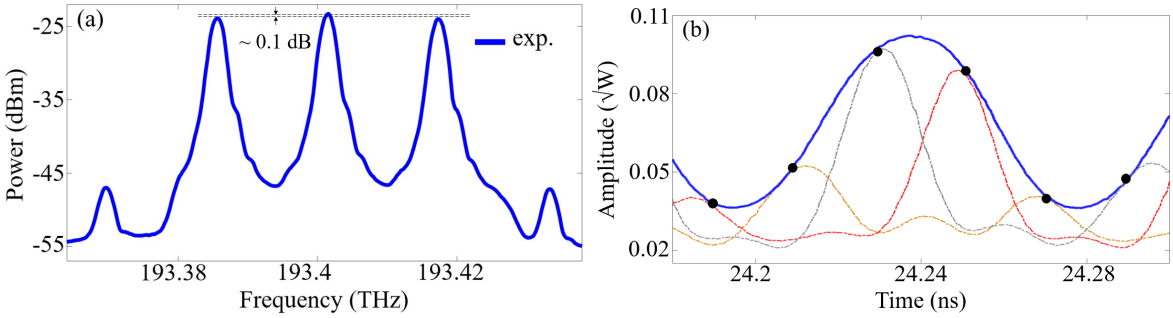


**Figure 4.4:** (a) The optical frequency comb having three lines spaced by 16 GHz produced with MZM-2 for optical sampling, displaying a positive ripple of 0.1 dB. (b) Depiction of the reconstructed sine wave in blue acquired from the sampling points of the gray, red, and orange sinc pulse sequences based on [119], [153].

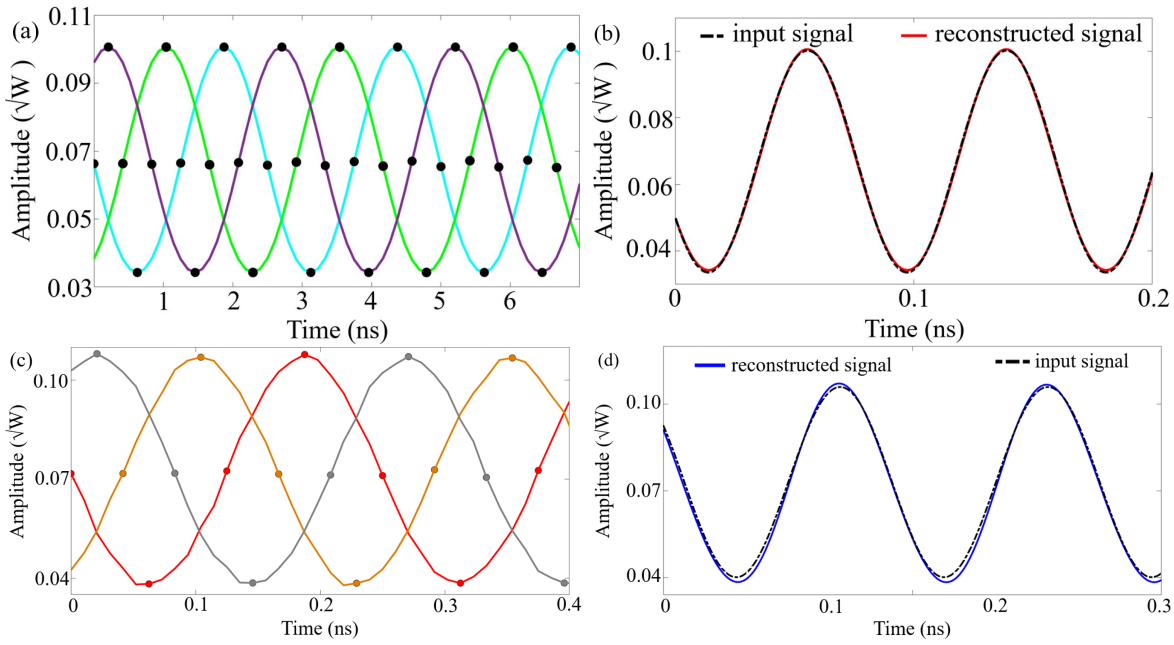


**Figure 4.5:** The waveform response at the ADC outputs corresponding to three different phase occurrences, i.e., 0°, 120°, and 240° and the comparison in time domain between the final 12 GHz reconstructed signal and the input signal for zero jitter based on [153] (a, b) and a system ADC jitter of 100 fs based on [119] (c, d). In both scenarios, the black dotted envelopes depict the sampling instances.

the signal. Considering an ADC jitter of zero and a positive ripple of 0.1 dB and an input sinusoidal signal with a frequency of 12 GHz, the reconstructed waveforms for three different phase shifts of 0°, 120°, and 240° after the ADC and the final reconstructed signal are depicted in Fig. 4.5 (a, b), respectively [153]. Additionally, for practical systems with 100 fs ADC jitter with 0.5 dB of positive ripple and same frequency of sinusoidal signal, the reconstructed waveforms and the final reconstructed result are illustrated in Fig. 4.5 (c, d), respectively [119]. For assessing the effect of comb ripple, simulations were done across a range of ripple values for both zero ADC jitter and 100 fs ADC jitter while considering an optical filter (OF) with a rectangular frequency response. For the case of zero ADC jitter, a perfectly flat comb with 0 dB ripple would result in an RMSE of zero and infinite ENOB and SINAD. Therefore, the RMSE, SINAD, and ENOB are evaluated starting at a positive jitter of 0.05 dB [153] as per Fig. 4.6 (a, b, c). For an ADC jitter of 100 fs, the respective RMSE, SINAD, and ENOB



https://doi.org/10.7795/110.20260421B

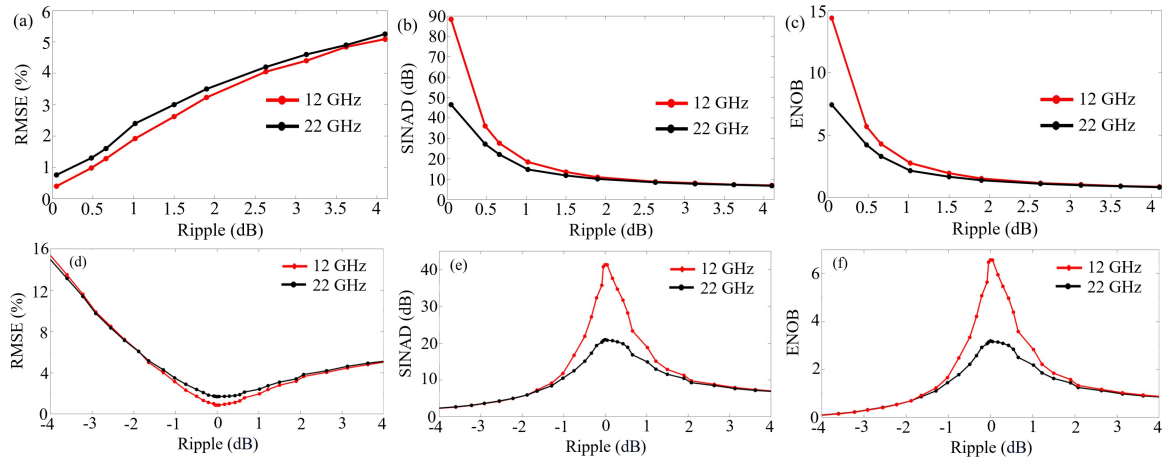


**Figure 4.6:** Comparison of the RMSE (a), SINAD (b) and ENOB (c) for different positive ripple values (in dB) for the zero jitter scenario based on [153]. For 100 fs ADC jitter, the RMSE, SINAD, ENOB is depicted in (d), (e), and (f) respectively for positive and negative values of jitter based on [119]. In every scenario, it is evaluated with sinusoidal input signals having frequencies of 12 GHz and 22 GHz.

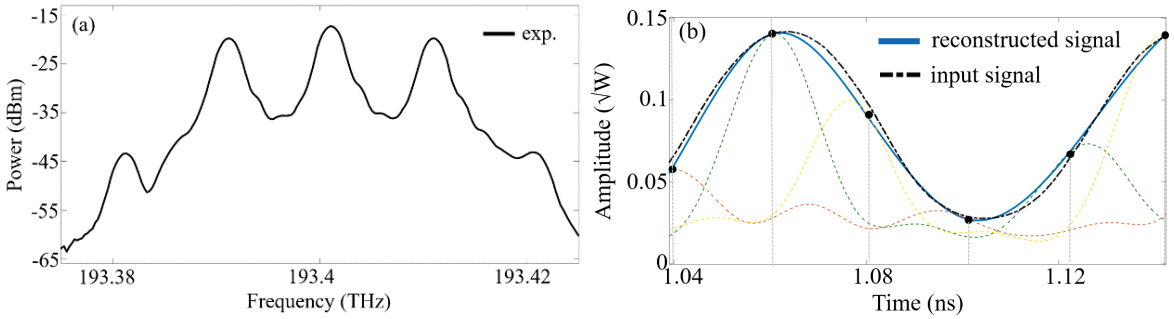


**Figure 4.7:** (a) Frequency domain of the three-line optical frequency comb having a spacing of 10 GHz produced by the $MZM_2$ and the corresponding reconstructed sine wave signal (b) generated from the sampling points of the sinc pulse sequences based on [90]. Here, the optical filter has a roll-off factor $\beta = 1$.

is computed for both positive and negative jitter values as illustrated in Fig. 4.6 (d, e, f) [119]. From these scenarios, it is ascertained that increasing the value of ripple in either directions has a negative impact on the sampled signal quality for a DD-based orthogonal sampling system with the negative ripple causing more RMSE than positive. This can be attributed to the higher attenuation of the essential spectral components for negative ripple ensuing in higher signal distortion.

## 4.4 Optical filter roll-off analysis

### 4.4.1 Experimental Results

In order to perform orthogonal sampling at a certain roll-off $\beta$ of the optical filter (OF), the setup is depicted in Fig. 4.3 [90, 119, 153]. The method and the components are previously discussed in Section 4.3.1 with certain changes in the parameters like frequency and bandwidth. The $MZM_1$ is modulated with a sinusoidal signal of frequency 12 GHz generated by the AWG and the frequency comb produced by $MZM_2$ has a line spacing of $\Delta f = 10$ GHz. The



https://doi.org/10.7795/110.20260421B

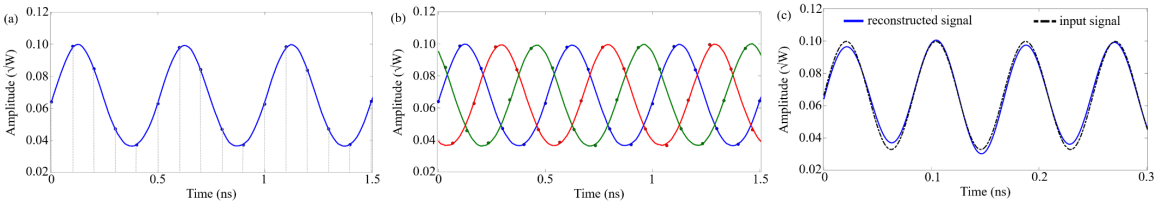


**Figure 4.8:** (a) The reconstructed down-converted waveform from the sampling points at the ADC output having an RF source phase of 0°. (b) The ADC output waveforms associated to RF phase instances of 0°, 120°, and 240°, respectively. (c) Comparative analysis of the final reconstructed waveform and the input 12 GHz input signal based on [90]. In every scenario, an optical filter (OF) with a roll-off factor of $\beta = 0.8$ is used and the ADC jitter is 100 fs.

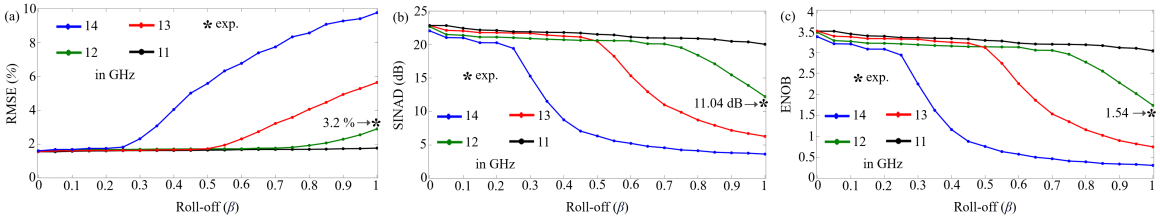


**Figure 4.9:** Evaluation of the (a) RMSE, (b) SINAD, and (c) ENOB across input frequencies of 11 GHz, 12 GHz, 13 GHz, and 14 GHz, over a range of roll-off values $\beta$ from 0 to 1, based on [90]. In every scenario, the jitter of the electronic ADC is taken as 100 fs. The experimental results with an input frequency of 12 GHz are denoted with an asterisk (*).

modulated signal at each of the three phases i.e. 0°, 120°, and 240° of the RF source is passed through the programmable optical filter (OF, Finisar WaveShaper 1000s) with a roll-off $\beta = 1$ after which it is detected with the photodetector (PD, Thorlabs DX50AF) in the time domain with a sampling oscilloscope. The final signal reconstruction is evaluated considering all the three phases via offline signal processing. The three-line OFC used for optical sampling with a frequency spacing of $\Delta f = 10$ GHz is illustrated in Fig. 4.7 (a), and the reconstructed 12 GHz signal (blue) from the sampling points of the respective sinc pulse sequences is depicted in Fig. 4.7 (b) and the RMSE is measured to be 3.2 %.

### 4.4.2 Simulation Results

Using Optisystem [161], the system performance is evaluated across a range of input frequencies, namely, 11 GHz, 12 GHz, 13 GHz, and 14 GHz considering the three-line OFC of $\Delta f = 10$ GHz and an ADC jitter of 100 fs. The simulations are performed in a system-level environment, where the required component models were taken from the library and the parameters were adjusted as per our requirements. With the input frequency as 12 GHz and the optical filter roll-off $\beta$ as 0.8, the output of the ADC is evaluated for a phase of 0° as per Fig. 4.8 (a). Considering all the three RF phases of 0°, 120°, and 240°, the ADC outputs are depicted in Fig. 4.8 (b). A complete signal reconstruction, along with a comparison with the original waveform, is illustrated in Fig. 4.8 (c) and the RMSE is calculated to be 1.92%. The error parameters like RMSE, SINAD, and ENOB are evaluated with the expressions listed previously in (3.1), (4.2), and (4.1) for the optical filter roll-off $\beta$ ranging from 0 to 1 as depicted in Fig. 4.9 (a), (b), and (c), respectively [90]. The results indicate that for a fixed input



https://doi.org/10.7795/110.20260421B

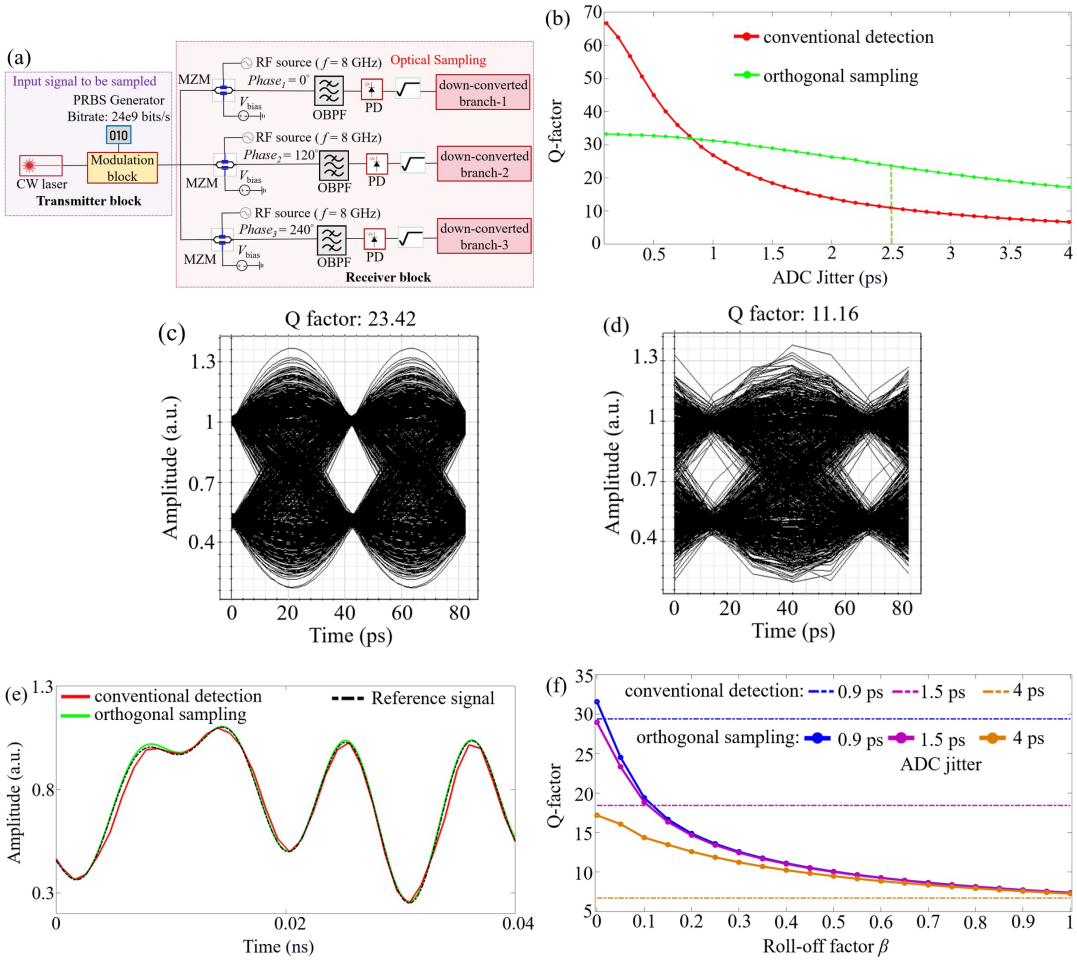


**Figure 4.10:** (a) Schematic diagram of orthogonal sampling of a broadband signal with a three-line frequency comb. PRBS generator: pseudorandom binary sequence generator, MZM: Mach-Zehnder modulator, RF source: Radio Frequency source, PD: Photodetector. (b) Evaluation of Q-factor across different ADC jitter values for the conventional detection i.e. direct detection (DD) with an ADC and our orthogonal sampling method. Eye diagram depiction for (c) our method and (d) the DD method with an electronic ADC. (e) Output waveform comparison the conventional detection i.e. direct detection (DD) with an ADC and our orthogonal sampling method considering an ADC jitter of 2500 fs and a roll-off $\beta = 0$. (f) Measurement of Q-factor across different ADC jitter values for the conventional detection i.e. direct detection (DD) with an ADC and our orthogonal sampling method over a range of roll-off values $\beta$ from 0 to 1, based on [154].

frequency, the RMSE remains nearly unchanged up to a specific threshold in the optical filter roll-off $\beta$ beyond which it begins to increase significantly. In parallel, both the SINAD and ENOB showcase a sharp decline after this threshold $\beta$. This behavior can be attributed to the frequency domain response of the optical filter previously illustrated in Fig. 4.2 (b), where the convoluted signal in the frequency domain is distorted after the filter has reached a certain roll-off $\beta$ value.

### 4.4.3 Broadband input simulation setup and results

The simulated orthogonal sampling system with three-line OFC for a DD system for a broadband signal as input is illustrated in Fig. 4.10 (a) [154]. The input signal is produced with a



https://doi.org/10.7795/110.20260421B

pseudo-random bit sequence (PRBS) generator at 24 Gbits/s via the first Mach-Zehnder modulator ($MZM_1$). The sampling is performed at each of the three branches with an RF signal operating at phase offsets of 0°, 120°, and 240°, respectively, with the second Mach-Zehnder modulator ($MZM_2$). The RF source at $MZM_2$ operates at a frequency of 8 GHz ensuring a frequency spacing of $\Delta f = 8\,\text{GHz}$ for the generated OFC. Thereafter, the down-converted signals are passed through an optical filter (OF) with a roll-off $\beta$ and subsequently detected with a photodetector (PD). After acquiring the signal from the three branches, the complete signal is reconstructed with offline signal processing. This method improves the bandwidth by a factor of 1.5 when compared to the conventional DD systems with electronic ADCs owing to the down-conversion, and a better quality of sampling in terms of the quality factor (Q-factor), particularly for greater values of ADC jitter as shown in Fig. 4.10 (b) considering the optical filter roll-off $\beta$ to be zero. For an ADC jitter of 2.5 ps, the enhancement in the eye diagram is evident in Fig. 4.10 (c, d) where the orthogonal sampling method shows a Q-factor of 23.42 while the conventional DD systems with electronic ADCs has a Q-factor of 11.16. For the same ADC jitter, a time domain comparison of the sampled and the reference signal for both the techniques is given in Fig. 4.10 (e). As depicted in Fig. 4.10 (f), increasing the optical filter roll-off $\beta$ from 0 to 1 reduces the Q-factor for orthogonal sampling method. Nevertheless, even for an ADC jitter of 1.5 ps, the orthogonal sampling method outperforms the conventional DD method up to an optical filter roll-off $\beta$ of 0.1. For a higher ADC jitter of 4 ps, the orthogonal sampling method ensures a superior performance even for an optical filter roll-off $\beta$ of 1.

## 4.5 Conclusion

In this chapter, a comprehensive analysis of non-idealities in a direct detection (DD) system with a three-line OFC based orthogonal sampling was performed while emphasizing two practical impairments, namely, comb ripple and optical filter roll-off $\beta$. This investigation provides simulation analysis and proof-of-concept experimental validation to ensure a detailed understanding of the effect of each of these impairments on signal integrity and overall performance of the optical system in a high-speed photonic sampling environment. Based on the examination, it is demonstrated that the orthogonal sampling with DD ensures effective down-conversion and signal reconstruction with reduced electronic bandwidth requirements.

For comb ripple analysis, it was observed that even minor deviations in the comb flatness could notably impact the fidelity of the reconstructed signal. This is particularly noticeable for systems with ADC jitters where the signal degradation for positive and negative comb ripple is reflected in terms of increased RMSE and reduced SINAD and ENOB. The robustness of the orthogonal sampling system to ripple is reduced, particularly when the ripple increases beyond 0.5 dB.

The impact of optical filter roll-off $\beta$ on the performance of a DD based orthogonal sampling system with sinusoidal input was ascertained revealing that the signal degradation remains quite low until a certain threshold, beyond which there is a rapid deterioration of performance. For broadband input signals, it was established that the orthogonal sampling consistently out-



https://doi.org/10.7795/110.20260421B

performed the conventional DD systems with electronic ADCs across different ADC jitter values and roll-off $\beta$ of the optical filter, while having a bandwidth enhancement of 1.5 owing to the down-conversion. The advantage in performance was clearly evident in terms of the quality factor and eye diagrams of the sampled signals at the output.

All in all, this chapter establishes that while orthogonal sampling in DD systems is fundamentally advantageous for sampling high bandwidth signals with low bandwidth electronics, its performance is critically impacted by practical imperfections in the system components. For practical ADC jitters, the analysis of comb ripple and optical filter roll-off $\beta$ collectively inform the trade-off in the design and tolerance viable for real-world deployment. The insights gained through the identification of acceptable bounds for the non-idealities contribute towards the design of next-generation high-speed, energy-efficient optical receivers using direct detection together with photonic integration. Nonetheless, in such PICs used for high bandwidth signal processing, a large amount of photonic components are placed very closely to one another resulting in the issue of thermal crosstalk, which hampers the overall performance of the optical system. The following chapter presents a comprehensive overview of thermal crosstalk and discusses design techniques to mitigate the same to achieve a crosstalk-alleviated integrated photonic platform capable of performing high bandwidth signal processing.



https://doi.org/10.7795/110.20260421B

# 5

# Mitigation of Thermal Crosstalk in Integrated Photonic Systems

With the help of the silicon photonics technology [18], it is feasible to have a compact and efficient realization of an assortment of electronic and photonic components on the same chip, and therefore undergo diverse optical functionalities like modulation, multiplexing, and wavelength filtering on the same chip. Among the wide range of platforms available, silicon-on-insulator (SOI) has surfaced as the most extensively implemented owing to its compatibility with the industry-standard CMOS fabrication process [18, 162] and the optical transparency of silicon in the infrared range. Consequently, these positive aspects enable streamlined integration of photonic components with electronic control circuits paving the way for applications in domains like telecommunications, optical interconnects, neuromorphic processing, and sensing.

Within these PICs, TOPS [163, 164] are pivotal for the above mentioned applications. The principle of operation involves the use of the thermo-optic effect [165], where the temperature modulation via a resistive micro-heater enables a refractive index change which ensures phase control of the guided optical signal. Typically, such heaters or PN junctions are integrated into complicated architectures like MZIs [166, 167], MZMs [162, 168, 169], or even ring resonators [170–173]. Nonetheless, the thermal conduction in the chip substrate triggers thermal crosstalk, which can critically impair the performance of phase shifters, modulators, attenuators [174, 175], and other integrated photonic components.

Over the past decades, a plenty of strategies have emerged to alleviate thermal crosstalk in PICs. Compact designs involving thin-film heaters with an air-filled trench to reduce thermal coupling were discussed in [176]. But the implementation in CMOS platforms is still a demanding task as it needs external heat absorbers. A $p^{++}$ doped silicon heater adaptable to CMOS platforms was engineered in [177], yielding lowered crosstalk at the expense of higher power consumption and footprint. The technique of time-multiplexed row-column addressing [178] was studied as well, but it is bounded by electrical design constraints. Microdisk resonator structures with built-in heater-modulators were reported in [179] for crosstalk analysis. Silicon Oxynitride (SiON) waveguides with metal heaters and the transform coordinate method (TCM) for modeling ring resonators were explored in [180]. The technique of thermal eigenmode decomposition (TED), which successfully neutralizes the phase coupling



https://doi.org/10.7795/110.20260421B

in microring resonator (MRR) and MZI based configurations, was investigated in [42, 181], depicting optimal performance when the phase coupling matrix (T) is ascertained and measured via integrated heaters. A concise overview of thermal crosstalk in passive photonic phase shifters is provided in [182], dealing mainly with passive components. A multitude of designs concerning low-crosstalk TOPS [183] were worked upon by our group at TU Braunschweig previously in [96].

This chapter expands on [96], and explores the thermal crosstalk and phase variation in different waveguide structures with metal and doped silicon heaters [105]. For effective thermal crosstalk mitigation, the deep trench designs have been thoroughly investigated for a multitude of photonic structures in PICs like different types of modulators [184–187], multi quantum well (MQW) lasers [188], avalanche photodetectors (APD) [189, 190] and uni-traveling carrier (UTC) photodetectors [191], switching networks [96, 192], etc. The study is further extended into the amorphous silicon platform which further suppresses the crosstalk [193], since it has a lower thermal conductivity as compared to crystalline silicon. Using these techniques, for a complete optical communication system using PICs [24, 120, 194–197], it can process high bandwidth signals with enhanced performance.

## Supporting Publications

### Journal Articles

- **S. De**, R. Das, R. K. Varshney, and T. Schneider, "CMOS-Compatible Photonic Phase Shifters With Extremely Low Thermal Crosstalk Performance," *Journal of Lightwave Technology*, vol. 39, no. 7, pp. 2113–2122, 2021, [105].

- K. Singh, R. Das, A. Venugopalan, **S. De**, M. I. Hosni, L. Zhou, and T. Schneider, "Real-time reconfigurable on-chip photonic frequency decoder," *Optics Express*, vol. 31, no. 19, pp. 30160–30170, 2023, [195].

### Book Chapters

- **S. De**, Y. Mandalawi, R. Das, and M. Weizel, "Integrated Photonics Assisted Signal Processing and Thermal Crosstalk," in T. Kürner, T. Doeker, T. Kleine-Ostmann, T. Schneider, D. Humphreys (editors), *Metrology for THz Communications - Findings from DFG FOR 2863 Meteracom, Springer Nature*, November 28$^{\text{th}}$, 2025 [120].

### Conference Proceedings

- **S. De**, R. Das, T. Kleine-Ostmann, and T. Schneider, "Athermal Travelling Wave Mach-Zehnder Modulators for Optical Interconnects," in *OSA Advanced Photonics Congress 2021, OSA Technical Digest*, Optica Publishing Group, 2021, paper NeF1B.4, [184].

- **S. De**, R. Das, T. Kleine-Ostmann, and T. Schneider, "Effect of Thermal Crosstalk on Travelling-wave Mach-Zehnder Modulator," in *Proc. 2021 Conference on Lasers*



https://doi.org/10.7795/110.20260421B

*and Electro-Optics Europe & European Quantum Electronics Conference (CLEO/Europe-EQEC)*, pp. 1–1, 2021, [185].

- **S. De**, R. Das, K. Singh, Y. Mandalawi, T. Kleine-Ostmann, and T. Schneider, "Thermal Crosstalk Mitigation in a Dual-Drive Mach-Zehnder Modulator," in *Proc. 2022 International Conference on Numerical Simulation of Optoelectronic Devices (NUSOD)*, pp. 27–28, 2022, [186].

- **S. De**, R. Das, K. Singh, Y. Mandalawi, T. Kleine-Ostmann, and T. Schneider, "Thermal Insulation of Silicon Ring Modulators in Densely-Packed Photonic Integrated Circuits," in *Proc. SPIE 12575, Integrated Optics: Design, Devices, Systems and Applications VII*, paper 125750C, 31 May 2023, [187].

- **S. De**, R. Das, K. Singh, Y. Mandalawi, T. Kleine-Ostmann, and T. Schneider, "Thermal-aware Multi-Quantum Well Laser," in *Frontiers in Optics + Laser Science 2022 (FIO, LS), Technical Digest Series*, Optica Publishing Group, 2022, paper JTu4A.51, [188].

- **S. De**, R. Das, K. Singh, Y. Mandalawi, T. Kleine-Ostmann, and T. Schneider, "Study of Thermal Crosstalk in Avalanche Photodetectors in THz Domain," in *Proc. 2022 47th International Conference on Infrared, Millimeter and Terahertz Waves (IRMMW-THz)*, pp. 1–2, 2022, [189].

- **S. De**, R. Das, K. Singh, Y. Mandalawi, T. Kleine-Ostmann, and T. Schneider, "Crosstalk Immune High-Speed Photonic Transmitter-Receiver System," in *Proc. 2024 15th German Microwave Conference (GeMiC)*, pp. 25–28, 2024, [194].

- **S. De**, R. Das, K. Singh, Y. Mandalawi, E. Baidoo, T. Kleine-Ostmann, and T. Schneider, "Crosstalk Resistant Integrated Uni-Traveling Carrier Photodetector," in *Proc. 2023 48th International Conference on Infrared, Millimeter, and Terahertz Waves (IRMMW-THz)*, pp. 1–2, 2023, [191].

- **S. De**, R. Das, K. Singh, Y. Mandalawi, T. Kleine-Ostmann, and T. Schneider, "Amorphous Silicon Based Crosstalk Resilient Photonic Phase Shifters," in *Proc. 2023 Conference on Lasers and Electro-Optics Europe & European Quantum Electronics Conference (CLEO/Europe-EQEC)*, pp. 1–1, 2023, [193].

- **S. De**, R. Das, K. Singh, Y. Mandalawi, T. Kleine-Ostmann, and T. Schneider, "Temperature Insensitive Avalanche Photodetectors," in *Optica Advanced Photonics Congress 2022, Technical Digest Series*, Optica Publishing Group, 2022, paper ITu3C.2, [190].

- **S. De**, Y. Mandalawi, A. Venugopalan, J. Meier, R. Das, K. Baaske, T. Kleine-Ostmann, L. Zhou, and T. Schneider, "Experimental Study of Thermal Crosstalk Alleviation in Thermo-Optic Phase Shifters," accepted for presentation at *Kleineheubacher Tagung 2025* [183].



https://doi.org/10.7795/110.20260421B

- R. C. Heim, **S. De**, R. Das, K. Singh, T. Kleine-Ostmann, and T. Schneider, "Thermal Crosstalk Alleviated Silicon Microring Switches," in *Conference on Lasers and Electro-Optics/Europe (CLEO/Europe 2023) and European Quantum Electronics Conference (EQEC 2023), Technical Digest Series*, Optica Publishing Group, 2023, paper ck_p_15, [192].
- R. Das, **S. De**, and T. Schneider, "On-chip Inductive Peaking to Boost the Silicon Modulator Bandwidth," in *OSA Advanced Photonics Congress 2021, Technical Digest*, B. Yang et al., Eds., Optica Publishing Group, 2021, paper NeF1B.2, [197].
- K. Singh, R. Das, A. Misra, **S. De**, M. I. Hosni, A. Venugopalan, L. Zhou, and T. Schneider, "Reconfigurable RF Frequency Sniffer Using Tunable Micro Ring Resonator," in *CLEO 2023, Technical Digest Series*, Optica Publishing Group, 2023, paper SW3O.5, [196].

## 5.1 Integrated heaters

Integrated heaters play a vital role in designing thermal phase shifters for PICs. In the SOI platform, two common heater configurations are used, namely, positioning the metal heater over the waveguide on the $SiO_2$ layer [96, 105, 198–200], and doped silicon heaters positioned adjoining the waveguide [96, 105, 200, 201]. A thorough summary of the integrated heater designs is given in [24, 202]. In this chapter, both of the heater types are examined to appraise the thermal crosstalk and phase performance considering rib and strip waveguides, respectively.

The phase shift brought about in the heated waveguide is governed by the temperature and thermo-optic coefficients of the silicon core and the silica cladding, and can be formulated as [96, 200]:

$$\Delta\phi = \frac{2\pi L \Delta T}{\lambda_0} \cdot \frac{dn_{\text{eff}}}{dT} \tag{5.1}$$

$$\frac{dn_{\text{eff}}}{dT} = \frac{dn_{\text{eff}}}{dn_{\text{Si}}} \cdot \frac{dn_{\text{Si}}}{dT} + \frac{dn_{\text{eff}}}{dn_{\text{SiO}_2}} \cdot \frac{dn_{\text{SiO}_2}}{dT} \tag{5.2}$$

In the expressions 5.1 and 5.2, $n_{\text{eff}}$ represents the mode's effective refractive index, $L$ denotes the length of the integrated heater, and $\lambda_0$ stands for the free-space wavelength. The temperature derivatives $\frac{dn_{\text{Si}}}{dT}$ and $\frac{dn_{\text{SiO}_2}}{dT}$ indicate the thermo-optic coefficients for silicon (Si) and silicon dioxide ($SiO_2$), which are around $1.8 \times 10^{-4}\,\text{K}^{-1}$ and $1 \times 10^{-5}\,\text{K}^{-1}$, respectively. Considering $\lambda_0 = 1550\,\text{nm}$ and $T = 300\,\text{K}$, $\Delta T$ which is the change in temperature, can be calculated for a phase shift of $\pi$ as:

$$\Delta T(\pi) = \frac{\lambda_0}{2L} \left( \frac{dn_{\text{eff}}}{dT} \right)^{-1} \tag{5.3}$$

In integrated phase shifters, the phase shift scales linearly with the rise in temperature above the ambient. Nonetheless, heat conduction within the chip material can ensue in thermal crosstalk in the adjacent structures. It is observed from 5.3 that increasing the heater length



https://doi.org/10.7795/110.20260421B

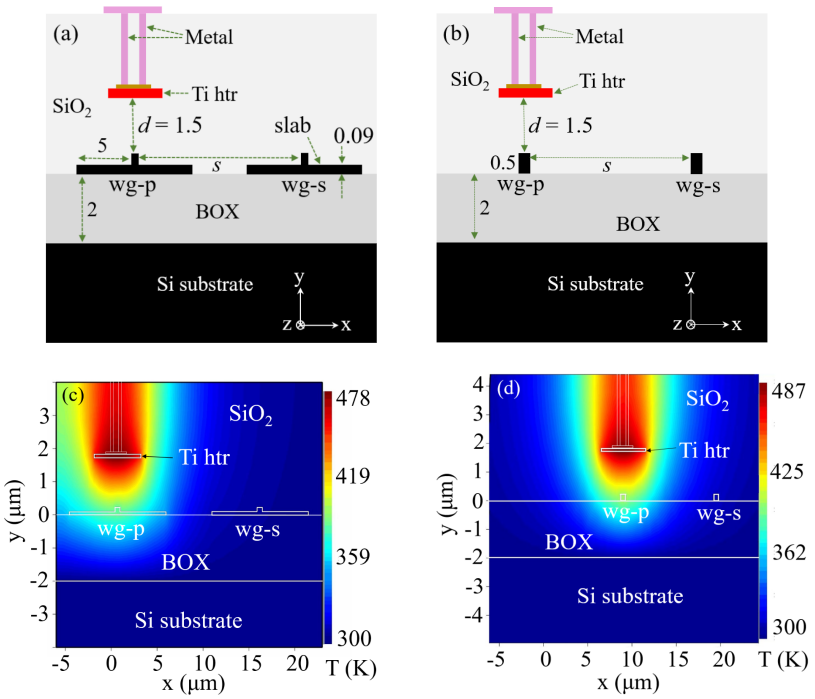


**Figure 5.1:** Structures of (a) rib and (b) strip waveguides having a titanium heater (Ti htr) with wg-p as the primary waveguide and wg-s as the secondary waveguide where the crosstalk is evaluated. The associated temperature distributions for a waveguide separation of $s = 15\,\mu$m and heater power of 211 mW are depicted in (c) and (d) for the rib and strip waveguides, respectively based on [105]. The $x$- and $y$-axes employ different scales, and dimensions are labeled in $\mu$m. The color bar represents the temperature in Kelvin (K), ranging from 300 K (blue) to a maximum of 478 K (red) in (c) and 487 K (red) in (d).

$L$ lowers $\Delta T$, eventually reducing the lateral thermal crosstalk. On the other hand, a longer heater results in a higher propagation loss with a larger device footprint. Consequently, the heat source is positioned closer to the waveguide so as to enhance the thermal efficiency of the heater while maintaining a small gap ($g$) between the waveguides to prevent the optical losses from the metal layer [199]. Achieving a compact integrated heater with low thermal crosstalk is still a challenge which continues to attract research interest.

### 5.1.1 Integrated Titanium heater with strip and rib waveguides

The geometry of the rib and strip waveguides together with the integrated heaters are simulated with Lumerical [122], and depicted in Fig. 5.1 (a, b) [105]. Silicon dioxide ($SiO_2$) is used as the material for the buried oxide (BOX) as well as for the cladding layers. Standard SOI dimensions are implemented along the x and y-axes, respectively considering the wavelength $\lambda = 1550\,$nm. The Titanium (Ti) heater is $5\,\mu$m wide and $0.1\,\mu$m thick and is placed on top of the primary waveguide (wg-p). The phase crosstalk is quantitatively defined as the ratio between the phase shift experienced by the secondary waveguide (wg-s) to the phase shift of the primary waveguide (wg-p). The temperature distribution profiles and the variation of phase with respect to the power as depicted in Fig. 5.1 (c, d) and Fig. 5.2 (a) are simulated with the HEAT and MODE solvers of Lumerical [122] which provides a rigorous numerical assessment of both thermal distribution profile and optical mode propagation, respectively.



https://doi.org/10.7795/110.20260421B

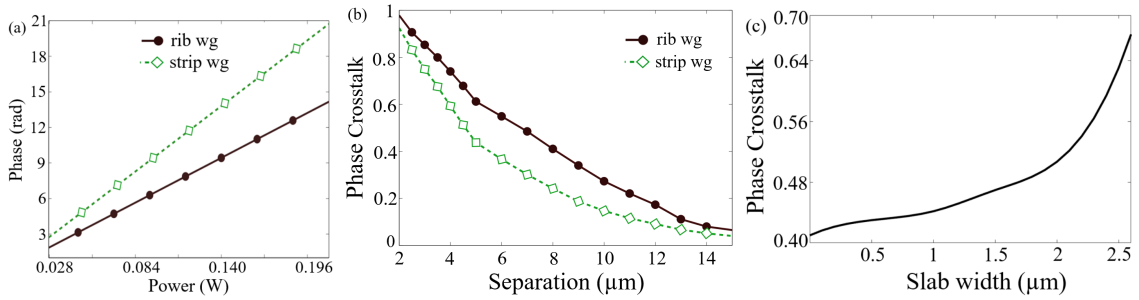


**Figure 5.2:** (a) Phase response with respect to the power applied across the Ti heater in the primary waveguide (wg-p) for rib and strip waveguides with a Ti heater. (b) Comparison of phase crosstalk at the secondary waveguide (wg-s) for strip and rib waveguides. (c) Phase crosstalk analysis by changing the slab widths based on [105]. For this scenario, a power of 211 mW is applied across the heater. The length of the waveguide is taken as 300 $\mu$m for every scenario.

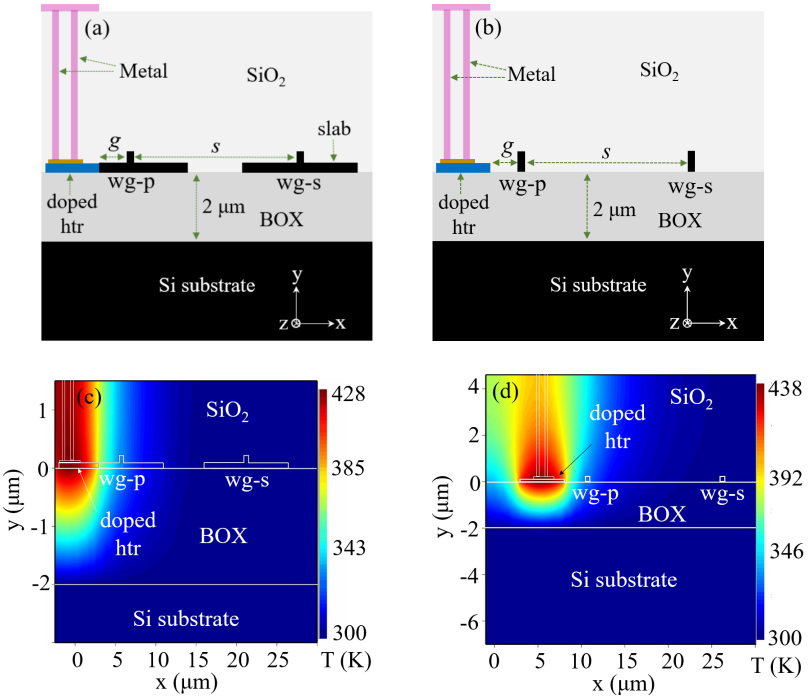


**Figure 5.3:** Structures of (a) rib and (b) strip waveguides with an $N^{++}$ doped silicon heater, where wg-p and wg-s denote the primary and secondary waveguides for crosstalk evaluation. Temperature distributions for $s = 15\,\mu$m and 211 mW heater power are shown in (c) and (d) for rib and strip waveguides, respectively, based on [105]. The axes use different scales, with dimensions in $\mu$m. The color scale represents temperature (K), from 300 K (blue) to 428 K in (c) and 438 K in (d).

The HEAT solver provides accurate modeling with the finite-element method and the MODE solver uses the finite-difference eigenmode (FDE) method to find out the optical modes and effective indices. To estimate the dependence of the phase crosstalk on the inter-waveguide spacing as shown in Fig. 5.2 (b), the center-to-center separation between the waveguides was shifted from 2 $\mu$m to 15 $\mu$m.

The illustrated temperature distribution profiles affirm the diffusion of heat from the heater into both the primary (wg-p) and the secondary waveguides (wg-s) which alters the local refractive index via the thermo-optic coefficient of the material, and hence modifies the phase of the signal in both waveguides (wg-p and wg-s). While the shift in the phase is intentional



https://doi.org/10.7795/110.20260421B

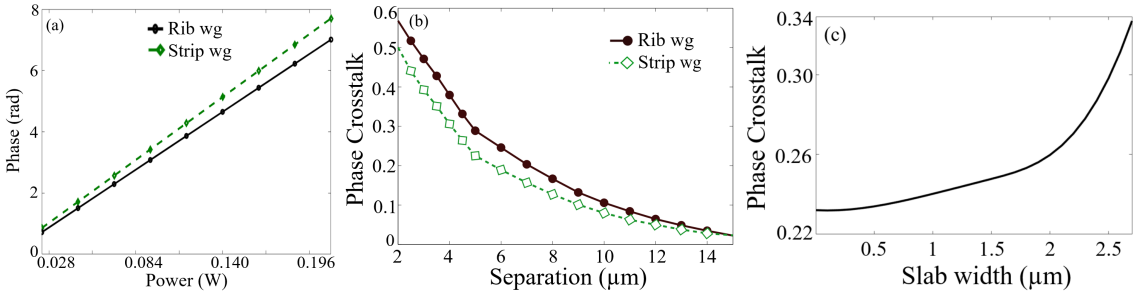


**Figure 5.4:** (a) Phase response with respect to the power applied across the $N^{++}$ doped silicon heater in the primary waveguide (wg-p) for rib and strip waveguides with a Ti heater. (b) Comparison of phase crosstalk at the secondary waveguide (wg-s) for strip and rib waveguides. (c) Phase crosstalk analysis by changing the slab widths based on [105]. For this scenario, a power of 211 mW is applied across the heater. The length of the waveguide is taken as 300 $\mu$m for every scenario.

in the primary waveguide (wg-p), it ensues in undesired thermal crosstalk in wg-s (secondary waveguide). As per Fig. 5.2 (a), for ensuring a phase shift of $\pi$, the rib waveguide structure demands for 0.042 W of power, while the strip waveguide needs 0.029 W to get the same response. Thus, the strip waveguides are more sensitive to fluctuations in temperature and hence more efficient in terms of power usage. For the strip waveguide designs, the silicon slabs which spreads the heat laterally, are not present thus ensuring in higher efficiency. As a consequence of the relatively high thermal conductivity of silicon (55 W/m·K) as compared to that of $SiO_2$ (1.38 W/m·K) [182], the thermal isolation is compromised with slabs. Hence, curtailing the slab width, as is implemented in the strip waveguide configuration, enhances the thermal isolation as depicted in Fig. 5.2 (c).

### 5.1.2 Integrated doped Silicon heater with strip and rib waveguides

As compared to the metal heaters, the doped silicon heaters showcase a better performance in terms of the thermal isolation and lowered phase crosstalk [96, 105]. For the simulations, an $N^{++}$ doped Si heater with a doping concentration of $1 \times 10^{20}$ cm$^{-3}$ is used. This heater is aligned in-plane with the primary and secondary waveguides while being 5 $\mu$m wide and 0.09 $\mu$m thick, which are usual design parameters [182]. In order to suppress the optical loss from free-carrier absorption, the heater is placed at a gap $g$ of 2.5 $\mu$m from the primary waveguide (wg-p). The simulation settings, including the parameters for the rib and strip waveguides and solver configurations are adapted according to Section 5.1.1. The geometry of the $N^{++}$ doped Si heater with the rib and strip waveguides and the respective temperature distribution profiles are depicted in Fig. 5.3. The center-to-center separation between the waveguides was shifted from 2 $\mu$m to 15 $\mu$m to evaluate the phase crosstalk for rib and strip waveguide configurations. As with metal heaters, for attaining a $\pi$ phase shift, the rib waveguides need a power of 0.091 W while the strip waveguides need only 0.080 W of power as illustrated in Fig. 5.4 (a). Subsequently, the strip waveguide configuration results in a mildly lower phase crosstalk as per Fig. 5.4 (b). The effect of slab width in rib waveguides for phase crosstalk was evaluated for $N^{++}$ doped Si heaters as shown in Fig. 5.4 (c) and it was ascertained that an increased slab width leads to deteriorated crosstalk performance. This occurs primarily be-



https://doi.org/10.7795/110.20260421B

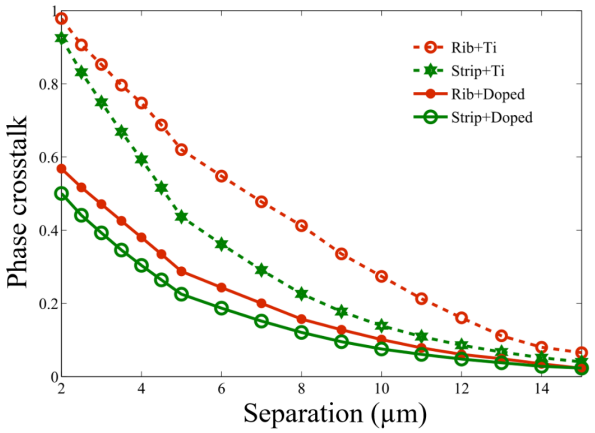


**Figure 5.5:** Phase crosstalk at the secondary waveguide (wg-s) for rib and strip waveguides considering both the Ti heater and the $N^{++}$ doped silicon heater. For every scenario, a power of 211 mW is applied across the heater and the length of the waveguide is taken as 300 $\mu$m based on [105].

cause of silicon incorporating a larger thermal conductivity then the encircling $SiO_2$ cladding. Consequently, the secondary waveguide (wg-s) receives more heat and becomes more prone to thermal crosstalk from nearby heater elements.

### 5.1.3 Performance analysis

A comparative evaluation of the phase crosstalk for Ti heaters and $N^{++}$ doped Si heater is exhibited in Fig. 5.5 demonstrating that the strip waveguides provide improved thermal isolation and superior power efficiency than the rib waveguides [105]. Nevertheless, this advantage is offset by a larger insertion loss of around 3 dB/cm [203]. For $N^{++}$ doped Si heater, both rib and strip waveguide structures exhibit a notably lower phase crosstalk than the metallic counterparts. This refinement can be credited to the localized heating for the doped heaters as compared to the metal heaters, which heats up a broader region encompassing the neighboring structures. Subsequently, the doped heaters are more suited for applications limited by thermal crosstalk, given that the corresponding power consumption is well within the tolerable limits.

### 5.1.4 Metal vias, routing, and heater power consumption

In standard PICs, the metal contacts or vias are used for delivering electrical power to drive the heating elements. For the simulations, the ambient temperature is kept at 300 K and a convection of 10 $W/m^2 \cdot K$ is assumed between the oxide cladding and the ambient air. The structural comparison of doped heaters for with and without Aluminum (Al) contacts is depicted in Fig. 5.6 (a) and (b) respectively. Most of the applied electrical power is dissipated as heat within the doped heater and at the contact resistances. With the supply of electrical power, the doped heater acts as the heat-generating element and the heat produced diffuses into the adjacent waveguides, the cladding, and the neighboring components. As illustrated in Fig. 5.6 (c), a $N^{++}$ doped Si heater without metal contacts can realize a temperature of 428 K at 150 mW of applied electrical power. But when the metal contacts are introduced,



https://doi.org/10.7795/110.20260421B

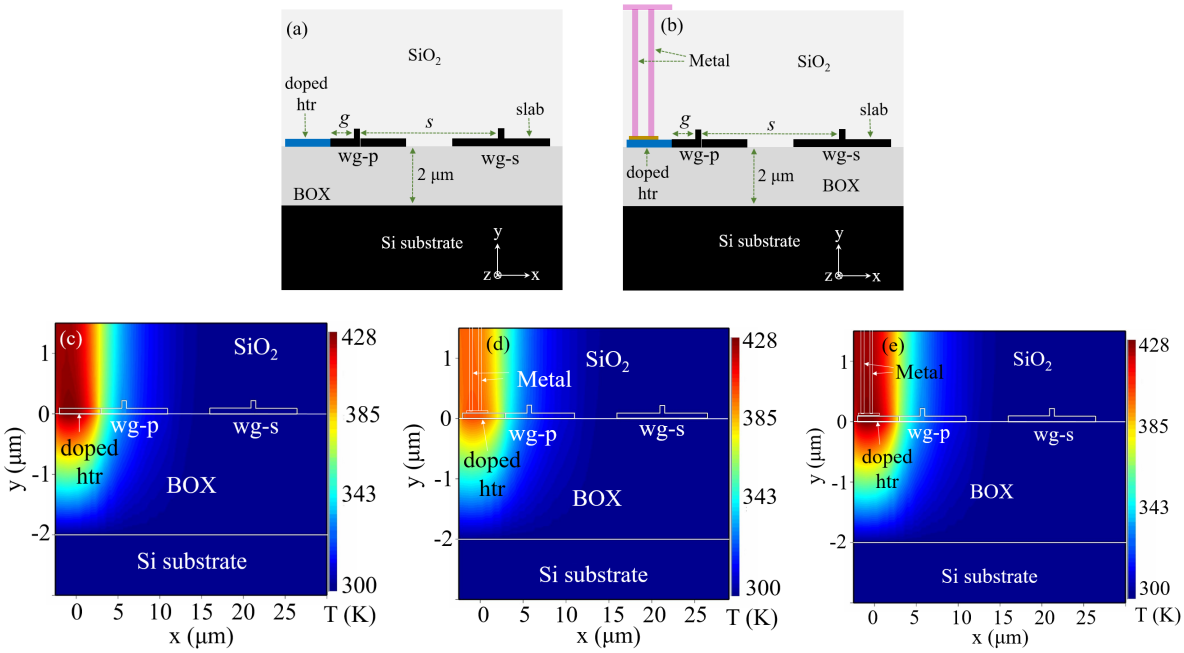


**Figure 5.6:** Rib waveguide configuration with $N^{++}$ doped silicon heaters: (a) without metal contacts and (b) with aluminum (Al) vias and a contact pad. Temperature profiles at 150 mW are shown in (c) and (d) for the respective cases, while (e) shows the temperature distribution with metal interfacing at 211 mW, based on [105]. The color scale in (c), (d), (e) represents temperature in Kelvin (K), ranging from 300 K (blue) to 428 K (red).

the doped heater can realize a temperature of 401 K, only, for the same power input [105] as shown in Fig. 5.6 (d). This can be attributed to the resistance and heat dissipation in the metal contacts and the vias which act as both resistive elements and thermal sinks. To achieve a temperature of 428 K with metal contacts at the doped heater, an input power of 211 mW is necessary as per Fig. 5.6 (e) [105]. Thus, the presence of metal contacts corresponds to an electrical power increase by around 40 % to attain the same thermal performance as is obtained in the absence of metal heaters. This increase in power requirement is applicable for metal heater structures as well. Nonetheless, the power loss can be minimized by strategic designs [200].

To evaluate the thermal leverage of metal routings on the top layer, thorough simulations were performed to assess the power dissipation in electrical routíngs and wire bondings on a standard SOI platform [105]. The $N^{++}$ doped Si heater was modeled with the respective dimensions and is located nearby a silicon waveguide with a thickness of 0.22 $\mu$m. The top metal routing is represented by the aluminum (Al) layer which is placed above the waveguide. To separate the silicon substrate from the waveguide a buried oxide layer (BOX) is used. The geometrical parameters for the design follow the standard SOI platform as per Section 5.1.2. The cross-sectional layout of the doped heater design with Al routing on top is depicted in Fig. 5.7 (a). Although many of the SOI foundries provide multi-layer stacks for complex photonic circuits, the model discussed here provides a simplification of the stack including only the top metal, waveguide, and the silicon substrate.

For the preliminary step, all resistances including those across the interconnects, gold bond



https://doi.org/10.7795/110.20260421B

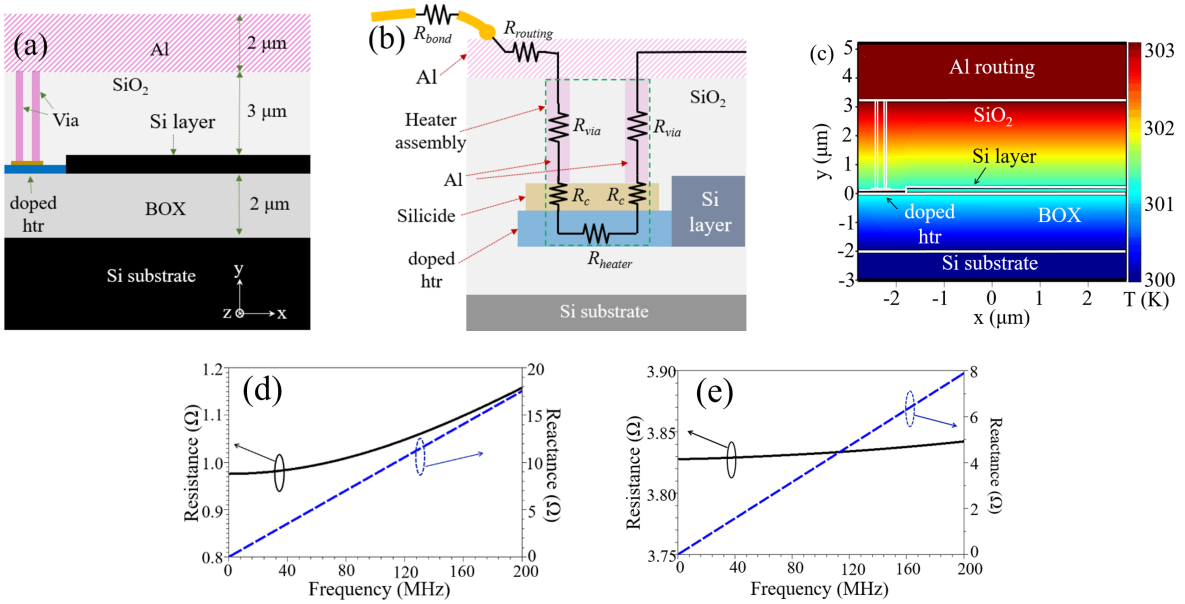


**Figure 5.7:** (a) Structure of the $N^{++}$ doped silicon heater featuring top layer aluminum (Al) routing. (b) Equivalent electrical resistance modeling of the $N^{++}$ doped silicon heater incorporating Al interconnects and gold wire bonds for PCB wire bonding. (c) Heat distribution profile generated by 5 mW power dissipation at the Al routing. The color scale in represents temperature in Kelvin (K), ranging from 300 K (blue) to 303 K (red). Plots of (d) resistance and (e) reactance versus frequency for the Al electrical routing and the gold wire bond, respectively based on [105].

wire, and heater structures, were retrieved to gauge the heat discharge across the top layer interconnects and the printed circuit board (PCB) wire bonding. The electrical model which is depicted in Fig. 5.7 (b) takes into account only the resistive losses excluding contributions that are capacitative ($C$) or inductive ($L$) considering low-frequency operation. For evaluating the worst-case scenario, An Al interconnect of length 5 mm corresponding to the typical maximum interconnect length in a PIC, and a gold wire bonding of 10 mm length and 20 $\mu$m diameter used for PCB packaging were considered. In practical scenarios, the usual PIC interconnects have much lower undesired resistance and inductance [204] and smaller bond wires [205] resulting in better performance.

The resistances of the electrical routing ($R_{\text{routing}}$) and the gold bond wire ($R_{\text{bond}}$) are determined with simulations using the Advanced System design (ADS) software [206] as per Fig. 5.7 (d, e). The $R_{\text{routing}}$ and $R_{\text{bond}}$ are taken to be 4 $\Omega$ and 1 $\Omega$, respectively, considering the operation of the TOPS electrical excitation at low frequencies in the kHz range. Full-wave electromagnetic simulations were using the Finite Element Method (FEM) solver of ADS to evaluate the overall resistance $R_{\text{T}}$ of the doped heater assembly. The different components like metal vias, doped silicon heater, buried oxide, and silicon substrate were considered in the 3D SOI model with every layer having its own parameters including conductivity, permittivity, etc. A frequency sweep was performed at frequencies ranging from 1 kHz to 200 MHz to evaluate the impedance response after applying differential ports at the metal pads. Eventually, the real part of the impedance at lower frequency provided the information for the effective DC resistance. The overall resistance $R_{\text{T}}$ of the doped heater assembly is formulated



https://doi.org/10.7795/110.20260421B

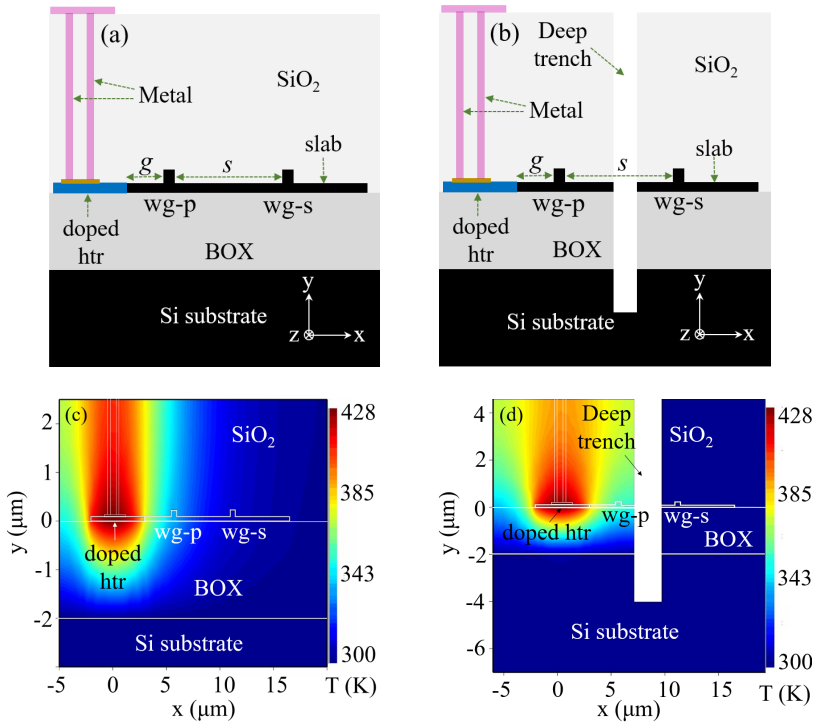


**Figure 5.8:** Structure of the rib waveguide having a $N^{++}$ doped silicon heater with wg-p as the primary waveguide and wg-s as the secondary waveguide for (a) no trench and (b) deep trench configuration. Heat distribution profiles are depicted for (c) no trench and (d) deep trench configuration considering a waveguide separation of $s = 5\,\mu$m and a heater power of 211 mW based on [105]. The color scale in (c) and (d) represents temperature in Kelvin (K), ranging from 300 K (blue) to 428 K (red).

as: $R_T = 2(R_{\text{via}} + R_C) + R_{\text{heater}}$, where $R_{\text{via}}$ represents the via resistance, $R_C$ denotes the contact resistance from the silicide region at the junction of the metal via and the doped heater, and $R_{\text{heater}}$ indicates the resistance of the doped heater. Given that $R_{\text{via}} \ll R_C$ or $R_{\text{heater}}$, the total resistance has been calculated roughly to be $R_T \approx 2R_C + R_{\text{heater}}$ and the total resistance $R_T$ of the heater assembly is 930 Ω. In practical designs, the $R_T$ can change up to an order of magnitude depending upon the process variations in doping, heater geometry, etc. [202]. As per the resistance values evaluated from Fig. 5.7 (b), the electrical routing expends a total power of 5 mW when the doped heater assembly is operating at 211 mW. This indicates that around 2 % of the total power is lost in the top layer electrical routing, which is relatively small but important nonetheless for thermal management and overall efficiency.

To evaluate the thermal impact of the Al routing on the adjacent silicon waveguides, a power of 5 mW was applied to the Al layer, accounting for the worst-case scenario. The resulting temperature distribution profile is illustrated in Fig. 5.7 (c), indicating that the Al interconnect reaches a temperature of 303 K, whereas the Si layer experiences a temperature or around 301.5 K which is 1.5 K above the ambient temperature. Hence, the electrical routings and wire bondings have a marginal contribution to thermal crosstalk in the whole system. Nevertheless, the inclusion of multi-level metal interconnects in future designs might enable a modest temperature increase, potentially necessitating additional thermal management considerations.



https://doi.org/10.7795/110.20260421B

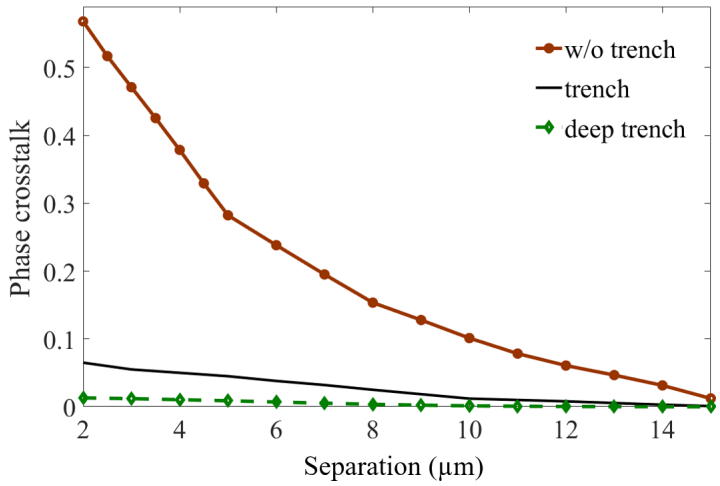


**Figure 5.9:** Phase crosstalk evaluation for $N^{++}$ doped silicon heater configuration with rib waveguides working at a power of 211 mW for no trench, oxide trench [96], and deep trench scenarios depicted in brown, black, and green. respectively based on [105].

## 5.2 Thermal crosstalk mitigation techniques

To allow for high bandwidth signal processing with high performance in dense PICs, it is essential to mitigate the thermal crosstalk in such designs. A brief overview of the thermal crosstalk alleviation methods has been given in Section 2.6.2. Using integrated doped heaters which are CMOS compatible, it is possible to lower the crosstalk up to a certain extent as shown in the previous section. Previously, we have demonstrated the air-filled oxide trench designs [96, 175] to suppress the crosstalk to a large extent. To ensure further minimization of thermal crosstalk, two design techniques, namely, deep trench isolation technique [105] and amorphous silicon (a-Si) [193] are discussed in this thesis.

### 5.2.1 Deep trench design

Introducing an air-filled deep trench between the rib waveguides, as illustrated in Fig. 5.8 (b) can improve the crosstalk alleviation [105]. This CMOS compatible trench begins at 2 $\mu$m below the surface of the silicon substrate and extends vertically to the top layer with a lateral distance of 2 $\mu$m from the primary waveguide (wg-p). As the trench is filled with air that possesses a minimal thermal conductivity of 0.026 W/m·K, it serves as an effective thermal insulator which suppresses the heat diffusion from the primary waveguide (wg-p) into the secondary waveguide (wg-s). A comparison of the doped heater geometry for no trench and deep trench scenarios together with the respective temperature distribution profiles is given in Fig. 5.8, illustrating that the secondary waveguide (wg-2) maintains a near-ambient temperature of 300 K with a deep trench regardless of the power applied across the doped heater. As depicted in Fig. 5.9, it can be ascertained that the deep trench results in minimal phase crosstalk over a wide range of separation $s$ between the two rib waveguides (wg-p and wg-s). Additionally, the deep trench offers thermal isolation which confines the heat effectively within the primary waveguide (wg-p), enabling the desired phase shift with low electrical



https://doi.org/10.7795/110.20260421B

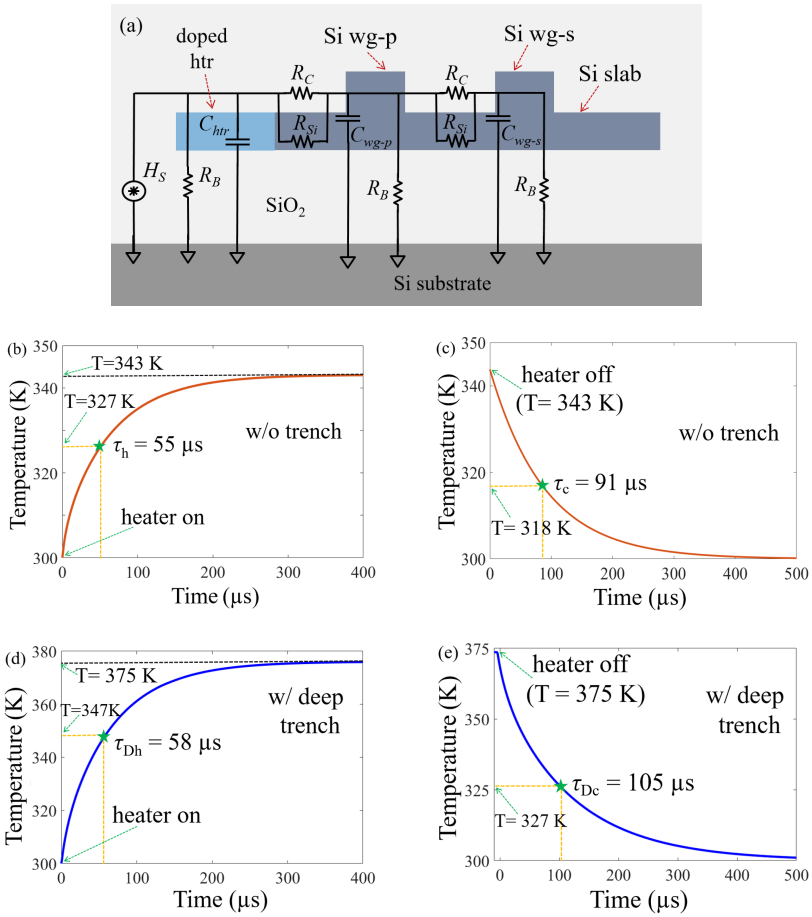


**Figure 5.10:** (a) Basic thermal RC model of the $N^{++}$ doped silicon heater configuration with rib waveguides using the parameters listed in Table 5.1. Transient analysis depicting temperature as a function of time with the doped heater and the primary waveguide (wg-p) showing the heating time constant ($\tau_h$) and the cooling time constant ($\tau_c$) for no trench (a, b) and deep trench (c,d) configurations respectively. In every scenario, a step input of 211 mW is given at the $N^{++}$ doped silicon heater based on [105].

power.

While deep trenches boost the thermal isolation, they can potentially alter the thermal time constant and the switching speed of the system. To quantify this, a detailed thermal transient analysis is conducted with a thermal RC network model as depicted in Fig. 5.10 (a) including the doped heater, silicon slab, and the two waveguides (wg-p and wg-s). This analysis is performed with the HEAT solver in Lumerical [122]. Here, the silicon substrate acts as the thermal equivalent of an electrical ground, enabling the primary path for heat removal. The parameters $R$ and $C$ indicate the thermal resistance and heat-storing capacity, respectively, of the corresponding component. The doped heater is activated with an external electrical power $H_S$ and the resulting heat mainly goes into the primary waveguide (wg-p) through the silicon slab $R_{Si}$ and the cladding region indicated as $R_B$ or $R_C$. The majority of the heat flux goes through the silicon slab as silicon has a substantially higher thermal conductivity as opposed to silicon dioxide ($SiO_2$), thus establishing it the main channel for thermal conduction. According to the thermal RC model, approximate expressions for the heating ($\tau_h$) and cooling ($\tau_c$) time constants can be extracted in terms of thermal resistance and capacitance. For no



https://doi.org/10.7795/110.20260421B

| Substance | Depth [µm] | Density [kg/m$^3$] | Heat capacity [J/kg·K] | Thermal conductivity [W/m·K] | Electrical conductivity [S/m] |
|---|---|---|---|---|---|
| Si (substrate) | $\gg 10$ | 2330 | 711 | 148 | $4.3 \times 10^{-4}$ |
| Si (wg) | 0.22 | 2330 | 711 | 90 | $4.3 \times 10^{-4}$ |
| Si (slab) | 0.09 | 2330 | 711 | 55 | $4.3 \times 10^{-4}$ |
| $N^{++}$ doped Si | 0.09 | 2330 | 711 | 25 | $1.0 \times 10^{5}$ |
| $SiO_2$ | – | 2203 | 709 | 1.38 | $1 \times 10^{-11}$ |
| Air | $\gg 10$ | 1.177 | 1006 | 0.026 | $1 \times 10^{-12}$ |

**Table 5.1:** Material parameters used for thermal simulations based on [182].

trench the expressions are given as: $\tau_h \approx R_{Si} C_{wg\text{-}p}$; $\tau_c \approx 0.45 R_B C_{wg\text{-}p}$ where $R_{Si}$ and $R_B$ denote the thermal resistance of the silicon and the clad layer, respectively. The parameter $C_{wg\text{-}p}$ indicates the heat-storing capacitance of the primary waveguide (wg-p). As $R_{Si} < R_B$, the cooling time constant is greater than the heating time constant implying that the cooling process will take longer than the heating. Consequently, the electrical driving frequency $f$ of the doped heater is constrained by the slower cooling time constant $\tau_c$. The corresponding time constants for the deep trench design as evaluated as: $\tau_{Dh} \approx R_{Si} C_{wg\text{-}p}$; $\tau_{Dc} \approx 0.5 R_B C_{wg\text{-}p}$. As $R_{Si} < R_B$, even with deep trench designs, the cooling time constant $\tau_{Dc}$ remains higher than the heating time constant $\tau_{Dh}$. As a consequence, the input frequency $f$ of the doped heater is limited by the cooling time constant $\tau_{Dc}$ . While the heating time-constant is approximately the same with and without the deep trench ($\tau_{Dh} \approx \tau_h$), the cooling process is marginally extended with the deep trench. This happens due to the poor thermal conductivity of air as opposed to silicon dioxide ($SiO_2$), ensuing in a marginal reduction in the allowed modulation frequency.

The thermal response at the primary waveguide (wg-p) was evaluated after applying a step electrical input power at the doped heater presenting heating time constants of $\tau_h = 55\,\mu s$ and $\tau_{Dh} = 58\,\mu s$ for no trench and deep trench designs, as illustrated in Fig. 5.10 (b) and (d), respectively. To estimate the cooling behavior, the input power was sustained for $400\,\mu s$ for ensuring steady-state conditions, followed by a sudden shutdown. As depicted in Fig. 5.10 (c) and (e) the cooling time for the deep trench ($\tau_{Dc} = 105\,\mu s$) is higher than that of no trench ($\tau_c = 91\,\mu s$) confirming that the cooling persistently slower than the heating which is consistent with the theory. The 3 dB input frequency was estimated to be around 11 kHz and 9.5 kHz for no trench and deep trench designs suggesting a reduced switching speed for the deep trench. Nonetheless, the heating efficiency at the primary waveguide (wg-p) and thermal crosstalk at the secondary waveguide (wg-s) are noticeably improved due to heat localization at the primary waveguide (wg-p) for the deep trench design.



https://doi.org/10.7795/110.20260421B

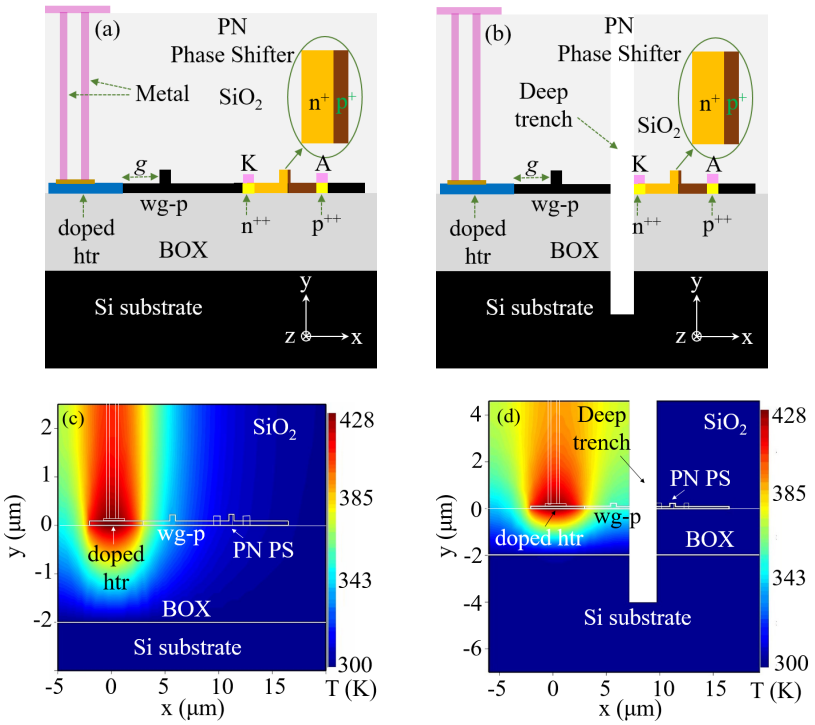


**Figure 5.11:** The cross-section profile of a thermally tuned primary waveguide (wg-p) and a PN phase shifter (PN PS) considering (a) no trench and (b) deep trench configurations. Heat distribution profiles for wg-p and PN phase shifter separation of 5 $\mu$m and heater power of 211 mW are depicted for (c) without trench and (d) deep trench configuration based on [105]. The color scale in (c) and (d) represents temperature in Kelvin (K), ranging from 300 K (blue) to 428 K (red).

### Crosstalk evaluation in PIC designs

A comprehensive evaluation of thermal crosstalk for the deep trench design is carried out for a multitude of photonic devices typically used in PICs like modulators, switches, photodetectors, etc. in the following sub-section. These findings are essential for ensuring scalable and compact PICs, where alleviating thermal crosstalk is of critical importance.

### A. Integrated PN junction phase shifter

The CMOS compatible integrated PN phase shifters [207, 208] are used in silicon photonics for a multitude of applications like tunable filters, wavelength-selective switches, photonic neural networks, etc . The thermal crosstalk performance of a deep trench based PN phase shifter is evaluated with the geometry for no trench and deep trench depicted in Fig. 5.11 (a) and (b), respectively [105]. In the modified design (Fig. 5.11 (b)), the thermally tuned waveguide and the PN phase shifter are spaced by 5 $\mu$m and a reverse bias voltage was used across the Anode (A) and Cathode (K) of the Al electrodes for biasing the phase shifter. In the phase shifter, the $n^{++}$ and $p^{++}$ regions are having a doping concentration of $1 \times 10^{20}$ cm$^{-3}$ and the $p^{+}$ and $n^{+}$ wells are doped with a concentration of $2 \times 10^{17}$ cm$^{-3}$ and $4 \times 10^{17}$ cm$^{-3}$, respectively. From the temperature distribution profiles in Fig. 5.11 (c) and (d), it can be observed that the deep trench substantially lessens the heat transfer to the PN region, hence alleviating the thermal crosstalk. Consequently, for the deep trench design, the phase is unaffected by the



https://doi.org/10.7795/110.20260421B

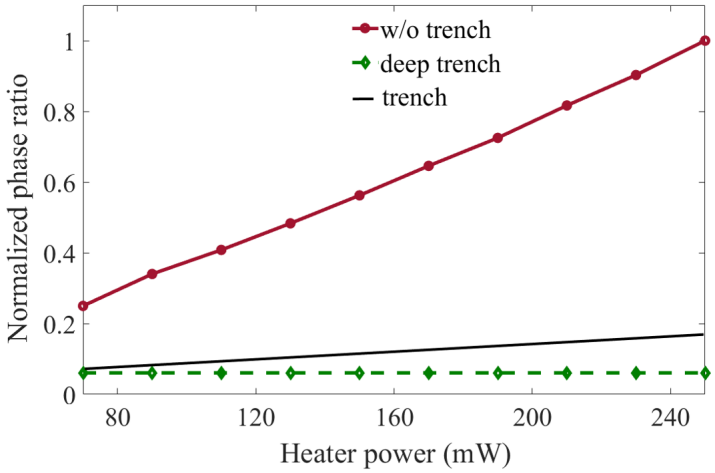


**Figure 5.12:** The normalized phase ratio comparison for no trench, oxide trench [96], and deep trench scenarios. Here, the normalized phase ratio is evaluated by dividing the phase shift in the PN phase shifter by the phase shift in the main waveguide (wg-p) at the highest heater power based on [105].

reverse bias voltage independent of the power given across the neighboring doped heater as per Fig. 5.12. Thus, the modified configuration with deep trench ensures a more robust thermal shielding mechanism, elevating the reliability and scalability of PICs.

### B. MZM driven with a PIN diode

The thermal crosstalk behavior of a MZM based on a PIN diode structure [209, 210] is examined for no trench and deep trench isolation as is illustrated by the geometries in Fig. 5.13 (b) and (c), respectively [105]. The top view of one arm of the modulator is demonstrated in Fig. 5.13 (a) and it depicts the modulator geometries in Fig. 5.13 (b) and (c). The MZM arm and the primary waveguide (wg-p) are spaced by 5 $\mu$m and for analyzing the crosstalk, a forward bias voltage ranging from 0.5 to 1.2 V is applied across the anode (A) and cathode (K) contacts of the PIN junction. In the PIN diode, the doping concentration for the $n^{++}$ and $p^{++}$ regions is $5 \times 10^{20}$ cm$^{-3}$ and they provide the forward bias voltage $V$. The $n^{+}$ type and $p^{+}$ type dopants on either side of the intrinsic (i) region have a doping concentration of $2 \times 10^{18}$ cm$^{-3}$ on either side of the intrinsic (i) region that constitutes the silicon waveguide core. The thermal and optical simulations were conducted with the CHARGE, HEAT and MODE solvers of Lumerical [122]. For the PIN junction, the diffusion of the charge carriers and the charge profile is simulated with the CHARGE solver, the temperature profile is evaluated with the HEAT solver, and the MODE solver can evaluate the resulting changes in the refractive index and the transmission characteristics.

For the MZMs, the charge is pumped from the p and n doped regions into the intrinsic (i) waveguide resulting in the modulation of the refractive index. As illustrated in Fig. 5.13 (d) and (e), with a deep trench the thermal stress on the MZM is noticeably reduced. In conventional designs, elevated heater temperatures ensue in thermal crosstalk, which amplifies the charge diffusion into the intrinsic region for a defined bias voltage $V$ eventually deteriorating the modulator performance. Within a PIN diode, the diffusion of the charge carriers is heavily



https://doi.org/10.7795/110.20260421B

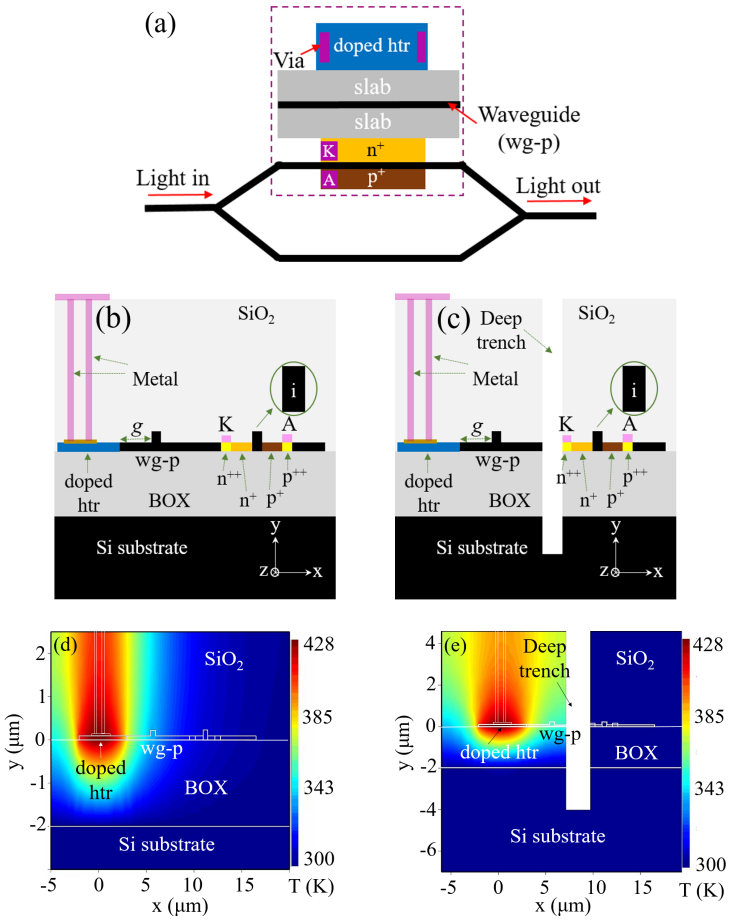


**Figure 5.13:** (a) Top view of the primary waveguide (wg-p) and Mach–Zehnder modulator (MZM). Cross-sections of the PIN diode and thermally tuned waveguide for (b) no trench and (c) deep trench cases. Heat distributions at 211 mW are shown in (d) and (e) for the respective configurations, based on [105]. The color scale in (d) and (e) indicates temperature (K), from 300 K (blue) to 428 K (red).

impacted by the temperature for a defined forward bias voltage $V$ [211]. As can be seen from Fig. 5.14 (a) and (b), the deep trench configuration allows for a minimum of twofold curtailment of charge carrier accumulation within the intrinsic (i) region.

Additionally, the refractive index showcases a linear response to the applied forward bias voltage starting from around 0.75 V as demonstrated in Fig. 5.15 (a) for deep trench as opposed to the non-linear response for no trench. This is a consequence of the elevated charge carrier diffusion, both electrons and holes, from the $p^+$ and $n^+$ regions into the intrinsic waveguide core with increased temperatures. As the temperature escalates, there is a boost in the amount of carriers in the intrinsic region, resulting in a non-linear shift in the effective refractive index. With a deep trench, this effect is mitigated by thermal isolation of the waveguide, ensuring that the refractive index is modified only by the applied voltage. This is especially useful for densely packed PICs with plenty of heaters, where the non-linearity can result in noticeable signal deterioration along with undesired higher-order sidebands in the modulated signals. Furthermore, the DC transfer curve in Fig. 5.15 (b) illustrates that the MZM needs a reduced $V_\pi$ (voltage to achieve a phase shift of $pi$) for the deep trench scenario thus affirming its superior performance and minimal thermal interference.



https://doi.org/10.7795/110.20260421B

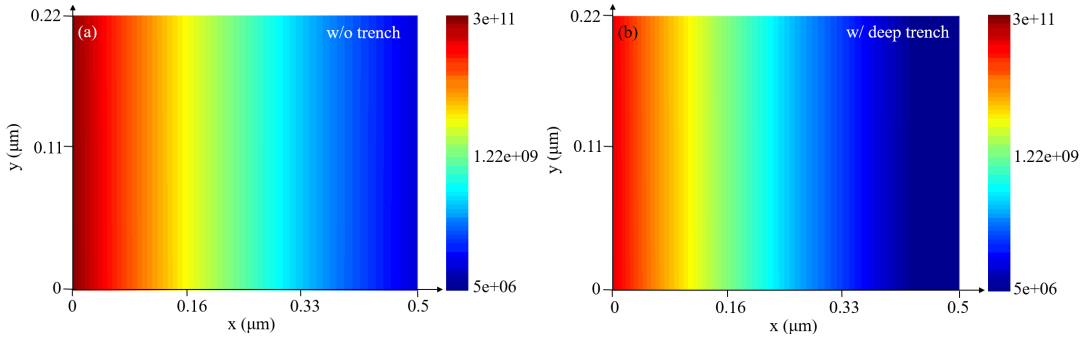


**Figure 5.14:** Charge distribution profile across the intrinsic region (i) of a PIN diode-based Mach–Zehnder modulator (MZM) for (a) no trench and (b) deep trench scenarios for a heater power of 211 mW and an applied bias voltage ($V_{\text{bias}}$) of 0 V based on [105]. The color scale represents the charge concentration in $\text{cm}^{-3}$ on a logarithmic scale, ranging from $5 \times 10^6$ (blue) to $3 \times 10^{11}$ (red).

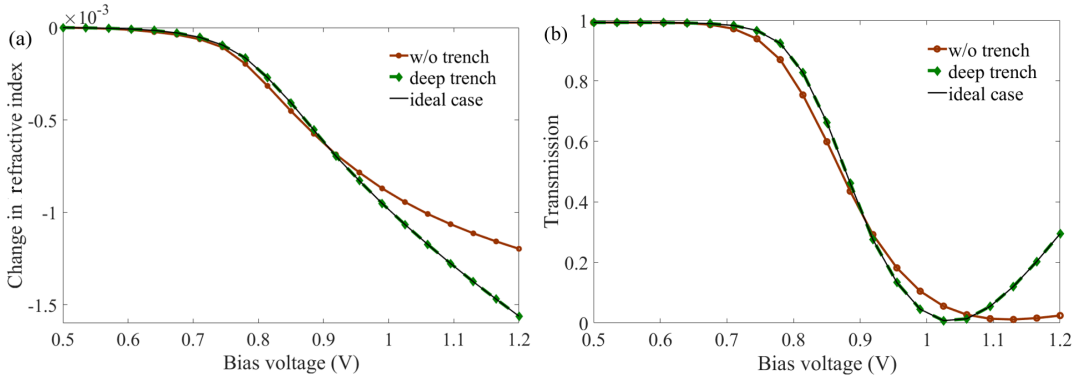


**Figure 5.15:** The variation of (a) the refractive index and (b) the optical transmission with respect to the bias voltage (V) for the no trench and deep trench configurations considering power of 211 mW applied across the $N^{++}$ doped silicon heater based on [105].

### C. Travelling Wave MZM

High-speed PN junction-based travelling-wave MZMs [212, 213] are key elements in silicon (Si) photonic transceivers for optical communication, ensuring high-speed and efficient modulation by harnessing a longer electrical–optical interaction region ensuing in a broader bandwidth. These structures are critical in PIC designs owing to their enhanced performance as opposed to conventional MZMs.

The top view of the MZM arm is depicted in Fig. 5.16 (a), and the cross-sectional configuration together with the doped heater and the thermally tuned waveguide (wg) is illustrated for no trench and deep trench configurations in Fig. 5.16 (b) and (c), respectively [184, 185]. For simulating the worst-case thermal interaction, the heater is located in close proximity to both the MZM arm and the waveguide (wg). The dimensions for the $N^{++}$ doped Si heater, Si waveguide (wg) is same as discussed in Section 5.1.2 with the gap $g$ between the doped heater and the MZM arm as 2.5 $\mu$m to curtail the free-carrier absorption. The doping profile for the modulator includes the $n^{++}$ and $p^{++}$ regions at $1 \times 10^{20}$ $\text{cm}^{-3}$, the $n^{+}$ region at $1 \times 10^{18}$ $\text{cm}^{-3}$, and the the $p^{+}$ region at $3 \times 10^{17}$ $\text{cm}^{-3}$. As seen in the zoomed view in Fig. 5.16 (c), the active core of the MZM has $n^{+}$ and $p^{+}$ regions with widths of 100 nm and 400 nm, respectively,



https://doi.org/10.7795/110.20260421B

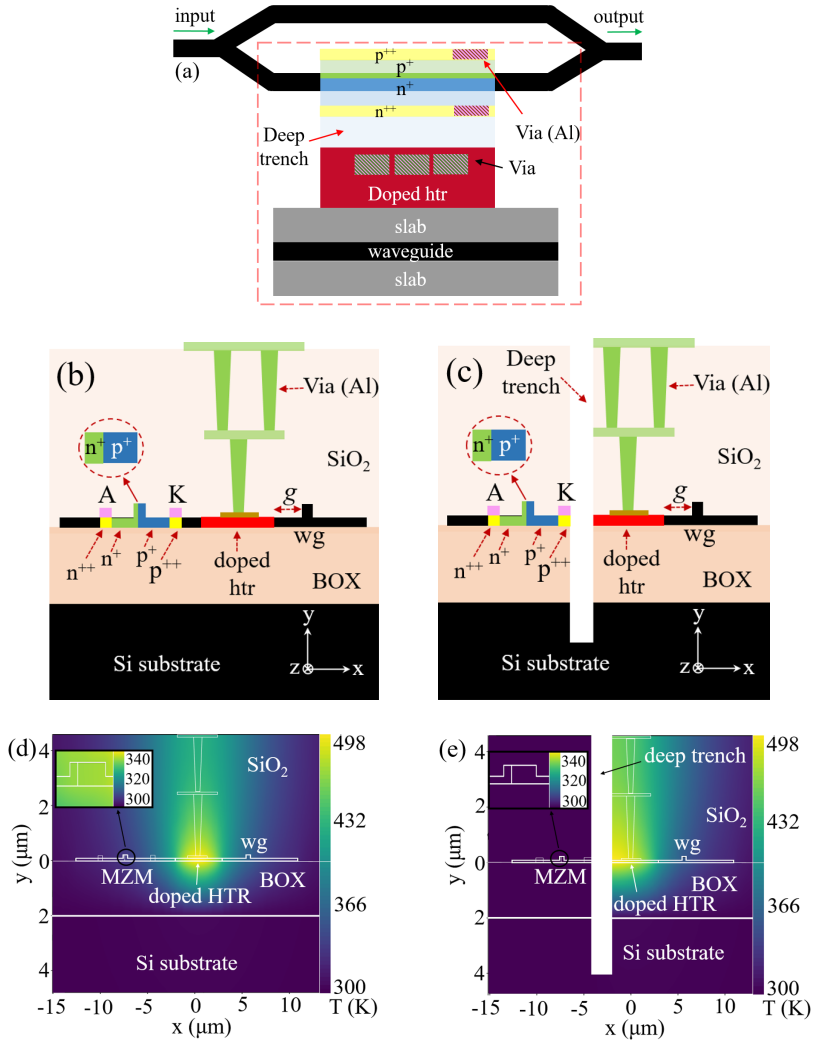


**Figure 5.16:** Cross-section profile of the TW-MZM arm and the thermally tuned waveguide (wg) for (a) no trench and (b) deep trench scenarios. Heat distribution profiles for a heater power of 250 mW are depicted for (c) no trench and (d) deep trench configuration based on [184]. The color scale in (d) and (e) represents temperature in Kelvin (K), ranging from 300 K (blue) to 498 K (yellow).

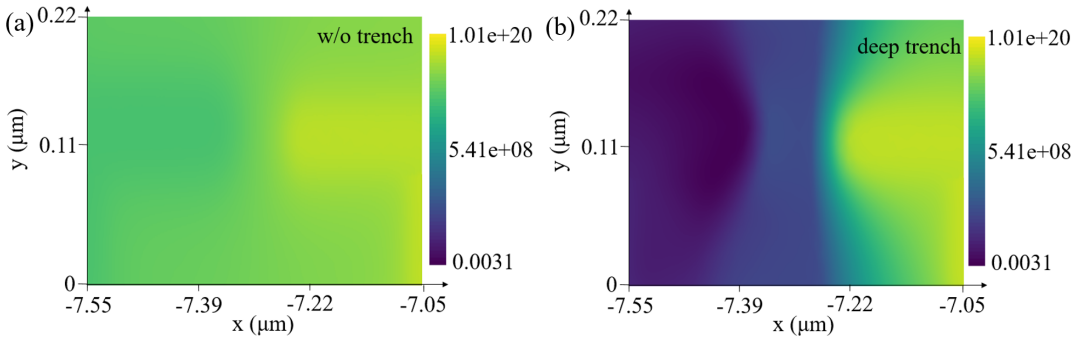


**Figure 5.17:** Charge distribution profile across the active region of the TW-MZM for (a) no trench and (b) deep trench scenarios considering a heater power of 250 mW and an applied bias voltage ($V_{\text{bias}}$) of 1.5 V based on [184]. The color scale represents the charge concentration in $\text{cm}^{-3}$ on a logarithmic scale, ranging from 0.0031 (blue) to $1.01 \times 10^{20}$ (yellow).



https://doi.org/10.7795/110.20260421B

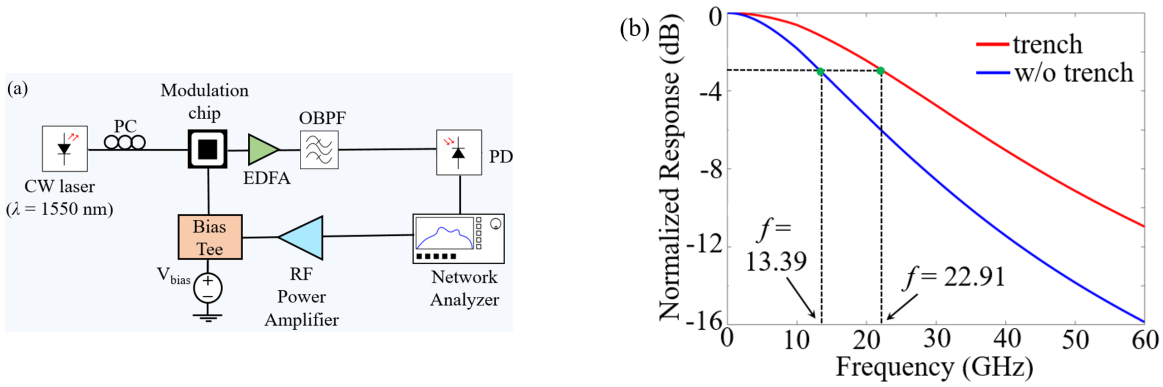


**Figure 5.18:** (a) Simulation setup for the bandwidth measurement of the TW-MZM and (b) the corresponding bandwidth for no trench and deep trench scenario based on [184]. The length of the TW-MZM is 500 $\mu$m.

with the air-filled deep trench acting as the thermal barrier. Simulations were carried out with Lumerical's [122] CHARGE, MODE and HEAT solvers indicating that the MZM core reaches a temperature greater than 340 K in the absence of trench as opposed to with the deep trench where the MZM remains at the ambient temperature of 300 K as illustrated in Fig. 5.16 (d) and (e), respectively, affirming the thermal insulation by the deep trench. Here, the CHARGE and MODE solver was used to obtain the charge distribution profile across the TW-MZM and evaluate the optical properties while the HEAT solver was used to obtain the temperature profile of the entire SOI configuration.

The charge profile distribution in the MZM core considering a reverse bias voltage ($V_{\text{bias}}$) of 1.5 V is illustrated in Fig. 5.17 (a), and it is ascertained that a temperature rise causes a considerable diffusion of $n^+$ and $p^+$ charge carriers in the MZM. Consequently, the modulator efficiency is compromised and the small-signal bandwidth is restricted. With a deep trench, this problem is resolved by thermal isolation which ensues in a lower charge carrier concentration in the active core as shown in Fig. 5.17 (b).

For simulating the electro-optic (E/O) bandwidth and BER performance of the MZM, the INTERCONNECT module of Lumerical [122] was used. The model parameters for the waveguide, optical modulator and the traveling wave electrode which constitute an entire modulator circuit is obtained from the CHARGE, MODE, and HEAT solvers and then imported into the INTERCONNECT solver for system level analysis. The simulation setup and the corresponding bandwidth performance is illustrated in Fig. 5.18 (a) and (b), respectively. With a deep trench, the bandwidth elevates to 22.91 GHz as opposed to 13.39 GHz without a trench, thus resulting in a 71 % bandwidth enhancement without any pre-compensation or pre-emphasis techniques [184]. This improvement is attributed to the trench structure suppressing the thermal diffusion of charge carriers into the active MZM core, thereby scaling down the junction capacitance and resistance which in turn lowers the RC time constant and enhances the small-signal bandwidth. The simulation setup for eye diagram and BER analysis is depicted in Fig. 5.19 (a) where the modulator performance is gauged at different data rates with an OOK modulation scheme with a $2 \times 10^{-1}$ PRBS sequence (representing a random data pattern), as visualized in Fig. 5.19 (b) - (e). For a lower data rate of 20 Gbps, the MZM has nearly identical



https://doi.org/10.7795/110.20260421B

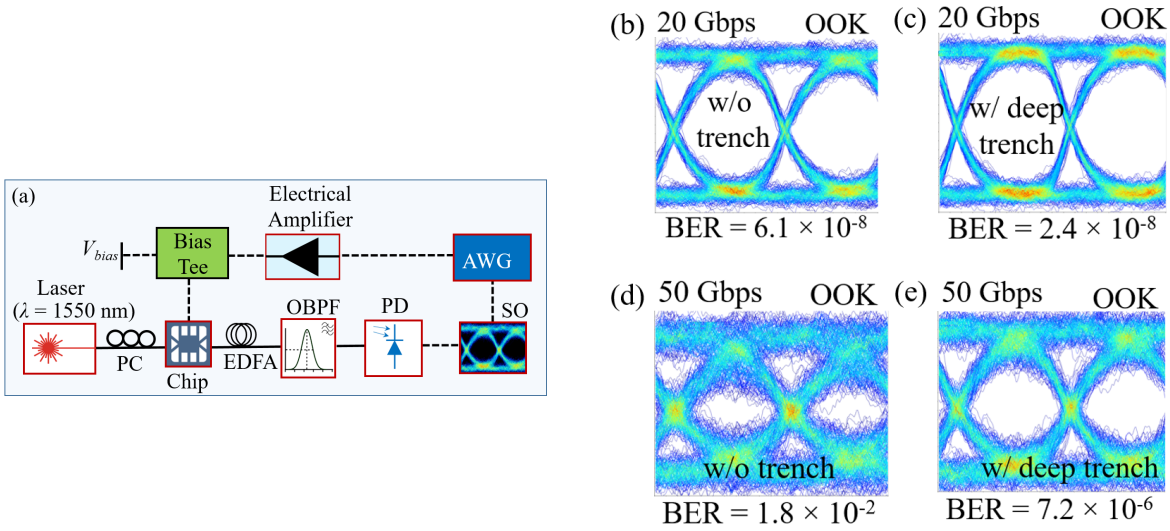


**Figure 5.19:** (a) Simulation setup for the eye-diagram and BER analysis of the TW-MZM [185]. Eye diagram analysis for no trench and deep trench scenarios at 20 Gbps (b, c) and 50 Gbps (d, e) respectively based on [184].

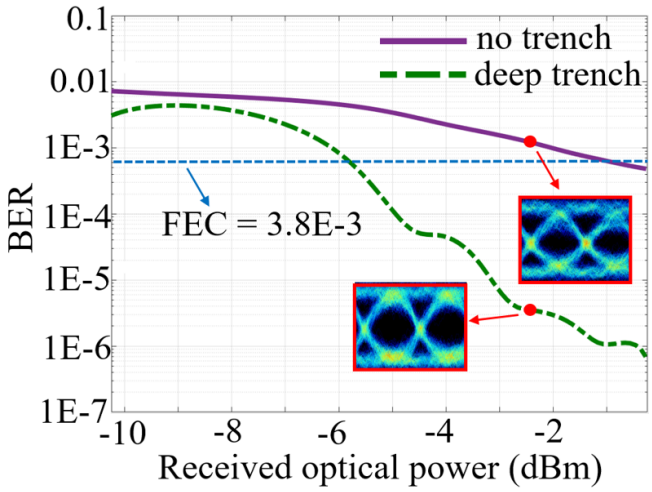


**Figure 5.20:** (a) Plot of BER with respect to the received optical power at the photodetector (PD) for no trench and deep trench scenarios at 50 Gbps based on [185].

eye diagrams with the same range for the BER. But as the data rate increases to 50 Gbps, the eye opening and the BER indicate noticeable divergence, with the deep trench model having a superior signal integrity. This is also confirmed by the plot of the BER vs the received optical power at the photodetector shown in Fig. 5.20 indicating a low BER of $3.54 \times 10^{-6}$ for the deep trench model which is much lower than the forward error correction (FEC) limits as opposed to a BER of $1.23 \times 10^{-3}$ without a trench for a received power of -2.45 dBm [185].

### D. Silicon ring modulator

The silicon ring modulators [214] in PICs provide a smaller footprint and higher energy efficiency compared to the conventional MZM designs, making them advantageous for use in frequency comb generators, digital links, microwave photonic links (MPLs), etc.



https://doi.org/10.7795/110.20260421B

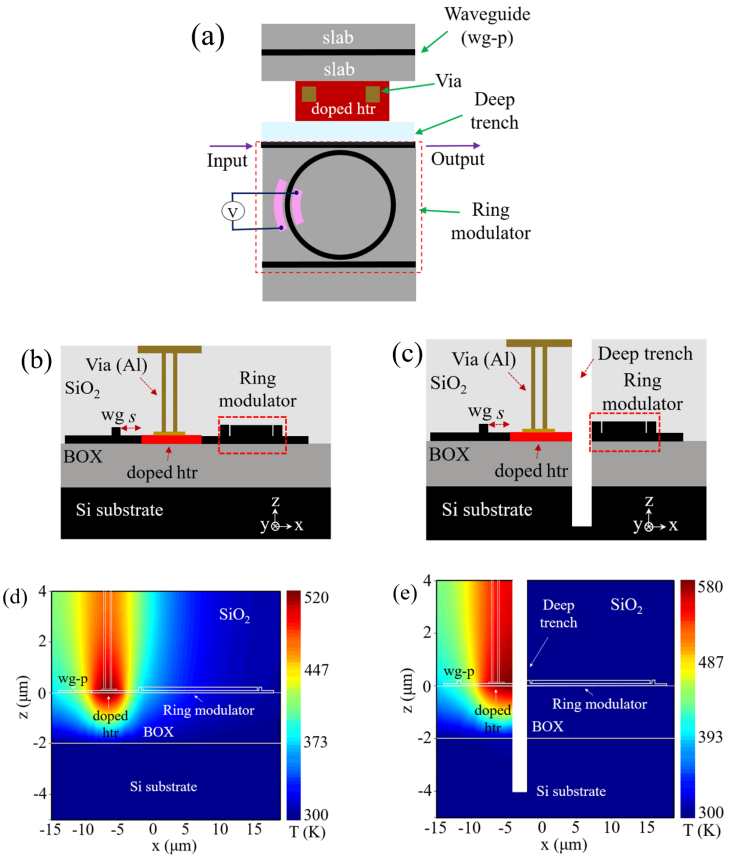


**Figure 5.21:** (a) Overhead view of the silicon (Si) ring modulator together with a doped heater, thermally tuned primary waveguide (wg-p), and deep trench structure, where the p–n junction region is marked in pink. Sectional view of the Si ring modulator, doped heater, and thermally tuned waveguide and the respective heat distribution profile for (b, d) no trench and (c, e) deep trench design based on [187]. For the temperature profiles a power of 280 mW is applied across the heater. The color scale represents temperature in Kelvin (K), ranging from 300 K (blue) to 498 K (red) in (d) and 580 K in (e).

The top view of the modulator is illustrated in Fig. 5.21 (a) and the cross-sectional layout is given in Fig. 5.21 (b), (c) for no trench and deep trench designs, respectively [187], with the 2 $\mu$m wide deep trench etched at 7.5 $\mu$m below the Si substrate. The $N^{++}$ doped Si heater and the design layouts are identical to the one in Section 5.1.2. The heater is placed in very close proximity to the modulator and at a distance of 2.5 $\mu$m from the waveguide (wg). The thermally-tuned waveguide (wg-p), the ring, and the coupling waveguide have cross-sectional proportions of 220 nm × 450 nm [215]. The ring has a radius of 7.5 $\mu$m with a distance of 210 nm from the adjacent bus waveguide. Inside the ring waveguide, the $n^+$ and $p^+$ regions are equally wide at 225 nm. The $n^{++}$, $p^{++}$, $n^+$, and $p^+$ regions are having a doping concentration of $1 \times 10^{20}$ cm$^{-3}$, $1 \times 10^{20}$ cm$^{-3}$, $1 \times 10^{18}$ cm$^{-3}$, and $3 \times 10^{18}$ cm$^{-3}$, respectively. With 280 mW of power applied across the doped heater, the temperature in the Si waveguide is 350 K as per Fig. 5.21 (d). In contrast, the temperature remains at 300 K for the deep trench (Fig. 5.21 (e)) owing to the thermal shielding of the ring modulator. The charge concentration profile in the PN phase shifter is examined for different reverse bias voltages as depicted in Fig. 5.22 indicating that with increasing voltages, the charge concentration moves to the left. For traditional designs, the temperature elevation results in a considerable diffusion of



https://doi.org/10.7795/110.20260421B

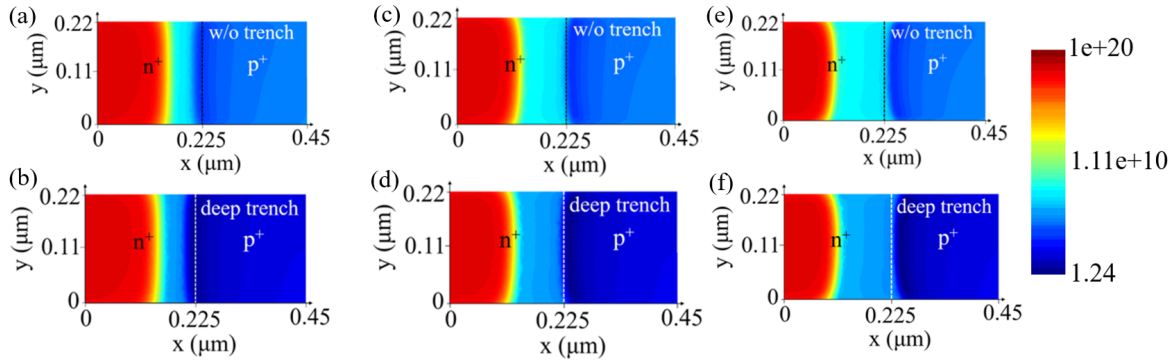


**Figure 5.22:** Charge distribution profiles of the n-type charge carriers of the PN phase shifter as shown in Fig. 5.21a in pink for the no trench (a, c, e) and deep trench (b, d, f) layouts considering reverse bias voltages of $-1\,\mathrm{V}$ (a, b), $-3\,\mathrm{V}$ (c, d), and $-5\,\mathrm{V}$ (e, f) supplied to the ring modulator with a heater power of 280 mW based on [187]. Here, the dashed lines represents the boundary of the $n^+$ and $p^+$ doped regions and the color bar represents the n-type charge concentration in $\mathrm{cm}^{-3}$ on a logarithmic scale ranging from 1.24 (blue) to $1 \times 10^{20}$ (red).

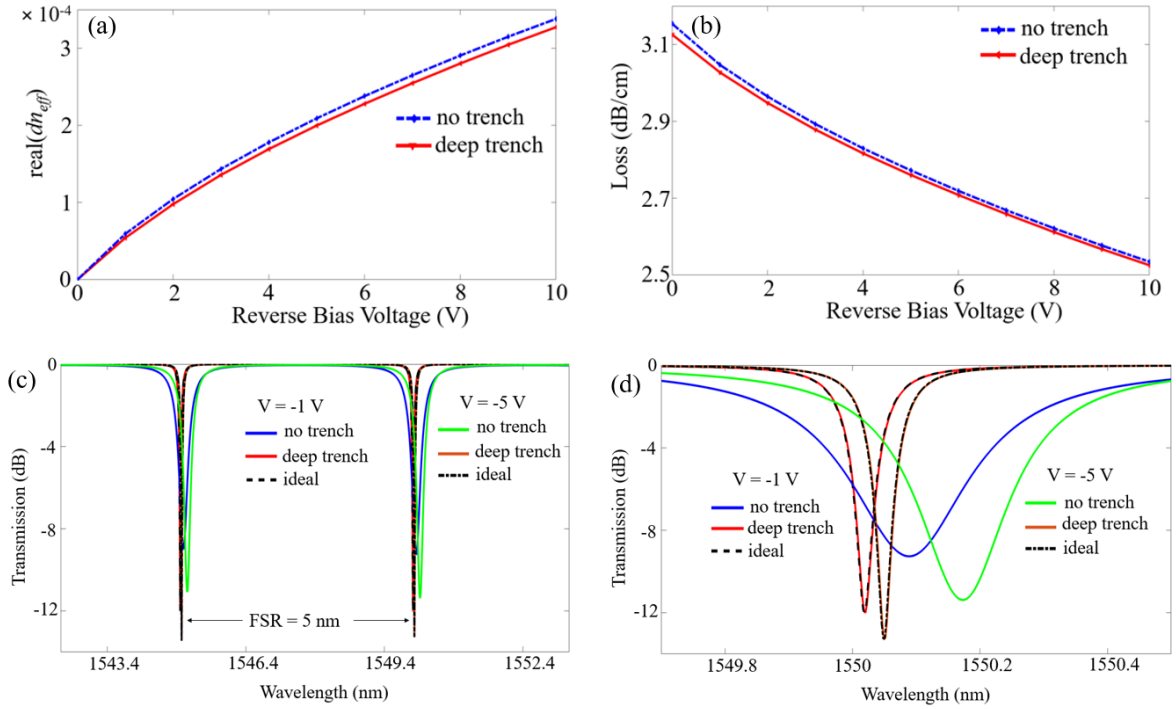


**Figure 5.23:** Variation of the (a) real part of the effective index ($\mathrm{Re}(\Delta n_{\mathrm{eff}})$) and (b) imaginary part (loss) in dB/cm corresponding to the reverse bias voltage applied across the silicon ring modulator, for without trench and deep trench scenarios. Transmission spectra of the ring modulator at (c) a wide range of wavelength and (d) a narrower range of wavelength for the ideal case, no trench, and deep trench layouts consídering reverse bias voltages of $-1\,\mathrm{V}$ and $-5\,\mathrm{V}$ based on [187]. In every scenario, a power of 280 mW is supplied across the doped heater.

$n^+$ and $p^+$ charge carriers into the PN junction deteriorating the modulator performance in terms of bandwidth and transmission characteristics, especially for compact PICs. However, modeling the deep trench thermally isolates the modulator with a significantly lower charge concentration.



https://doi.org/10.7795/110.20260421B

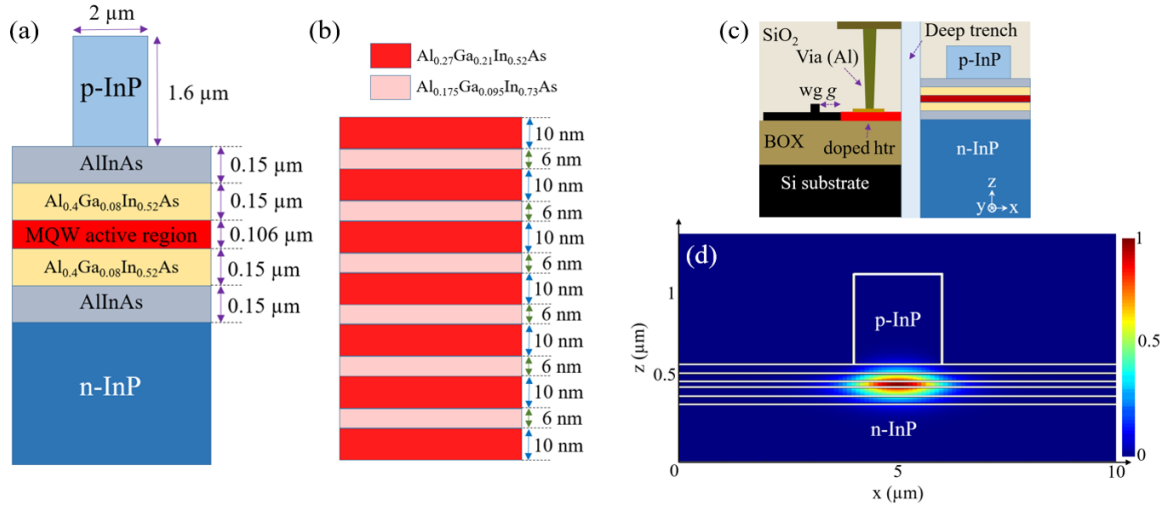


**Figure 5.24:** (a) Structural layout of the AlGaInAs/InP-based MQW laser and (b) depicts a magnified view of the MQW active region. (c) Sectional view depicting the laser together with the doped heater and waveguide. (d) Simulated optical mode distribution of the MQW laser based on [188].

As a consequence of silicon's large thermo-optic coefficient of $1.8 \times 10^{-4}$ $K^{-1}$ , a noticeable phase shift is caused in the PN phase shifter, modifying the effective refractive index $\Delta n_{\text{eff}}$ as well as the loss as demonstrated by the plots in Fig. 5.23 (a) and (b). Due to the thermal isolation provided by the deep trench, both $\Delta n_{\text{eff}}$ and loss are lower than the conventional modulator designs. In Fig. 5.23 (c) and (d), the transmission spectrum of the ring modulator is assessed at reverse biases of -1 V and -5 V with an free spectral range (FSR) of 5 nm which is defined as the wavelength spacing between two consecutive resonance modes of the ring resonator. From the magnified view in Fig. 5.23 (d), it is ascertained that a deep trench assisted modulator ensures a sharp and deep resonance which closely resemble the ideal resonance.

### E. Multi-Quantum Well (MQW) laser

While the silicon photonics platform does not support a native laser source, narrow linewidth and CW lasers [216] have the potential to be co-integrated via heterogeneous bonding like wafer bonding or III-V/IV bonding [217–219]. As such, the integrated laser sources can generate unwanted heat in the PICs and are susceptible to thermal interference from neighboring elements. AlGaInAs/InP MQW lasers, however, offers reliable operation even at higher temperatures [220].

For gauging the thermal interaction effects in PICs, the 1.3 $\mu$m AlGaInAs/InP-based MQW laser is simulated on a SOI platform as depicted in Fig. 5.24 (a), (b), and (c) [188]. For evaluating the harshest thermal conditions, the doped heater is meticulously located between the laser and a nearby waveguide (Fig. 5.24 (c)). Nonetheless, this preliminary investigation excludes self-heating, which is likely to further deteriorate the performance. The doped Si heater, waveguide (wg), and the trench model with the corresponding parameters is adapted from Section 5.2.1. Using the MODE solver of Lumerical [122] which uses the FDE method, the optical mode profile considering the fundamental Transverse Electric mode is evaluated



https://doi.org/10.7795/110.20260421B

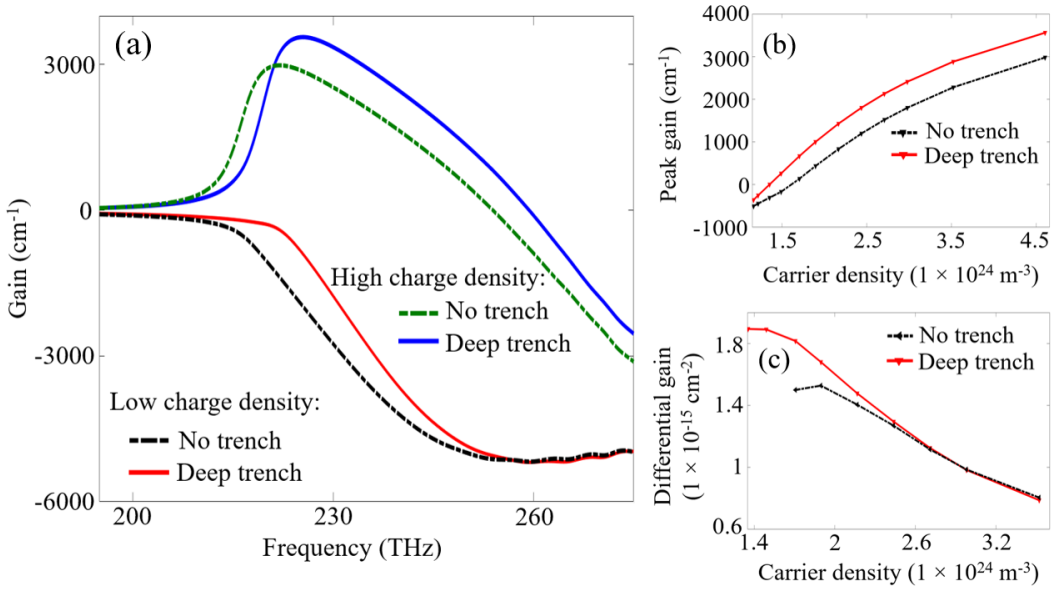


**Figure 5.25:** (a) Plot of the MQW laser gain ($cm^{-1}$) as a function of frequency in THz for high ($4.60 \times 10^{24}\,m^{-3}$) and low ($1.16 \times 10^{24}\,m^{-3}$) carrier densities. Evaluation of (b) peak gain ($cm^{-1}$) and (c) differential gain ($1 \times 10^{-15}\,cm^{2}$) as a function of carrier density ($1 \times 10^{24}\,m^{-3}$) based on [188]. For every scenario, the no trench and deep trench configurations are evaluated.

and its effective index and group index is determined. The mode profile confirms that the optical modes are restricted within the active region of the MQW laser as per Fig. 5.24 (d) which is necessary in order to have a high optical gain and stable laser operation.

When a power of 320 mW is applied across the heater, the effective temperature in the MQW laser core is 350 K, which alters its gain characteristics negatively. Nevertheless, incorporating a deep trench thermally isolates the laser and the active region stays at an ambient temperature of 300 K thus enhancing the laser performance in terms of gain under high carrier density, as is visualized in Fig. 5.25 (a). For an elevated carrier density of $4.60 \times 10^{24}\,m^{-3}$, the peak gain reaches $3562\,cm^{-1}$, suggesting an improvement of 20 % in the peak gain as per Fig. 5.25 (b). Additionally, the differential gain, which is defined as the rate at which the optical gain varies with the carrier density, is also enhanced for lower charge carrier densities (Fig. 5.25 (c)). All in all, the deep trench successfully alleviates the thermal crosstalk in MQW lasers [188].

### F. Avalanche photodetector (APD)

Silicon-Germanium (Si-Ge) APDs featuring a thin multiplication region [221, 222] are optimal for high-speed and energy-efficient optical receivers owing to their multi-fold advantages in PICs like suppressed dark current, lower operating voltage, and higher bandwidth. The thin multiplication region ensures lower noise along with faster transit time making CMOS compatible and compact Si-Ge APDs perfect for next-generation optical communication systems applications.

The geometry of the heater, $100\,\mu m$ long Si-Ge APD, and the waveguide (wg) on the SOI platform with the deep trench and a magnified view of the Si-Ge APD is illustrated in Fig. 5.26



https://doi.org/10.7795/110.20260421B

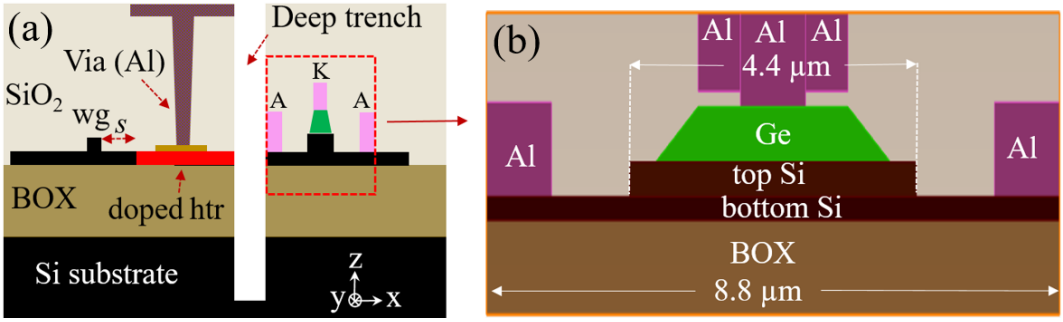


**Figure 5.26:** (a) Sectional view of the Si-Ge APD with the doped Si heater, thermally tuned waveguide and a deep trench. (b) Magnified perspective of the Si-Ge APD depicting the Si, Ge layers and Al electrodes based on [190]. For both the subfigures the x-axis is compressed for clarity.

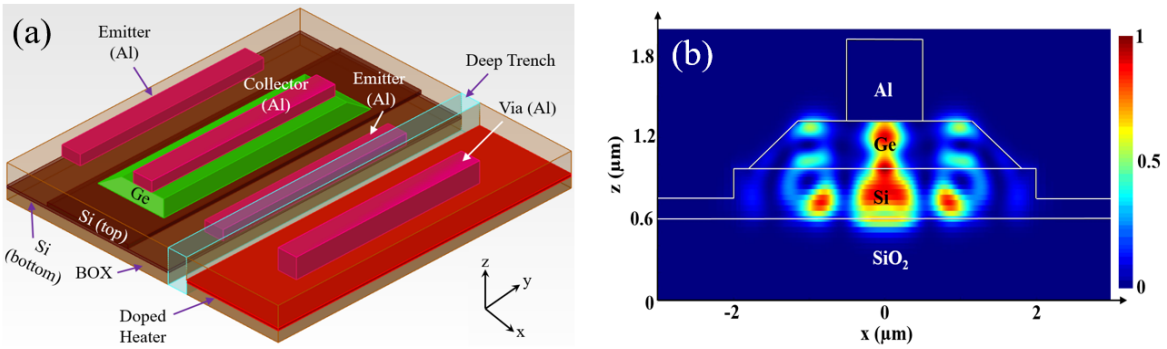


**Figure 5.27:** (a) Three-dimensional illustration of the Si-Ge APD with the doped Si heater, thermally tuned waveguide and a deep trench. (b) Optical mode distribution measured at 5 $\mu$m away from the Si-Ge front edge based on [189].

(a) and (b), respectively [190]. A three dimensional view of this geometry and the optical mode profile is given in Fig. 5.27 (a) and (b), respectively, affirming that the optical modes are contained in the Si and Ge layers in the APD [189]. To model the worst-case thermal crosstalk scenario, the $N^{++}$ doped Si heater is located centrally amid the thermally tuned waveguide (wg) and the Si-Ge APD. The SOI design parameters, doped heater and waveguide (wg) features, and the deep trench dimensions are adapted from Section 5.2.1. As can be seen from the magnified view (Fig. 5.26 (b)), the APD has a multi-layered structure starting with the bottom Si layer with a width of 8.8 $\mu$m and a thickness of 0.15 $\mu$m followed by a top Si layer with 4.4 $\mu$m width and 0.22 $\mu$m thickness. This is followed by the 0.35 $\mu$m thick Ge layer and Al electrodes. The APD Si layers form the multiplication region and the Si doping profiles have vertically aligned $n^+$, i, and $p^-$ Si wells with doping concentrations of $1 \times 10^{20}$ cm$^{-3}$, $1 \times 10^{15}$ cm$^{-3}$, and $1 \times 10^{17}$ cm$^{-3}$, respectively. The $p^+$ and $p^{++}$ wells in Ge have doping levels of $1 \times 10^{18}$ cm$^{-3}$ and $1 \times 10^{20}$ cm$^{-3}$, respectively and they start at the bottom of the Ge layer extending through a thickness of 0.35 $\mu$m and 0.37 $\mu$m, respectively [223]. The distribution of the p-type charge carriers considering the bottom and top Si layers of the APD is depicted in Fig. 5.28 (a) and (b) considering no trench and deep trench models, respectively. When the trench is not included in the design, the Si layer in the APD heats up to 400 K under 3 V of reverse bias and 290 mW power across the heater. Consequently, the diffusion of $p^+$



https://doi.org/10.7795/110.20260421B

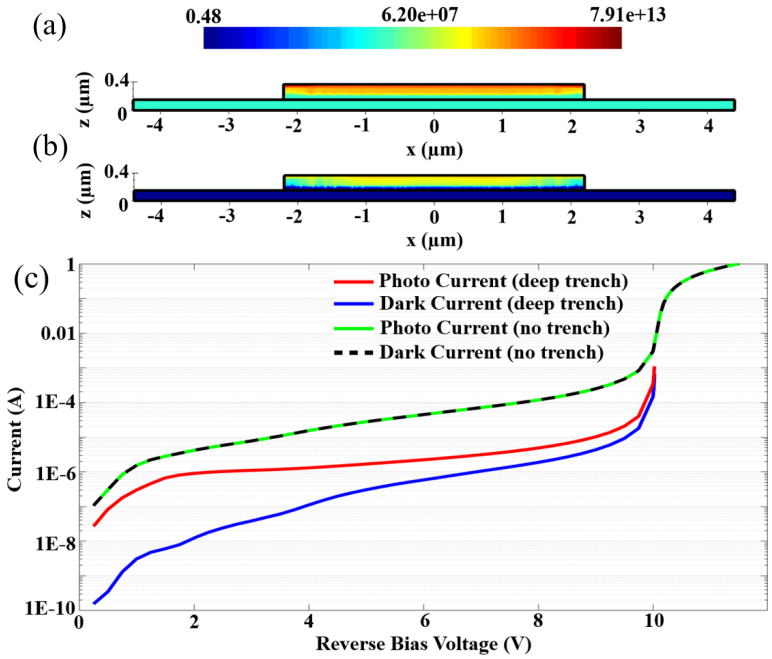


**Figure 5.28:** P-type charge carrier profile for (a) no trench and (b) deep trench scenarios at the top and bottom Si layers of the APD considering a heater power of 290 mW and a reverse bias of 3 V. The color bar at the top depicts the p-type charge concentration in $cm^{-3}$ on a logarithmic scale ranging from 0.48 (blue) to $7.91 \times 10^{13}$ (red). (c) Photo current and dark curent as a function of voltage for the Si-Ge APD for no trench and deep trench designs for a heater power of 290 mW based on [190].

charge carriers across the top and bottom Si APD layers substantially deteriorates the device performance when the bandwidth and overall performance metrics are gauged. Nonetheless, with a deep trench integrated design, the APD is thermally decoupled from the doped heater, reducing charge diffusion (Fig. 5.28 (b)) and enhancing the device performance.

For investigating the photocurrent and dark current in the APD, the reverse bias voltage across the Al electrodes is varied until 12 V as depicted in Fig. 5.28 (c). In the absence of trench, the heightened charge carrier concentration ensues in high amounts of photocurrent and dark current practically indistinguishable for any given voltage. With the deep trench, however, the dark current and photocurrent are lower and distinct owing to the thermal shielding, with breakdown voltage observed at 10.02 V. With the simulation setup in Fig. 5.29 (a), the performance of the Si-Ge APD is gauged in terms of eye diagram at 40 Gbps utilizing OOK modulation and a PRBS sequence of $2^{10} - 1$ with a multiplication factor ($M$) of 5. With the deep trench the APD demonstrates a higher BER and enhanced extinction ratio (ER) of $6.1 \times 10^{-8}$ and 15.86 dB as opposed to $1.96 \times 10^{-4}$ and 3.92 dB for no trench [190].

### G. Uni-travelling carrier photodiode

While the ultrafast photodetectors [225] are critical for advanced implementations like high-speed optical interconnects and fiber-optic links, they are still restricted by the slower hole mobility as compared to the electrons, allowing for an asymmetrical and delayed response. As the holes move at a lower speed compared to the electrons, the photocurrent produced has a temporal drag as the response of the leading edge is much faster than the trailing edge which



https://doi.org/10.7795/110.20260421B

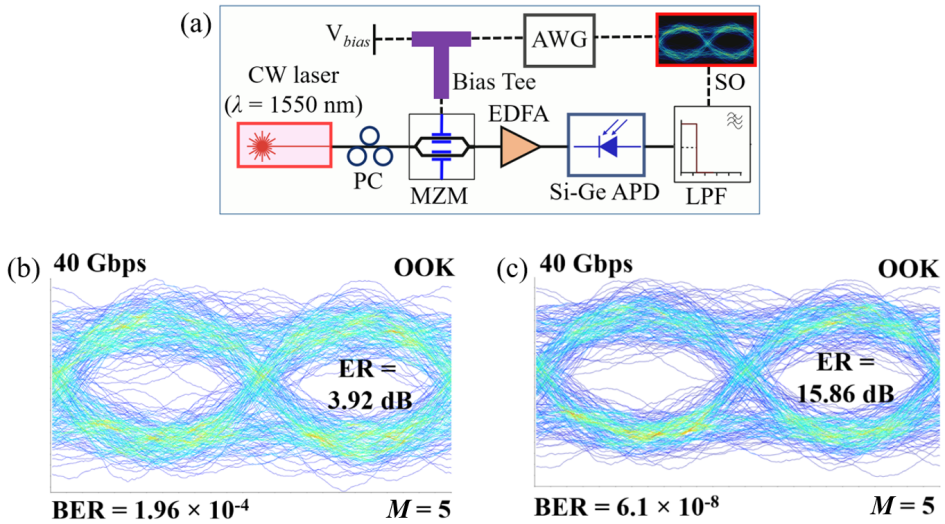


**Figure 5.29:** (a) Simulation confíguration for the eye diagram analysis consisting of CW laser, polarization controller (PC), Mach-Zehnder Modulator (MZM), Arbitrary Waveform Generator (AWG) with non-return-to-zero (NRZ) encoding, Erbium-doped fiber amplifier (EDFA), a 40 GHz Low pass filter (LPF), Si-Ge APD and Sampling Oscilloscope (SO). Eye diagrams of the avalanche photodetector operating for on-off keying (OOK) modulation at 40 Gbps for (b) no trench and (c) deep trench based on [190].

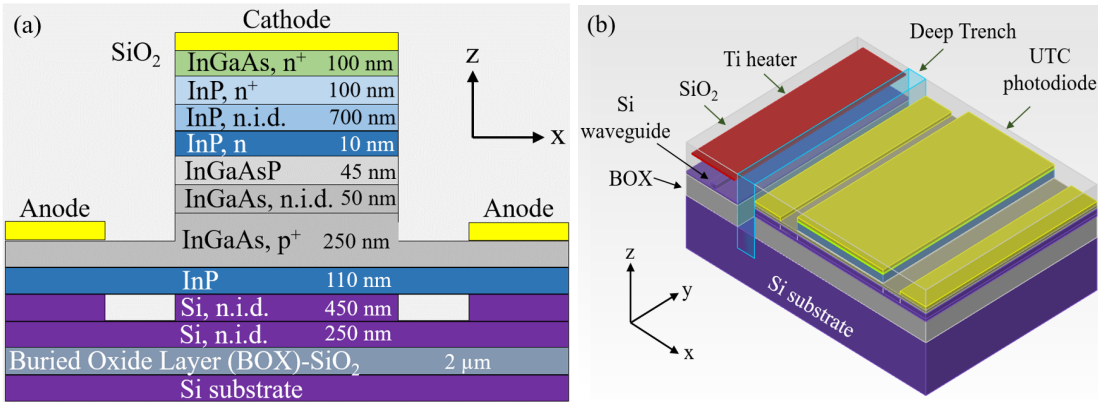


**Figure 5.30:** (a) Schematic representation the InP/InGaAs UTC photodetector [224] and (b) the three dimensional representation of the photodetector along with the Titanium heater and the deep trench design based on [191].

eventually leads to pulse broadening and compromises the modulation speed of the photodetector. For UTC photodetectors [226–229], electrons alone act as the active carriers, ensuing in reduced transit times and improved photoresponse. They can exhibit bandwidths ranging up to 100 GHz in III-V waveguide configurations, and 155 GHz for integrated silicon nitride (SiN) platforms. Additionally, the UTC photodetectors are promising for photomixing applications, ensuring high-purity THz signal generation for next-generation THz wireless communication. Nevertheless, when integrated in a PIC, the thermal crosstalk is a key challenge and needs to be mitigated.

The Indium Phosphide / Indium Gallium Arsenide (InP/InGaAs) UTC photodiode design [191, 227] comprises of a 700 nm thick not-intentionally-doped (n.i.d.) Indium Phosphide (InP) collector layer, an Indium Gallium Arsenide (InGaAs) and InP bonding layer of 250 nm



https://doi.org/10.7795/110.20260421B

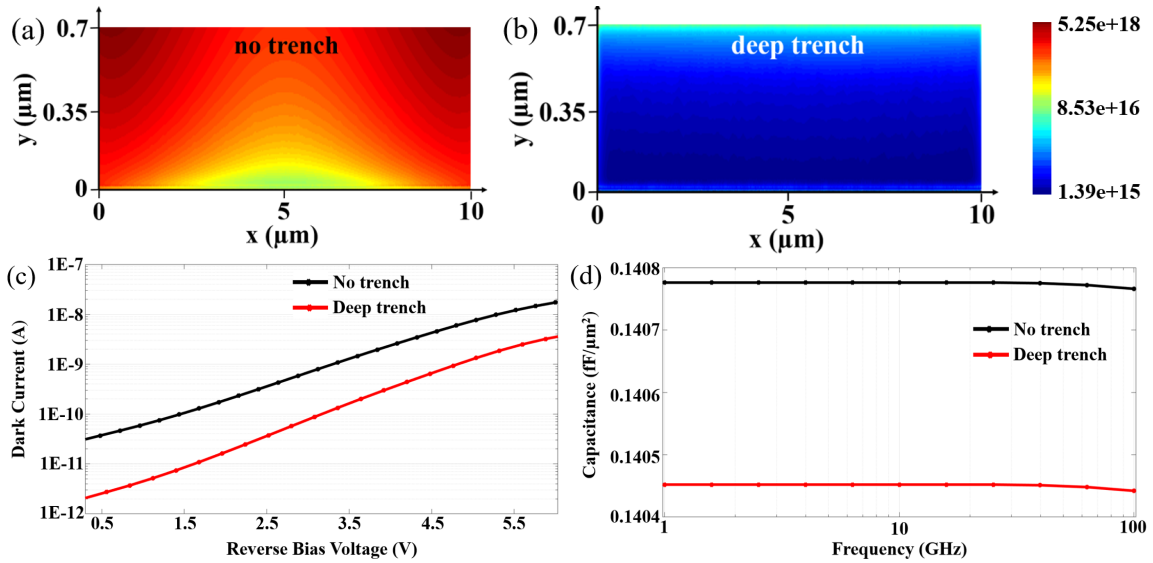


**Figure 5.31:** Spatial distribution of the n-type charge carriers in the 700 nm thick InP, n.i.d. collector layer shown in Fig. 5.30a for (a) no trench and (b) deep trench configurations where the color scale indicates the charge concentration in $cm^{-3}$ on a logarithmic scale ranging from $1.39 \times 10^{15}$ (blue) to $5.25 \times 10^{18}$ (red). (c) Current–voltage and (d) capacitance–frequency characterization of the UTC photodetector. In every scenario, the heater power applied is 250 mW based on [191].

and 100 nm thickness, respectively as described in Fig. 5.30 (a). To evaluate the most severe thermal condition, a Ti heater with dimensions discussed in Section 5.1.1 is located adjacent to the UTC photodetector. For crosstalk alleviation, an air-filled deep trench having proportions described in Section 5.2.1 was positioned amid the heater and the UTC photodetector, the three-dimensional view of which is illustrated in Fig. 5.30 (b). This causes the UTC to be thermally isolated and remain at the ambient temperature of 300 K even at a heater power of 250 mW. The CHARGE solver of Lumerical [122] was used to determine the charge carrier concentration, model the dark current, and extract the capacitance of the photodetector. The design exhibits a reduced charge diffusion and decreased charge carrier concentration in the InP collector layer (Fig. 5.31 (b)) as opposed to the no trench design (Fig. 5.31 (a)). The dark current is reduced to approximately 2.5 pA for 0.5 V of reverse bias as per the current-voltage plot in Fig. 5.31 (c). Further, a minor drop in the capacitance is observed (Fig. 5.31 (d)), affirming that the deep trench assisted design outperforms its conventional counterpart [191].

### H. Silicon micro-ring switches

In advanced optical communication systems, Si micro-ring resonators [230, 231] are pivotal elements especially for optical switching and sensing applications, owing to their CMOS compatibility and easy incorporation into PICs. Additionally, silicon's high refractive index contrast eases the realization of dense, efficient, and scalable switching architectures [232] with ring resonator arrays.

For evaluating the thermal crosstalk performance, a segment of the $4 \times 4$ silicon photonic switching network [232] with the schematic diagram depicted in Fig. 5.32 (a) is simulated. A



https://doi.org/10.7795/110.20260421B

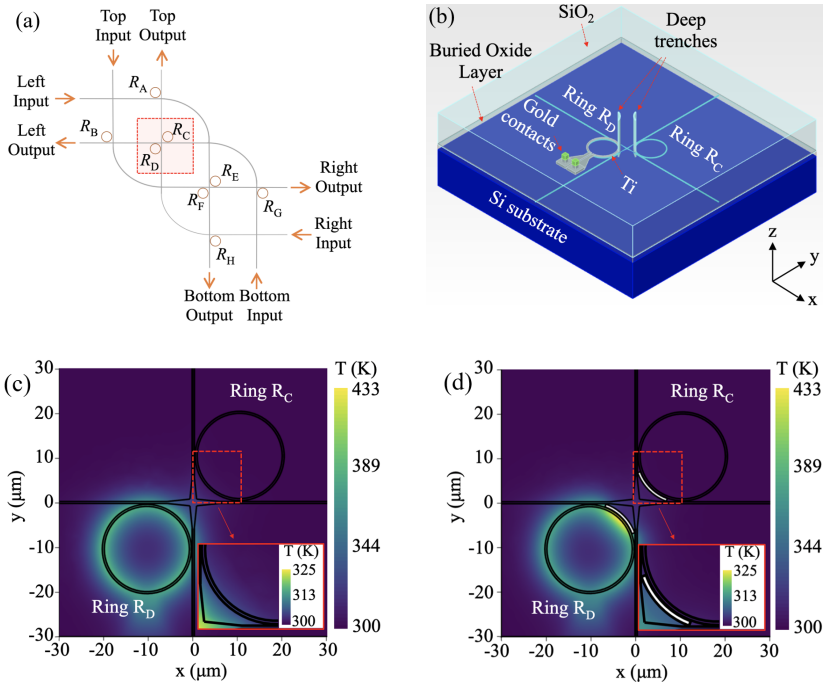


**Figure 5.32:** (a) Schematic diagram of the 4×4 optical routing network from [232]. Here, a part of the switch consisting of $R_C$ and $R_D$ as indicated inside the red box depicts the simulated section. (b) Three-dimensional model of the highlighted section consisting of the ring resonators (one is activated) and the deep trench to prevent unintentional thermal leakage into the adjacent ring. Heat distribution profiles of the silicon micro-ring resonators for (c) no trench and (d) deep trench scenario where the magnified views at the bottom left indicate the thermal impact on adjoining ring based on [192]. The color scale in (c), (d) represents temperature in Kelvin (K), ranging from 300 K (blue) to 433 K (yellow).

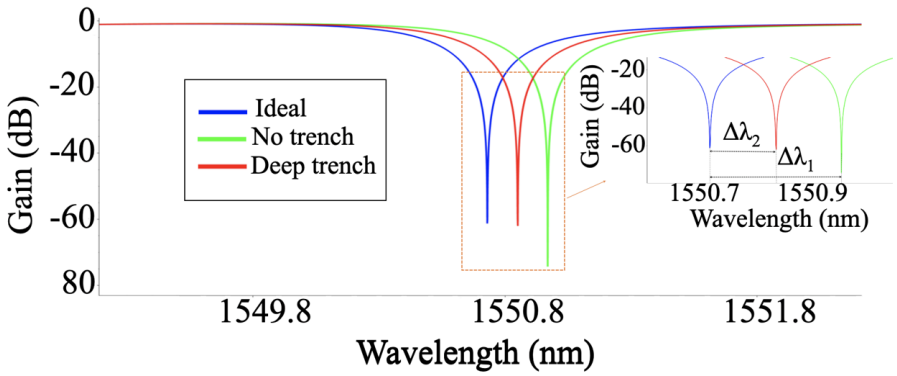


**Figure 5.33:** Simulated transmission response for ideal, no trench and deep trench scenarios depicted in blue, green and red respectively based on [192]. Here, the magnified view of the highlighted portion indicates the shift in the wavelengths for the three different scenarios.

three-dimensional model of the highlighted section in red (Fig. 5.32 (a)) is demonstrated in Fig. 5.32 (b) [192]. Here, the linear waveguides are 160 $\mu$m long, 0.45 $\mu$m thick, and 0.25 $\mu$m wide [233]. The rings $R_C$ and $R_D$ have a radius of 9.55 $\mu$m while being 0.45 $\mu$m thick, and at a distance of 0.185 $\mu$m from the bus waveguide. The ring is tuned with the Ti heater located 0.8 $\mu$m above the ring. For crosstalk mitigation, two air-filled deep trenches are introduced around the rings $R_C$ and $R_D$, each being 0.65 $\mu$m wide and beginning at 3 $\mu$m depth in the Si substrate. The trenches curve around one-eighth of the ring circumference along the bus waveg-



https://doi.org/10.7795/110.20260421B

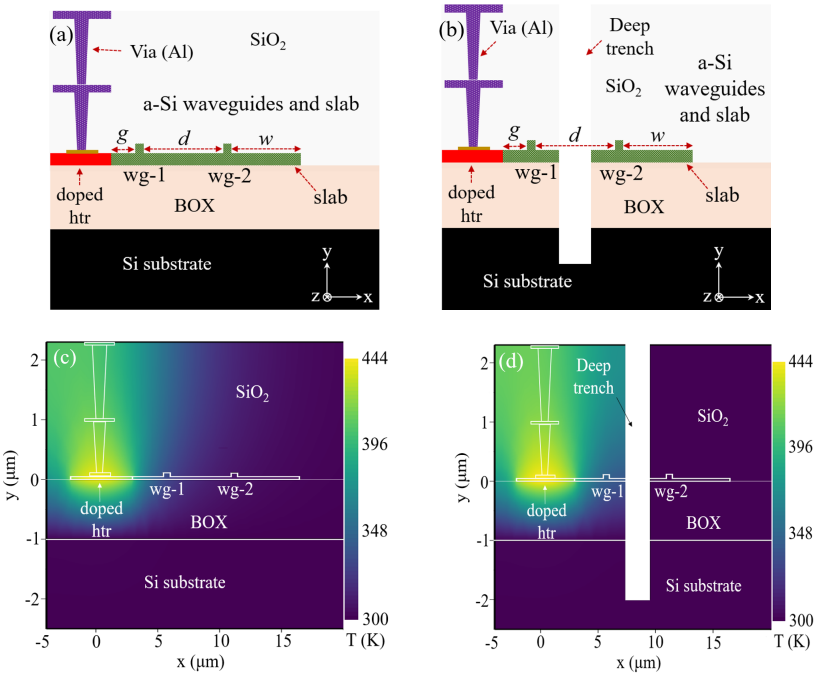


**Figure 5.34:** Cross-sectional geometry and heat distribution profiles of the amorphous Si waveguides (wg-1 and wg-2) with an $N^{++}$ doped Si heater, for (a, c) no trench and (b, d) deep trench configuration based on [193]. The deep trench is 2 µm wide and starts at a depth of 2 µm from the silicon substrate. The color scale in (c), (d) represents temperature in Kelvin (K), ranging from 300 K (blue) to 444 K (yellow).

uide intersection as per the white region in Fig. 5.32 (b). The HEAT and INTERCONNECT solvers of Lumerical [122] are used to evaluate the temperature profile of the thermal switch and the system-level switching analysis, respectively. The temperature distribution profiles for no trench and deep trench models are depicted in Fig. 5.32 (c) and (d), respectively. When the ring $R_D$ is heated to 382 K with the Ti heater, the adjacent ring $R_C$ reaches 304.5 K without a trench. Deep trench model corresponds to effective thermal insulation and the temperature drops to 301.5 K. The spectral response of the micro-ring resonator was plotted in Fig. 5.33 for no trench and deep trench models. Under ideal circumstances with no unwanted thermal effects, the inactive ring remains at 300 K. From the magnified view, it is ascertained that for the no trench model, there is a wavelength shift of $\Delta\lambda_1 = 0.24$ nm equating to a frequency deviation of 29.92 GHz, while for the deep trench configuration, the wavelength shift is narrowed down to $\Delta\lambda_2 = 0.12$ nm equating to a frequency deviation of 14.95 GHz. Thus, the deep trench minimizes crosstalk ensuring only half the resonance shift with improved network switching [192].

### 5.2.2 Amorphous Silicon platform

Beyond structural design, the thermal crosstalk in PICs is greatly influenced by the choice of materials in the device construction. Section 5.1.2 demonstrates the superiority of $N^{++}$ doped heaters in suppressing the thermal crosstalk as compared to Ti heaters considering thermally tuned crystalline silicon (c-Si) rib waveguides. Nevertheless, it is possible to fabricate PICs compatible with CMOS technology with hydrogenated amorphous silicon (a-Si) [234] using



https://doi.org/10.7795/110.20260421B

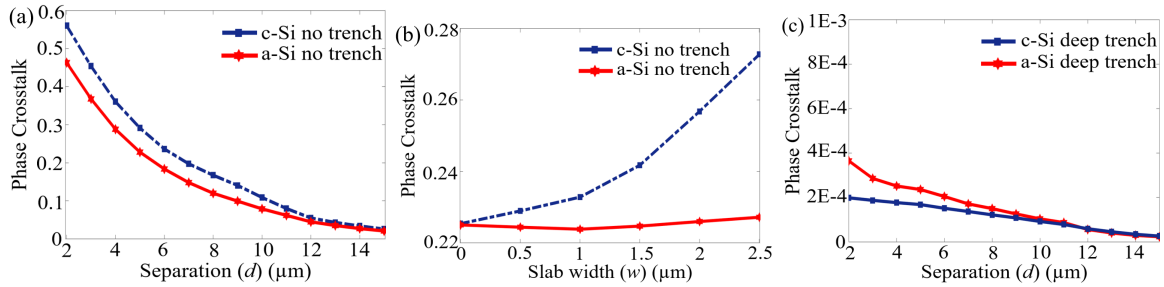


**Figure 5.35:** (a) Phase crosstalk measured across the secondary waveguide (wg-2) as a function of the separation $d$ between the two waveguides (wg-1 and wg-2) in $\mu$m for the no trench scenario. (b) Phase crosstalk versus slab width $w$ in $\mu$m for the no trench scenario. (c) Phase crosstalk measured across the secondary waveguide (wg-2) as a function of the separation $d$ between the two waveguides (wg-1 and wg-2) in $\mu$m for the deep trench scenario based on [193]. In each case, amorphous silicon (a-Si, red) and crystalline silicon (c-Si, blue) are compared.

chemical vapor deposition [235]. Considering the significantly lower thermal conductivity of a-Si around 1.8 W/(m·K) as opposed to 90 W/(m·K) for c-Si, a-Si can be viable for use in compact PICs where thermal crosstalk poses a key challenge.

The integrated $N^{++}$ doped Si heater design with two waveguides (wg-p and wg-s) based on c-Si is previously demonstrated in Section 5.1.2. In this simulated design as depicted in Fig. 5.34 (a, b), a-Si is used as the material for the slab region and for the waveguides (wg- and wg-2). To further alleviate the thermal crosstalk, an air-filled deep trench with parameters previously discussed in Section 5.2.1 is implemented between the two waveguides as per Fig. 5.34 (b) [193]. The temperature distribution profile for the no trench and deep trench designs was simulated using the HEAT solver of Lumerical [122] and it is provided in Fig. 5.34 (c) and (d), respectively, clearly depicting the thermal isolation provided by the deep trench where the wg-2 remains at the ambient temperature of 300 K at a power of 250 mW across the integrated $N^{++}$ doped Si heater. The phase crosstalk, which is the ratio of the phase shifts in wg-2 and wg-1, is determined for different waveguide spacings $d$ and slab widths $w$ as per Fig. 5.35 (a, b, c). It is evident from Fig. 5.35 (a, b) that with a-Si, the design has a lower phase crosstalk as compared to c-Si. Further, with deep trench, both a-Si and c-Si show extremely low values of phase crosstalk (Fig. 5.35 (c)), confirming the usefulness of trench assisted a-Si designs.

## 5.3 Conclusion

To summarize, this chapter provides a thorough simulation analysis of thermal crosstalk mitigation techniques for several devices suitable for integration into CMOS compatible PICs. To start with, it was realized that the strip waveguide outperforms the rib waveguides ensuring enhanced phase and thermal stability. With integrated $N^{++}$ doped Si heater, the thermal characteristics are superior with lower phase crosstalk as opposed to the conventional metal heaters. With metal contacts, the overall power requirement increases in PICs, however, the influence on thermal crosstalk is marginal. A notable improvement in crosstalk mitigation is observed for deep trench designs with a minor increase in the cooling time-constant. Such designs have shown performance improvement for a variety of devices like PN phase shifters,



https://doi.org/10.7795/110.20260421B

| Reference Number | Heater type | Air trench | External heat sink | CMOS ready | Thermal Crosstalk | PIC tested |
|---|---|---|---|---|---|---|
| [176] | Thin film | Yes | Yes | No | Moderate | Passive (MZI[a], MMI[b]) |
| [177] | $P^{++}$ Doped Silicon | No | No | Yes | Low | Passive (MZI[a], MMI[b]) |
| [180] | Metal heater | No | No | Yes | Low | Passive (ring) |
| [42, 181] | Metal heater | No | No | Yes | Low | Active and Passive (ring, MZI[a]) |
| [182] | $N^{++}$ Doped Silicon | Yes | No | Yes | Low | Passive (MZI[a]) |
| [96] | $N^{++}$ Doped Silicon | Yes | No | Yes | Low | Active and Passive (ring, PN PS[c], attenuator) |
| [105], this work | $N^{++}$ Doped Silicon | Yes (Deep trench) | No | Yes | Very low | Active and Passive (modulator, PN PS[c]) |

MZI[a] = Mach-Zehnder interferometer, MMI[b] = Multi-mode interferometer, PN PS[c] = PN phase shifter.

**Table 5.2:** Thermal crosstalk comparison for proposed designs with different types of heaters

modulators, switching networks, etc. Further alleviation of thermal crosstalk is observed with the amorphous silicon platform with a much lower thermal conductivity as compared to crystalline silicon.

A comparison of our work [105] with the previous studies on thermal crosstalk is offered in Table 5.2. The heater design shown in [176] was developed with thin-film integration. Nevertheless, the heater was not compliant with CMOS technology providing mediocre crosstalk alleviation and the design was validated only for passive components in the PICs. The studies demonstrated in [177] and [180] evaluated crosstalk behavior across multiple passive photonic elements like MZIs, MMIs, and micro-ring resonators. The designs followed CMOS fabrication standards, ensuring easy integration into the industry-standard photonic manufacturing workflows with scalable PICs. The works shown in [42, 181] illustrate metal heaters capable of thermally tuning integrated photonic devices, taking into account both passive and active components like micro-ring resonators and MZIs. Despite being CMOS compatible, they



https://doi.org/10.7795/110.20260421B

lacked supplementary thermal isolation mechanisms such as air-filled trenches or auxiliary heat sinks. Consequently, the devices exhibited a low, but not negligible thermal crosstalk. The study reported in [182] and our previous work [96] have explored doped Si heaters integrated with thermal isolation structures based on air-filled trenches. While [182] examines a passive MZI, [96] extends the usage of the heaters to both active and passive components like ring resonators, phase shifters based on PN junctions, and integrated optical attenuators. Both of these designs have allowed for significantly low thermal crosstalk. The work in this chapter [105] simulates deep trench designs that can provide very effective thermal isolation, thus effectively reducing thermal crosstalk to extremely low values in both passive devices and active devices like PN phase shifters, modulators [184, 185, 187], avalanche [189, 190] and uni-travel carrier photodetectors [191], etc.

To sum it all up, combating thermal crosstalk is a multi-dimensional challenge entailing integrated doped heaters for control, structural obstructions like air-filled oxide and deep trenches for isolation, and material selections like a-Si for enhanced thermal management. Combining these methods together allow for robust, scalable, and thermally efficient photonic systems with PICs capable of performing high bandwidth signal processing.



https://doi.org/10.7795/110.20260421B

# 6

# Summary and future work

This thesis delves into the generation, detection, and fidelity challenges concerning high bandwidth signal processing in PICs. Uniting conceptual frameworks with simulations and experimental validations, the thesis emphasizes on the key non-idealities and thus enhances the design and reliability of crosstalk-free optical communication systems that can be efficiently scaled into the PICs.

The investigation began with the generation of high-quality Nyquist pulse sequences through the direct synthesis of a rectangular optical frequency comb locked in phase generated by sinusoidally driven MZMs. Nevertheless, system non-idealities like comb ripple, inadequate optical suppression of sidebands, and roll-off in the optical bandpass filters for DD systems can limit the overall system performance and restrict the temporal and spectral fidelity of the pulses. These imperfections were analyzed experimentally for three-line OFCs and through simulations across three-line, five-line and nine-line OFCs, and the quality of the pulses were quantified in terms of the RMSE. The comb ripple and SSR analysis revealed that the nine-line OFCs have enhanced performance with the lowest RMSE. With cascaded MZMs, a higher number of comb lines can be produced, but the flatness deteriorates owing to the non-linearity of the modulator and the limited RF bandwidth. Such Nyquist pulse sequences have been generated on an integrated platform with on-chip silicon MZMs as well with different roll-off $\beta$ values of the optical filter indicating the best performance with an RMSE of 0.7 % for lowest $\beta$ values.

The following chapter discussed the DD method with a single photodiode as a viable low-complexity alternative to coherent detection for short-reach and cost-effective applications. Two practical impairments, namely the comb ripple and optical filter roll-off $\beta$ were investigated though simulations and proof-of-concept experimental validation for a DD based orthogonal sampling system with three-line OFCs. For systems with a considerable ADC jitter, both positive and negative comb ripple contribute to a larger RMSE and lower SINAD and ENOB. When the ripple surpasses 0.5 dB, there is a noticeable reduction in the robustness of the orthogonal sampling system. Varying the optical filter roll-off $\beta$ for the system revealed that the signal quality remains stable until a critical threshold, after which it declines sharply. For broadband signals, the orthogonal sampling consistently exhibited superior performance over conventional DD systems with electronic ADCs across different jitter levels and roll-off



https://doi.org/10.7795/110.20260421B

values, ensuring a 1.5 times improvement of bandwidth due to down-conversion, and better Q-factors and eye diagrams at the output for higher ADC jitters.

Lastly, the critical issue of thermal crosstalk was analyzed across multiple devices suitable for integration into the CMOS compatible PICs. Thorough simulations reveal the crosstalk reduction with integrated $N^{++}$ doped Si heater as compared to the conventional metal heaters. With air-filled deep trenches, the thermal crosstalk reduces to extremely low values as experienced in multiple devices in PICs like modulators, ring resonators, avalanche photodetectors, etc. As compared to the no trench designs or oxide trench designs, it offers significantly reduced thermal coupling, resulting in improved thermal isolation and stability. Further reduction in crosstalk has been demonstrated with amorphous silicon, owing to its significantly lower thermal conductivity relative to crystalline silicon.

In essence, this thesis provides a comprehensive overview of the practical constraints in high-bandwidth optical systems, from production of Nyquist pulses with phase locked OFCs to their application in DD based orthogonal sampling. Additionally, with the methods mentioned to curtail thermal crosstalk in PICs, it is possible to have robust, scalable, and thermally optimized photonic systems for high bandwidth signal processing using PICs.

## Future work

To build upon the methodologies and results in this thesis, future investigations can pursue the following ideas:

**Experimental Validation of system performance with non-idealities in mm-wave regime:** For the next phase of research, experimental evaluation of the system performance under non-idealities like ripple, SSR, and optical filter roll-off $\beta$ can be performed for three-line and five-line OFCs at higher frequency spacing between the comb lines, where several effects like bandwidth characteristics, phase coherence, etc. can be thoroughly analyzed. This allows for a comprehensive performance characterization in the millimeter-wave (mm-wave) range and facilitate system assessments customized for high-accuracy metrology applications.

**Sampling analysis for accurate metrological systems:** Waveform metrology methods can be adopted to have a deeper understanding of the Nyquist pulse based sampling as opposed to the conventional electrical sampling. This encompasses extracting the system's transfer function along with its associated measurement uncertainty, which is formulated as a covariance matrix which takes into account the correlation between all measurement points, and facilitating metrology-based error correction. Furthermore, performance metrics like the jitter, ENOB, linearity, and effective bandwidth can be derived together with the uncertainty estimates, ensuring a quantitative performance comparison as opposed to the other state-of-the-art sampling approaches.

**Performance evaluation of DD based orthogonal sampling with nine-line OFCs:** To extend the experimental work done in this thesis, the approach of using orthogonal sampling for



https://doi.org/10.7795/110.20260421B

DD systems can be extended to nine-line OFCs along with broadband communication signals as input, allowing for improved temporal resolution and enhanced spectral shaping. This scheme can be adopted within PICs optimal for cost-sensitive and scalable applications including data centers and sensor networks.

**Integrated PICs with air-filled deep trench model:** To realize experimental validation of the benefits of the deep trench design, full photonic subsystems including elements like modulators, filters, and photodetectors can be integrated into deep trench assisted PICs. This will enable practical realization of a complete link demonstrating crosstalk-free high-bandwidth signal processing under real-world conditions.



https://doi.org/10.7795/110.20260421B

https://doi.org/10.7795/110.20260421B

# List of Supervised Thesis and Publications

## Bachelor's Thesis

1. Rebecca Cubas Heim, "Simulation Study of Thermal Switch using Thermally Active Ring Resonators", Technical University of Braunschweig, March 9, 2023, supervised by **S. De**, K. Singh.

## Journal Articles

1. **S. De**, A. Misra, R. Das, T. Kleine-Ostmann and T. Schneider, "Analysis of Non-Idealities in the Generation of Reconfigurable Sinc-Shaped Optical Nyquist Pulses," in *IEEE Access*, vol. 9, pp. 76286-76295, 2021.

2. **S. De**, K. Singh C. Kress, R. Das, T. Schwabe, S. Preußler, T. Kleine-Ostmann, J. C. Scheytt, and, T. Schneider "Roll-Off Factor Analysis of Optical Nyquist Pulses Generated by an On-Chip Mach-Zehnder Modulator," in *IEEE Photonics Technology Letters*, vol. 33, no. 21, pp. 1189-1192, 2021.

3. **S. De**, R. Das, R. K. Varshney, and T. Schneider, "CMOS-Compatible Photonic Phase Shifters With Extremely Low Thermal Crosstalk Performance," *Journal of Lightwave Technology*, vol. 39, no. 7, pp. 2113–2122, 2021.

4. K. Singh, R. Das, A. Venugopalan, **S. De**, M. I. Hosni, L. Zhou, and T. Schneider, "Real-time reconfigurable on-chip photonic frequency decoder," *Optics Express*, vol. 31, no. 19, pp. 30160–30170, 2023.

5. Y. Mandalawi, J. Meier, K. Singh, M. I. Hosni, **S. De** and T. Schneider, "Analysis of Bandwidth Reduction and Resolution Improvement for Photonics-Assisted ADC," in *Journal of Lightwave Technology*, 41(19), 6225–6234, 2023.

6. Y. Mandalawi, M. I. Hosni, J. Meier, K. Singh, **S. De**, R. Das, and T. Schneider, "Integrated segmented IQ-modulator for orthogonal sampling and multi-level high-bandwidth signal generation," *Optics Letters*, vol. 49, no. 9, pp. 2193–2196, 2024.



https://doi.org/10.7795/110.20260421B

## Book Chapters

1. **S. De**, Y. Mandalawi, R. Das, and T. Schneider, “Metrological Analysis of Non-idealities for Photonics Assisted Signal Processing,” in T. Kürner, T. Doeker, T. Kleine-Ostmann, T. Schneider, D. Humphreys (editors), *Metrology for THz Communications - Findings from DFG FOR 2863 Meteracom, Springer Nature*, November 28$^{\text{th}}$, 2025.

2. **S. De**, Y. Mandalawi, and R. Das, “Error Metrics for Photonics Assisted Signal Processing,” in T. Kürner, T. Doeker, T. Kleine-Ostmann, T. Schneider, D. Humphreys (editors), *Metrology for THz Communications - Findings from DFG FOR 2863 Meteracom, Springer Nature*, November 28$^{\text{th}}$, 2025.

3. **S. De**, Y. Mandalawi, R. Das, and M. Weizel, "Integrated Photonics Assisted Signal Processing and Thermal Crosstalk," in T. Kürner, T. Doeker, T. Kleine-Ostmann, T. Schneider, D. Humphreys (editors), *Metrology for THz Communications - Findings from DFG FOR 2863 Meteracom, Springer Nature*, November 28$^{\text{th}}$, 2025.

## Conference Proceedings

1. **S. De**, R. Das, T. Kleine-Ostmann and T. Schneider, "Characterization of non-idealities in optical Nyquist pulses for THz signal sampling metrology," *46th International Conference on Infrared, Millimeter and Terahertz Waves (IRMMW-THz)*, Chengdu, China, 2021, pp. 1-2.

2. **S. De**, J. Meier, Y. Mandalawi, K. Singh, A. Venugopalan, D. Yadav, R. Das, N. Meyne, K. Baaske, T. Kleine-Ostmann, and T. Schneider, "Comb flatness dependence for orthogonally sampled high bandwidth signals," in *Proc. SPIE 12994, Terahertz Photonics III*, paper 1299407, 18 June 2024.

3. **S. De**, J. Meier, Y. Mandalawi, A. Venugopalan, P. Mandal, R. Das, N. Meyne, K. Baaske, T. Kleine-Ostmann, and T. Schneider, "Optical Filter Roll-off Analysis for Orthogonal Sampling in a Direct Detection System," in *Proc. 2025 16th German Microwave Conference (GeMiC)*, pp. 45–48, 2025.

4. **S. De**, J. Meier, Y. Mandalawi, R. Das, N. Meyne, K. Baaske, T. Kleine-Ostmann, and T. Schneider, "Orthogonal Sampling with a Single Photodiode," in *Proc. 2025 Conference on Lasers and Electro-Optics Europe & European Quantum Electronics Conference (CLEO/Europe-EQEC)*, Munich, Germany, 2025, (accepted).

5. **S. De**, R. Das, T. Kleine-Ostmann, and T. Schneider, "Athermal Travelling Wave Mach-Zehnder Modulators for Optical Interconnects," in *OSA Advanced Photonics Congress 2021, OSA Technical Digest*, Optica Publishing Group, 2021, paper NeF1B.4.

6. **S. De**, R. Das, T. Kleine-Ostmann, and T. Schneider, "Effect of Thermal Crosstalk on Travelling-wave Mach-Zehnder Modulator," in *Proc. 2021 Conference on Lasers*



https://doi.org/10.7795/110.20260421B

*and Electro-Optics Europe & European Quantum Electronics Conference (CLEO/Europe-EQEC)*, pp. 1–1, 2021.

7. **S. De**, R. Das, K. Singh, Y. Mandalawi, T. Kleine-Ostmann, and T. Schneider, "Thermal Crosstalk Mitigation in a Dual-Drive Mach-Zehnder Modulator," in *Proc. 2022 International Conference on Numerical Simulation of Optoelectronic Devices (NUSOD)*, pp. 27–28, 2022.

8. **S. De**, R. Das, K. Singh, Y. Mandalawi, T. Kleine-Ostmann, and T. Schneider, "Thermal Insulation of Silicon Ring Modulators in Densely-Packed Photonic Integrated Circuits," in *Proc. SPIE 12575, Integrated Optics: Design, Devices, Systems and Applications VII*, paper 125750C, 31 May 2023.

9. **S. De**, R. Das, K. Singh, Y. Mandalawi, T. Kleine-Ostmann, and T. Schneider, "Thermal-aware Multi-Quantum Well Laser," in *Frontiers in Optics + Laser Science 2022 (FIO, LS), Technical Digest Series*, Optica Publishing Group, 2022, paper JTu4A.51.

10. **S. De**, R. Das, K. Singh, Y. Mandalawi, T. Kleine-Ostmann, and T. Schneider, "Study of Thermal Crosstalk in Avalanche Photodetectors in THz Domain," in *Proc. 2022 47th International Conference on Infrared, Millimeter and Terahertz Waves (IRMMW-THz)*, pp. 1–2, 2022.

11. **S. De**, R. Das, K. Singh, Y. Mandalawi, T. Kleine-Ostmann, and T. Schneider, "Crosstalk Immune High-Speed Photonic Transmitter-Receiver System," in *Proc. 2024 15th German Microwave Conference (GeMiC)*, pp. 25–28, 2024.

12. **S. De**, R. Das, K. Singh, Y. Mandalawi, E. Baidoo, T. Kleine-Ostmann, and T. Schneider, "Crosstalk Resistant Integrated Uni-Traveling Carrier Photodetector," in *Proc. 2023 48th International Conference on Infrared, Millimeter, and Terahertz Waves (IRMMW-THz)*, pp. 1–2, 2023.

13. **S. De**, R. Das, K. Singh, Y. Mandalawi, T. Kleine-Ostmann, and T. Schneider, "Amorphous Silicon Based Crosstalk Resilient Photonic Phase Shifters," in *Proc. 2023 Conference on Lasers and Electro-Optics Europe & European Quantum Electronics Conference (CLEO/Europe-EQEC)*, pp. 1–1.

14. **S. De**, R. Das, K. Singh, Y. Mandalawi, T. Kleine-Ostmann, and T. Schneider, "Temperature Insensitive Avalanche Photodetectors," in *Optica Advanced Photonics Congress 2022, Technical Digest Series*, Optica Publishing Group, 2022, paper ITu3C.2.

15. **S. De**, Y. Mandalawi, A. Venugopalan, J. Meier, R. Das, K. Baaske, T. Kleine-Ostmann, L. Zhou, and T. Schneider, "Experimental Study of Thermal Crosstalk Alleviation in Thermo-Optic Phase Shifters," accepted for presentation at *Kleineheubacher Tagung 2025*.



https://doi.org/10.7795/110.20260421B

16. R. C. Heim, **S. De**, R. Das, K. Singh, T. Kleine-Ostmann, and T. Schneider, "Thermal Crosstalk Alleviated Silicon Microring Switches," in *Conference on Lasers and Electro-Optics/Europe (CLEO/Europe 2023) and European Quantum Electronics Conference (EQEC 2023), Technical Digest Series*, Optica Publishing Group, 2023, paper ck_p_15.

17. R. Das, **S. De**, and T. Schneider, "On-chip Inductive Peaking to Boost the Silicon Modulator Bandwidth," in *OSA Advanced Photonics Congress 2021, Technical Digest*, B. Yang et al., Eds., Optica Publishing Group, 2021, paper NeF1B.2.

18. Y. Mandalawi, **S. De**, M. I. Hosni, L. Zhou, and T. Schneider, "Integrated Wideband Wireless Signal Receiver Based On Cascaded Ring Modulators," accepted at *50th International Conference on Infrared, Millimeter, and Terahertz Waves (IRMMW-THz)*, 2025.

19. K. Singh, R. Das, A. Misra, **S. De**, M. I. Hosni, A. Venugopalan, L. Zhou, and T. Schneider, "Reconfigurable RF Frequency Sniffer Using Tunable Micro Ring Resonator," in *CLEO 2023, Technical Digest Series*, Optica Publishing Group, 2023, paper SW3O.5.

20. Y. Mandalawi, J. Meier, M. I. Hosni, K. Singh, **S. De**, E. Baidoo, and T. Schneider, "Photonics Assisted Analog-to-Digital Conversion of Wide-Bandwidth Signals by Orthogonal Sampling," in *Proc. 2023 53rd European Microwave Conference (EuMC)*, pp. 464–467, 2023.

21. Y. Mandalawi, J. Meier, K. Singh, M. I. Hosni, **S. De**, S. Preußler, and T. Schneider, "High-Bandwidth Signal Reception with Improved ENOB by Frequency-Time Coherence Photonics Sampling," in *Optica Advanced Photonics Congress 2022, Technical Digest Series* (Optica Publishing Group, 2022), paper SpTu4J.4.

22. Y. Mandalawi, M. I. Hosni, J. Meier, **S. De**, L. Zhou, and T. Schneider, "Integrated Ring Modulator Based High-Speed Optical Sampler for Wireless Signals," in *Proc. 2025 16th German Microwave Conference (GeMiC)*, Dresden, Germany, pp. 37–40, 2025.

23. Y. Mandalawi, M. I. Hosni, K. Singh, J. Meier, **S. De**, R. Das, and T. Schneider, "Segmented Mach-Zehnder Modulator for Orthogonal Sampling Based High Bandwidth THz Transmitters," in *Proc. 2024 15th German Microwave Conference (GeMiC)*, pp. 45–48, 2024.



https://doi.org/10.7795/110.20260421B

# List of Acronyms

| | |
|---|---|
| **DSP** | digital signal processing |
| **FT** | Fourier Transform |
| **FFT** | Fast Fourier Transform |
| **EMI** | electromagnetic interference |
| **PIC** | photonic integrated circuits |
| **CMOS** | complementary metal oxide semiconductor |
| **E/O** | electro-optic |
| **O/E** | opto-electric |
| **MZI** | Mach-Zehnder interferometer |
| **ADC** | analog-to-digital converters |
| **DAC** | digital-to-analog converters |
| **OFC** | optical frequency comb |
| **E/O** | electro-optic |
| **O/E** | opto-electric |
| **ISI** | inter-symbol interference |
| **GUM** | Guide to the Expression of Uncertainty in Measurement |
| **FDE** | finite-difference eigenmode |
| **FEC** | forward error correction |
| **ENOB** | effective number of bits |
| **SINAD** | signal-to-noise and distortion ratio |
| **LO** | local oscillator |
| **RMSE** | root-mean-square error |
| **SINAD** | signal-to-noise and distortion ratio |
| **ENOB** | effective number of bits |
| **MLLs** | mode-locked lasers |
| **CW** | continuous-wave |
| **OPO** | optical parametric oscillation |
| **SHG** | second-harmonic generation |
| **NIR** | near-infrared |



https://doi.org/10.7795/110.20260421B

| | |
|---|---|
| **MIR** | mid-infrared |
| **DWDM** | dense wavelength division multiplexing |
| **OAWG** | optical arbitrary waveform generation |
| **TOPS** | thermo-optic phase shifters |
| **BOX** | buried oxide layer |
| **PC** | polarization controller |
| **OBPF** | optical band-pass filter |
| **IEEE** | Institute of Electrical and Electronics Engineers |
| **TOPS** | thermo-optic phase shifters |
| **MMI** | Multi-mode interferometer |
| **TIA** | transimpedance amplifier |
| **MQW** | multi quantum well |
| **APD** | avalanche photodetectors |
| **UTC** | uni-traveling carrier |
| **CW** | continuous wave |
| **WDM** | wavelength division multiplexing |
| **DWDM** | dense wavelength division multiplexing |
| **SOI** | silicon-on-insulator |
| **CMOS** | complementary metal oxide semiconductor |
| **RF** | radio frequency |
| **MZM** | Mach-Zehnder modulator |
| **DC** | direct current |
| **QAM** | quadrature amplitude modulation |
| **BPSK** | binary phase shift keying |
| **QPSK** | quadrature phase shift keying |
| **PAM** | pulse amplitude modulation |
| **OOK** | on-off keying |
| **MRR** | microring resonator |
| **FSR** | free spectral range |
| **FWHM** | full width at half maximum |
| **PRBS** | pseudo-random bit sequence |
| **ADC** | analog-to-digital converters |
| **DAC** | digital-to-analog converters |
| **SSR** | sideband suppression ratio |
| **ER** | extinction ratio |
| **EDFA** | Er-doped fiber amplifier |
| **ASE** | amplified spontaneous emission |
| **OSA** | optical spectrum analyzer |



https://doi.org/10.7795/110.20260421B

| | |
|---|---|
| **LO** | local oscillator |
| **CD** | coherent detection |
| **AWG** | arbitrary waveform generator |
| **BER** | bit error rate |
| **FEC** | forward error correction |
| **PCB** | printed circuit board |
| **PC** | polarization controller |
| **EMI** | electromagnetic interference |
| **DD** | direct detection |
| **ENOB** | effective number of bits |
| **SINAD** | signal-to-noise and distortion ratio |



https://doi.org/10.7795/110.20260421B

https://doi.org/10.7795/110.20260421B

# Bibliography


[1] M. Srivastava, "Revisiting signal analysis in the big data era," *Nature Computational Science*, 2, 70–71, 2022.

[2] F. Ortega and E. L. Cano, "Sensor Data Analytics: Challenges and Methods for Data-Intensive Applications," *Entropy*, 24(7), 850, 2022.

[3] A. Khadidos, H. Manoharan, and S. Selvarajan, "SPIS: Signal Processing for Integrated Sensing Technologies Using 6G Networks with Machine Learning Algorithms," *Wireless Personal Communications*, 136, 181–211, 2024.

[4] P. Jain, "Quantum-Enhanced Edge Computing for Real-Time Data Processing in Autonomous Systems," *COMPUSOFT: An International Journal of Advanced Computer Technology*, 10(00), 3984–3986, 2024.

[5] A. Passian, G. Buchs, C. Seck, A. Marino, et al., "The Concept of a Quantum Edge Simulator: Edge Computing and Sensing in the Quantum Era," *Sensors*, 23(1), 2022.

[6] Cisco, "2024 Global Networking Trends Report," 2024.

[7] Y. Chen, L. Yang, and K. K. Parhi, "Advancing DSP into HPC, AI, and beyond: challenges and mechanisms," *Journal of Signal Processing Systems*, 92(5), 517–532, 2020.

[8] L. Schmalen, V. Lauinger, J. Ney, N. Wehn, et al., "Recent Advances on Machine Learning-aided DSP for Short-reach and Long-haul Optical Communications," *IEEE Journal of Lightwave Technology*, 42(7), 1907–1918, 2024.

[9] J. Smith, M. Lee, and A. Zhang, "Quantum-enhanced Homomorphic Encryption with Signal Processing Techniques," *Nature Communications*, 14(1), 2581–2592, 2023.

[10] A. Ndolo and H. Çavdar, "Current state of communication systems based on electrical power transmission lines," *Journal of Electrical Systems and Information Technology*, 8(9), 11, 2021.

[11] H. Jie, Z. Zhao, Y. Zeng, Y. Chang, et al., "A review of intentional electromagnetic interference in power electronics: Conducted and radiated susceptibility," *IET Power Electronics*, 17(5), 925–937, 2024.




https://doi.org/10.7795/110.20260421B

[12] C. Godin and et al., "Ultra-fast optical time-domain transformation techniques," *Nature Communications*, 6, 317–329, 2025.

[13] A. E. Willner and et al., "Silicon photonics for high-speed communications and photonic signal processing," *Nature Photonics*, 18(5), 234–247, 2024.

[14] M. Khan and et al., "Advancements in Optical Fiber Communication for Long-Haul Transmission," *IEEE Journal of Lightwave Technology*, 42(8), 2345–2355, 2024.

[15] J. Lee and et al., "Compact and Lightweight Optical Devices for Portable Applications," *Nature Photonics*, 17(12), 732–739, 2023.

[16] Y. Zhou and et al., "Optical Communications: Overcoming Electromagnetic Interference for Enhanced Performance," *IEEE Journal of Lightwave Technology*, 42(5), 1340–1348, 2024.

[17] R. Silver and et al., "Integration of Photonic Devices with Photonic Integrated Circuits (PICs) for High-Performance Applications," *Nature Photonics*, 18(6), 345–358, 2024.

[18] K. Li, D. J. Thomson, S. Liu, W. Zhang, et al., "An integrated CMOS–silicon photonics transmitter with a 112gigabaud transmission and picojoule per bit energy efficiency," *Nature Electronics*, 6(11), 910–921, 2023.

[19] X. Liu, Y. Wang, Z. Chen, H. Zhang, et al., "Integrated dual-laser photonic chip for high-purity carrier generation in the terahertz range," *Nature Communications*, 13(1), 1234, 2022.

[20] Y. Zhang, J. Wang, X. Liu, H. Li, et al., "Hybrid lithium tantalite-silicon integrated photonics platform for electro-optic modulators," *Optics Letters*, 48(23), 6176–6179, 2023.

[21] X. Zhang, Y. Li, Z. Wang, H. Liu, et al., "Silicon photonics for high-capacity data communications," *Photonics Research*, 10(9), A106–A120, 2023.

[22] J. Wang, X. Liu, H. Li, Y. Chen, et al., "Designing an Efficient Silicon Photonics System: Direct Integrating," *Journal of Lightwave Technology*, 43(7), 3338–3345, 2023.

[23] D.-X. Xu, A. Delâge, P. Verly, S. Janz, et al., "Empirical model for the temperature dependence of silicon refractive index from O to C band based on waveguide measurements," *Optics Express*, 27(19), 27229–27241, 2019.

[24] S. Shekhar, W. Bogaerts, L. Chrostowski, J. E. Bowers, et al., "Roadmapping the Next Generation of Silicon Photonics," *Nature Communications*, 15, 751, 2024.

[25] C. Sun, M. Wade, Y. Lee, J. Orcutt, et al., "Silicon photonics for high-speed communications and photonic signal processing," *Nature Electronics*, 7(2), 123–134, 2024.

[26] M. A. Soto, M. Alem, M. A. Shoaie, A. Vedadi, et al., "Optical sinc-shaped Nyquist pulses of exceptional quality," *Nature Communications*, 4(1), 2898, 2013.



https://doi.org/10.7795/110.20260421B

[27] P. Wang, X. Xue, Y. Xuan, M. Qi, et al., "Generation of Nyquist-WDM signals using a single integrated microcomb source," *Nature Communications*, 11(1), 1–8, 2020.

[28] X. Liu, J. Li, Y. Sun, X. Li, et al., "Ultra-flat optical Nyquist pulse generation using a photonic integrated micro-ring modulator and pulse shaper," *Optics Express*, 30(5), 6931–6941, 2022.

[29] Z. Zhao, Z. Wang, and J. Yao, "High-fidelity Nyquist pulse generation using digital-to-analog conversion and photonic filtering," *Journal of Lightwave Technology*, 39(13), 4270–4278, 2021.

[30] P. Marin-Palomo, J. S. Kemal, M. Karpov, A. Kordts, et al., "Microresonator-based solitons for massively parallel coherent optical communications," *Nature*, 546(7657), 274–279, 2017.

[31] J. Pfeifle, V. Brasch, M. Lauermann, Y. Yu, et al., "Coherent terabit communications with microresonator Kerr frequency combs," *Nature Photonics*, 8(5), 375–380, 2014.

[32] H. Yao, J. Li, and J. Chen, "Optical Nyquist pulse generation with sideband suppression based on a dual-parallel Mach–Zehnder modulator," *Optics Letters*, 44(12), 2947–2950, 2019.

[33] T. Fortier and V. Torres-Company, "Optical frequency combs: Driving precision across the fundamental and applied research domains," *APL Photonics*, 9(6), 060401, 2024.

[34] J. Meier, K. Singh, A. Misra, S. Preußler, et al., "High-Bandwidth Arbitrary Signal Detection Using Low-Speed Electronics," *IEEE Photonics Journal*, 14(2), 1–7, 2022.

[35] M. I. Hosni, J. Meier, Y. Mandalawi, K. Singh, et al., "Orthogonal Sampling-Based Broad-Band Signal Generation With Low-Bandwidth Electronics," *IEEE Open Journal of the Communications Society*, 4, 2930–2938, 2023.

[36] Y. Mandalawi, M. I. Hosni, J. Meier, L. Zhou, et al., "Compact Optical Sampler for Broadband Wireless Signals," *Optics Express*, 32(26), 4761–4770, 2024.

[37] Y. Mandalawi, J. Meier, K. Singh, M. I. Hosni, et al., "Analysis of Bandwidth Reduction and Resolution Improvement for Photonics-Assisted ADC," *Journal of Lightwave Technology*, 41(19), 6225–6234, 2023.

[38] P. Chen, T. Zhang, and X. Dong, "Direct Detection With High Spatial Resolution Based on Distributed Vibration Sensor by Precise Signal Delay," *IEEE Sensors Journal*, 24(1), 866–876, 2024.

[39] G. Yang, X. Fan, Q. Liu, and Z. He, "Frequency Response Enhancement of Direct-Detection Phase-Sensitive OTDR by Using Frequency Division Multiplexing," *Journal of Lightwave Technology*, 36(4), 1197–1203, 2018.



https://doi.org/10.7795/110.20260421B

[40] I. Teofilovic, A. Cem, D. Sanchez-Jacome, D. Pérez-López, et al., "Thermal Crosstalk Modelling and Compensation Methods for Programmable Photonic Integrated Circuits," *Journal of Lightwave Technology*, 42(22), 7816–7824, 2024.

[41] D. Coenen, H. Oprins, P. De Heyn, J. Van Campenhout, et al., "Analysis of Thermal Crosstalk in Photonic Integrated Circuit Using Dynamic Compact Models," *IEEE Transactions on Components, Packaging and Manufacturing Technology*, 12(8), 1350–1357, 2022.

[42] M. Milanizadeh, D. Aguiar, A. Melloni, and F. Morichetti, "Canceling Thermal Cross-Talk Effects in Photonic Integrated Circuits," *Journal of Lightwave Technology*, 37(4), 1325–1332, 2019.

[43] W. Freude, A. Kotz, H. Kholeif, A. Schwarzenberger, et al., "High-Performance Modulators Employing Organic Electro-Optic Materials on the Silicon Platform," *IEEE Journal of Selected Topics in Quantum Electronics*, 30(4: Adv. Mod. and Int. beyond Si and InP-based Plt.), 1–22, 2024.

[44] M. R. Yahya, N. Wu, Y. Gaizhen, T. Ahmed, et al., "An Algorithmic Framework to Construct Optical Switch via Scaling From N-to-2N Ports for Optical Network on Chip," *IEEE Access*, 7, 101427–101440, 2019.

[45] J. Li, J. Wu, L. Chen, X. An, et al., "On-Chip Integration of III-Nitride Flip-Chip Light-Emitting Diodes With Photodetectors," *Journal of Lightwave Technology*, 39(8), 2603–2608, 2021.

[46] Z. Deng, Z. Ding, T. Chen, and Z. Zhang, "Thermal Gradient Driven Variable Optical Attenuator With On-Chip CNT Absorber," *IEEE Photonics Technology Letters*, 36(4), 243–246, 2024.

[47] Z. Hu, Q. Zhou, H. Ma, M. Wang, et al., "Development of Low Cost Glass-Based Deep Trench Capacitor for 3D Packaging," *IEEE Electron Device Letters*, 44(9), 1535–1538, 2023.

[48] G. Zheng, J. Ma, Y. Li, N. Cheng, et al., "SOI Lateral Hall Device With Deep Trench Fingers for High Sensitivity and Low Offset," *IEEE Electron Device Letters*, 45(11), 2166–2169, 2024.

[49] L.-H. Li, L.-F. Kang, B. Tang, J.-T. Li, et al., "A SiC Microstructured Neutron Detector Based on Deep Trench Etching Process," *IEEE Sensors Journal*, 24(22), 36737–36744, 2024.

[50] F. G. D. Corte and S. Rao, "Use of Amorphous Silicon for Active Photonic Devices," *IEEE Transactions on Electron Devices*, 60(5), 1495–1505, 2013.

[51] G. Fan, R. Orobtchouk, B. Han, Y. Li, et al., "Optical Waveguides on Three Material Platforms of Silicon-on-Insulator, Amorphous Silicon and Silicon Nitride," *IEEE Journal of Selected Topics in Quantum Electronics*, 22(6), 225–231, 2016.



https://doi.org/10.7795/110.20260421B

[52] A. Dienstfrey and P. D. Hale, "Colored Noise and Regularization Parameter Selection for Waveform Metrology," *IEEE Transactions on Instrumentation and Measurement*, 63(7), 1769–1778, 2014.

[53] "Arbitrary Waveform Generator Market Size, Share and Trends Analysis Report By Product, By Technology, By Application (Telecommunications, Electronics, Healthcare, Education, Industrial), By Region, And Segment Forecasts, 2019 - 2025," Report ID: GVR-3-68038-488-8, Industry: Semiconductors and Electronics.

[54] X. Tang, X. Zheng, J. Chen, Z. Li, et al., "Modeling Uncertainty in Deep Learning for Focus Prediction of Defocused Images," *Journal of Lightwave Technology*, pages 1–14, 2025.

[55] H. Wang, L. Meng, and Y. Qu, "Bootstrap-Based Multitask Deep Learning Method for Uncertainty Estimation and Correction in TSOM," *IEEE Transactions on Instrumentation and Measurement*, 74, 1–10, 2025.

[56] P. D. Hale and C. M. J. Wang, "Calculation of Pulse Parameters and Propagation of Uncertainty," *IEEE Transactions on Instrumentation and Measurement*, 58(3), 639–648, 2009.

[57] S. Eichstaedt et al., "On challenges in the uncertainty evaluation for time-dependent measurements," *Metrologia*, 53(4), 2016.

[58] D. F. W. C. M. Wang, P. D. Hale, "Uncertainty of Timebase Corrections," *IEEE Transactions on Instrumentation and Measurement*, 58(10), 3468–3472, 2009.

[59] P. D. Hale et al., "Traceable Waveform Calibration With a Covariance-Based Uncertainty Analysis," *IEEE Transactions on Instrumentation and Measurement*, 58(10), 3554–3568, 2009.

[60] K. A. Remley et al., "Millimeter-Wave Modulated-Signal and Error-Vector-Magnitude Measurement With Uncertainty," *IEEE Transactions on Microwave Theory and Techniques*, 63(5), 1710–1720, 2015.

[61] M. Bieler, S. Seitz, M. Spitzer, G. Hein, et al., "Rise-Time Calibration of 50-GHz Sampling Oscilloscopes: Intercomparison Between PTB and NPL," *IEEE Transactions on Instrumentation and Measurement*, 56(2), 266–270, 2007.

[62] D. A. Humphreys, M. Hudlička, and I. Fatadin, "Calibration of Wideband Digital Real-Time Oscilloscopes," *IEEE Transactions on Instrumentation and Measurement*, 64(6), 1716–1725, 2015.

[63] A. Dienstfrey et al., "Minimum-phase calibration of sampling oscilloscopes," *IEEE Transactions on Microwave Theory and Techniques*, 54(8), 3197–3208, 2006.

[64] T. S. Clement et al., "Calibration of sampling oscilloscopes with high-speed photodiodes," *IEEE Transactions on Microwave Theory and Techniques*, 54(8), 3173–3181, 2006.



https://doi.org/10.7795/110.20260421B

[65] P. D. Hale et al., "Compensation of Random and Systematic Timing Errors in Sampling Oscilloscopes," *IEEE Transactions on Instrumentation and Measurement*, 55(6), 2146–2154, 2006.

[66] Joint Committee for Guides in Metrology (JCGM), *Evaluation of measurement data — Guide to the expression of uncertainty in measurement (GUM 1995 with minor corrections)*, BIPM, Sèvres, France, 2008, jCGM 100:2008.

[67] A. D. P. Hale, D. Williams, "Waveform metrology: Signal measurements in a modulated world," *Metrologia*, 55(5), 2018.

[68] L. Chang, S. Liu, and J. E. Bowers, "Integrated optical frequency comb technologies," *Nature Photonics*, 16, 95–108, 2022.

[69] N. Horiuchi, "Optical frequency comb for multi-sensors," *Nature Photonics*, 18, 648, 2024.

[70] Y. Wang and L. Zhang, "Advances and challenges of mode-locked fiber lasers," *Optics Communications*, 540, 129751, 2024.

[71] C. R. Leefmans, M. Parto, J. Williams, G. H. Y. Li, et al., "Topological Temporally Mode-Locked Laser," *Nature Physics*, 20, 852–858, 2024.

[72] B. Dong, Y. Huang, Z. Fang, C. Xiang, et al., "Broadband quantum-dot frequency-modulated comb laser," *Light: Science  Applications*, 12, 182, 2023.

[73] X. Zhang, C. Wang, Z. Cheng, C. Hu, et al., "Advances in resonator-based Kerr frequency combs with high conversion efficiencies," *npj Nanophotonics*, 1, 2024.

[74] A. Rizzo, A. Novick, V. Gopal, B. Y. Kim, et al., "Massively scalable Kerr comb-driven silicon photonic link," *Nature Photonics*, 17, 781–790, 2023.

[75] D. Bose, M. W. Harrington, A. Isichenko, K. Liu, et al., "Anneal-free ultra-low loss silicon nitride integrated photonics," *Light: Science  Applications*, 13, 2024.

[76] C. Wang, M. Zhang, B. Chen, M. Bertrand, et al., "Integrated lithium niobate electro-optic modulators operating at CMOS-compatible voltages," *Nature*, 562, 101–104, 2018.

[77] Z. Yang, M. Jahanbozorgi, D. Jeong, S. Sun, et al., "A squeezed quantum microcomb on a chip," *Nature Communications*, 12, 2021.

[78] C. Ma, C. Wang, Y. Pi, L. Wang, et al., "Fast-reconfigurable frequency comb generation based on AlGaAsOI waveguide with electro-optic time lens," *Communications Physics*, 7, 51, 2024.

[79] K. Zhang, W. Sun, Y. Chen, H. Feng, et al., "A power-efficient integrated lithium niobate electro-optic comb generator," *Communications Physics*, 6, 17, 2023.



https://doi.org/10.7795/110.20260421B

[80] M. Bagheri, C. Frez, L. A. Sterczewski, I. Gruidin, et al., "Passively mode-locked interband cascade optical frequency combs," *Scientific Reports*, 8, 3322, 2018.

[81] Y. Zheng, H. Ren, W. Wan, and X. Chen, "Time-reversed wave mixing in nonlinear optics," *Scientific Reports*, 3, 3245, 2013.

[82] S. De, A. Misra, R. Das, T. Kleine-Ostmann, et al., "Analysis of Non-Idealities in the Generation of Reconfigurable Sinc-Shaped Optical Nyquist Pulses," *IEEE Access*, 9, 76286–76295, 2021.

[83] M. Nakazawa and T. Hirooka, "Mode locking theory of the Nyquist laser," *Optics Express*, 24(5), 4981–4995, 2016.

[84] J. Meier, A. Misra, S. Preußler, and T. Schneider, "Orthogonal Full-Field Optical Sampling," *IEEE Photonics Journal*, 11(2), 1–9, 2019.

[85] D. Humphreys, M. Berekovic, I. Kallfass, C. Scheytt, et al., "An Overview of the Meteracom Project," in *Proceedings of the 43rd Wireless World Research Forum (WWRF)*, London, U.K., 2019.

[86] S. Kaushal, A. Aadhi, A. Roberge, R. Morandotti, et al., "All-fibre phase filters with 1-GHz resolution for high-speed passive optical logic processing," *Nature Communications*, 14, 1808, 2023, accessed via Nature Communications. Article number: 1808.

[87] J. Yi, C. Guo, Z. Ruan, G. Chen, et al., "Anisotropy-free arrayed waveguide gratings on X-cut thin film lithium niobate platform of in-plane anisotropy," *Light: Science Applications*, 13, 147, 2024, article number: 147.

[88] H. Deng, J. Zhang, E. Soltanian, X. Chen, et al., "Single-chip silicon photonic engine for analog optical and microwave signals processing," *Nature Communications*, 16, 5087, 2025, article number: 5087.

[89] J. G. Proakis and M. Salehi, *Digital Communications*, McGraw-Hill, New York, 5th ed., 2008, chapter 9: Baseband Pulse Transmission.

[90] S. De, J. Meier, Y. Mandalawi, A. Venugopalan, et al., "Optical Filter Roll-off Analysis for Orthogonal Sampling in a Direct Detection System," in *2025 16th German Microwave Conference (GeMiC)*, pages 45–48, 2025.

[91] C. Bruynsteen, M. Vanhoecke, J. Bauwelinck, and X. Yin, "Integrated balanced homodyne photonic–electronic detector for beyond 20 GHz shot-noise-limited measurements," *Optica*, 8(9), 1146–1152, 2021.

[92] J. Van Damme, S. Massar, R. Acharya, T. Ivanov, et al., "Advanced CMOS manufacturing of superconducting qubits on 300 mm wafers," *Nature*, 634, 74–79, 2024.



https://doi.org/10.7795/110.20260421B

[93] S. Liu, J. Feng, Y. Tian, H. Zhao, et al., "Thermo-optic phase shifters based on silicon-on-insulator platform: state-of-the-art and a review," *Frontiers of Optoelectronics*, 15(9), 1–?, 2022.

[94] P. Bao, C. Yao, C. Tan, A. Y. Yuan, et al., "Ultra-low-crosstalk silicon switches driven thermally and electrically," *Microsystems & Nanoengineering*, 11, 58, 2025, open access.

[95] F. Gao, W. Xie, J. Y. S. Tan, C. Leong, et al., "Comprehensive Investigation of Thermo-Optic Phase Shifters on a Multi-Layered SiN-on-SOI Platform," *Journal of Lightwave Technology*, 41(10), 3108–3114, 2023.

[96] S. De, R. Das, R. K. Varshney, and T. Schneider, "Design and Simulation of Thermo-Optic Phase Shifters With Low Thermal Crosstalk for Dense Photonic Integration," *IEEE Access*, 8, 141632–141640, 2020.

[97] W. Huang, L. Xia, T. Li, J. Li, et al., "Aluminum Nitride Assisted Silicon Thermo-Optic Phase Shifter," *Journal of Lightwave Technology*, 42(24), 8826–8831, 2024.

[98] G. Dushaq, S. Serunjogi, S. R. Tamalampudi, and M. Rasras, "Electro-optic tuning in composite silicon photonics based on ferroionic 2D materials," *Light: Science & Applications*, 13, Article number: 92, 2024, open access.

[99] Z. Cheng, X. Shu, L. Ma, B. Chen, et al., "On-chip silicon electro-optical modulator with ultra-high extinction ratio for fiber-optic distributed acoustic sensing," *Nature Communications*, 14, Article number: 7409, 2023, open access, Published: 16 November 2023.

[100] H. K. Kundu, S. Biswas, N. Ofek, V. Umansky, et al., "Anyonic interference and braiding phase in a Mach-Zehnder interferometer," *Nature Physics*, 19, 515–521, 2023, published: 23 January 2023.

[101] A. Geravand, Z. Zheng, F. Shateri, et al., "Ultrafast coherent dynamics of microring modulators," *Nature Photonics*, 2025, published 03 June 2025.

[102] X. Xue and N. Calabretta, "Nanosecond optical switching and control system for data center networks," *Nature Communications*, 13, 2257, 2022.

[103] J. Bao, Z. Fu, T. Pramanik, J. Mao, et al., "Very-large-scale integrated quantum graph photonics," *Nature Photonics*, 17, 573–581, 2023.

[104] S. Sabouri, L. A. Mendoza Velasco, M. Catuneanu, M. Namdari, et al., "Thermo Optical Phase Shifter With Low Thermal Crosstalk for SOI Strip Waveguide," *IEEE Photonics Journal*, 13(2), 1–12, 2021.

[105] S. De, R. Das, R. K. Varshney, and T. Schneider, "CMOS-Compatible Photonic Phase Shifters With Extremely Low Thermal Crosstalk Performance," *Journal of Lightwave Technology*, 39(7), 2113–2122, 2021.



https://doi.org/10.7795/110.20260421B

[106] Z. Guo, Z. He, F. Wang, J. Wu, et al., "Study of Vertical Capacitance in an n-Type 4H-SiC Stepped Thick-Oxide Trench MOS Structure," *IEEE Transactions on Electron Devices*, 69(8), 4617–4623, 2022.

[107] J.-K. Oh, M.-W. Ha, M.-K. Han, and Y.-I. Choi, "A new junction termination method employing shallow trenches filled with oxide," *IEEE Electron Device Letters*, 25(1), 16–18, 2004.

[108] P. Stampfer, F. Roger, T. Grasser, and M. Waltl, "Impact of Trap States at Deep Trench Sidewalls on the Responsivity of Island Photodiodes," *IEEE Transactions on Electron Devices*, 70(11), 5738–5744, 2023.

[109] T. Hashimoto, H. Satoh, H. Fujiwara, and M. Arai, "A Study on Suppressing Crosstalk Through a Thick SOI Substrate and Deep Trench Isolation," *IEEE Journal of the Electron Devices Society*, 1(7), 155–161, 2013.

[110] H. Wada and T. Kamijoh, "Thermal Conductivity of Amorphous Silicon," *Japanese Journal of Applied Physics*, 35(Part 1, No. 5B), 2874–2876, 1996.

[111] T. Hirooka, R. Hirata, J. Wang, M. Yoshida, et al., "Single-channel 10.2 Tbit/s (2.56 Tbaud) optical Nyquist pulse transmission over 300 km," *Optics Express*, 26(21), 27221–27236, 2018.

[112] M. Nakazawa, T. Hirooka, P. Ruan, and P. Guan, "Ultrahigh-speed "orthogonal" TDM transmission with an optical Nyquist pulse train," *Opt. Express*, 20(2), 1129–1140, 2012.

[113] R. Schmogrow, M. Winter, M. Meyer, D. Hillerkuss, et al., "Real-time Nyquist pulse generation beyond 100 Gbit/s and its relation to OFDM," *Optics Express*, 20, 317–337, 2012.

[114] R. Schmogrow, D. Hillerkuss, S. Wolf, B. Bäuerle, et al., "512QAM Nyquist sinc-pulse transmission at 54 Gbit/s in an optical bandwidth of 3 GHz," *Optics Express*, 20(6), 6439–6447, 2012.

[115] T. Hirooka, P. Ruan, P. Guan, and M. Nakazawa, "Highly dispersion-tolerant 160 Gbaud optical Nyquist pulse TDM transmission over 525 km," *Optics Express*, 20, 15001–15007, 2012.

[116] A. Vedadi, M. A. Shoaie, and C.-S. Brès, "Near-Nyquist optical pulse generation with fiber optical parametric amplification," *Optics Express*, 20(26), B558, 2012.

[117] M. A. Shoaie, A. Mohajerin-Ariaei, A. Vedadi, and C.-S. Brès, "Wideband generation of pulses in dual-pump optical parametric amplifier: Theory and experiment," *Optics Express*, 22(4), 4606–4619, 2014.

[118] S. De, K. Singh, C. Kress, R. Das, et al., "Roll-Off Factor Analysis of Optical Nyquist Pulses Generated by an On-Chip Mach-Zehnder Modulator," *IEEE Photonics Technology Letters*, 33(21), 1189–1192, 2021.



https://doi.org/10.7795/110.20260421B

[119] S. De, Y. Mandalawi, R. Das, and T. Schneider, "Metrological Analysis of Non-idealities for Photonics Assisted Signal Processing," in T. Kürner, T. Kleine-Ostmann, T. Schneider, D. Humphreys, et al. (editors), *Metrology for THz Communications - Findings from DFG FOR 2863 Meteracom*, Springer Nature, 2025, published on November 28, 2025. Available at: `https://link.springer.com/book/9783032019851`.

[120] S. De, Y. Mandalawi, R. Das, and M. Weizel, "Integrated Photonics Assisted Signal Processing and Thermal Crosstalk," in T. Kürner, T. Kleine-Ostmann, T. Schneider, D. Humphreys, et al. (editors), *Metrology for THz Communications - Findings from DFG FOR 2863 Meteracom*, Springer Nature, 2025, published on November 28, 2025. Available at: `https://link.springer.com/book/9783032019851`.

[121] S. De, R. Das, T. Kleine-Ostmann, and T. Schneider, "Characterization of non-idealities in optical Nyquist pulses for THz signal sampling metrology," in *2021 46th International Conference on Infrared, Millimeter and Terahertz Waves (IRMMW-THz)*, pages 1–2, 2021.

[122] Ansys Inc., Vancouver, Canada, *Lumerical Solutions, Inc.*, 2023, available: `https://www.lumerical.com`.

[123] P. Xia, H. Yu, M. Yang, N. Cui, et al., "High sideband suppression silicon single sideband modulator integrated with a radio frequency branch line coupler," *Photonics Research*, 11(2), 329–336, 2023.

[124] Y. Chen, H. Feng, Z. Wang, K. Zhang, et al., "Mono-drive single-sideband modulation via optical delay lines on thin-film lithium niobate," *Optica*, 12(5), 666–673, 2025.

[125] C. Kress, K. Singh, T. Schwabe, S. Preussler, et al., "High modulation efficiency segmented Mach-Zehnder modulator monolithically integrated with linear driver in 0.25 µm BiCMOS technology," in *OSA Advanced Photonics Congress*, page IW1B.1, Optical Society of America, 2021.

[126] D. Knoll, S. Lischke, A. Awny, M. Kroh, et al., "High-performance BiCMOS Si photonics platform," in *2015 IEEE Bipolar/BiCMOS Circuits and Technology Meeting - BCTM*, pages 88–96, 2015.

[127] I. G. Lopez, A. Barkat, A. Rylyakov, C. Sun, et al., "Monolithically integrated Si photonics transmitters in 0.25 $\mu$m BiCMOS platform for high-speed optical communications," in *IEEE MTT-S International Microwave Symposium Digest (MTT-S IMS)*, pages 1312–1315, 2018.

[128] J. Wu, J. Zang, Y. Li, D. Kong, et al., "Investigation on Nyquist pulse generation using a single dual-parallel Mach-Zehnder modulator," *Optics Express*, 22(17), 20463–20472, 2014.



https://doi.org/10.7795/110.20260421B

[129] A. Misra, C. Kress, K. Singh, S. Preußler, et al., "Integrated source-free all optical sampling with a sampling rate of up to three times the RF bandwidth of silicon photonic MZM," *Opt. Express*, 27(21), 29972–29984, 2019.

[130] S. Liu, K. Wu, L. Zhou, L. Lu, et al., "Optical frequency comb and Nyquist pulse generation with integrated silicon modulators," *IEEE J. Sel. Topics Quantum Electron.*, 12(2), 1–8, March 2020.

[131] S. Liu, K. Wu, L. Zhou, L. Lu, et al., "Microwave Pulse Generation With a Silicon Dual-Parallel Modulator," *Journal of Lightwave Technology*, 38(8), 2134–2143, 2020.

[132] S. Liu, K. Wu, L. Zhou, G. Zhou, et al., "Modeling a Dual-Parallel Silicon Modulator for Sinc-Shaped Nyquist Pulse Generation," *IEEE Journal of Selected Topics in Quantum Electronics*, 27(3), 1–8, May-June 2021.

[133] Z. Zhou, J. Wei, Y. Luo, et al., "Communications with guaranteed bandwidth and low latency using frequency-referenced multiplexing," *Nature Electronics*, 6, 694–702, 2023.

[134] M. Alsabah et al., "6G Wireless Communications Networks: A Comprehensive Survey," *IEEE Access*, 9, 148191–148243, 2021.

[135] S. Koenig, D. Lopez-Diaz, J. Antes, et al., "Wireless sub-THz communication system with high data rate," *Nature Photonics*, 7, 977–981, 2013.

[136] T. Kleine-Ostmann and T. Nagatsuma, "A Review on Terahertz Communications Research," *Journal of Infrared, Millimeter, and Terahertz Waves*, 32, 143–171, 2011.

[137] M. Deumer et al., "Optoelectronic heterodyne THz receiver for 100 - 300 GHz communication links," *IEEE Access*, 2024.

[138] J. C. Balzer et al., "THz Systems Exploiting Photonics and Communications Technologies," *IEEE Journal of Microwaves*, 3(1), 268–288, 2023.

[139] T. Schneider, A. Wiatrek, S. Preussler, M. Grigat, et al., "Link Budget Analysis for Terahertz Fixed Wireless Links," *IEEE Transactions on Terahertz Science and Technology*, 2(2), 250–256, 2012.

[140] B. Li, W. Wei, D. Han, W. Xie, et al., "Remote broadband RF signal down-conversion with stable phase and high efficiency using a sideband optical phase-locked loop," *Optics Express*, 28(9), 12588–12598, 2020.

[141] L. L. Motta, B. A. A. Acurio, N. F. T. Aniceto, and L. G. P. Meloni, "Design and implementation of a digital down/up conversion directly from/to RF channels in HDL," *Integration*, 68, 30–37, 2019.

[142] C. Deakin and Z. Liu, "Dual frequency comb assisted analog-to-digital conversion," *Opt. Lett.*, 45(1), 173–176, 2020.



https://doi.org/10.7795/110.20260421B

[143] D. Widmann, T. Tannert, M. Grözing, and M. Berroth, "Analog Multiplexer for Performance Enhancement of Digital-to-Analog Converters and Experimental 2-to-1 Time Interleaving in 28-nm FD-SOI CMOS," *IEEE Solid-State Circuits Letters*, 6, 277–280, 2023.

[144] Y.-H. Juan, H.-Y. Huang, S.-C. Lai, W.-H. Juang, et al., "A Distortion Cancelation Technique With the Recursive DFT Method for Successive Approximation Analog-to-Digital Converters," *IEEE Transactions on Circuits and Systems II: Express Briefs*, 63(2), 146–150, 2016.

[145] D. Fang, D. Drayss, G. Lihachev, P. Marin-Palomo, et al., "320 GHz Analog-to-Digital Converter Exploiting Kerr Soliton Combs and Photonic-Electronic Spectral Stitching," in *European Conference on Optical Communication (ECOC)*, 2021.

[146] S. Preußler, G. R. Mehrpoor, and T. Schneider, "Frequency-time coherence for all-optical sampling without optical pulse source," *Scientific reports*, 6, 34500, 2016.

[147] Y. Mandalawi, M. I. Hosni, J. Meier, K. Singh, et al., "Integrated segmented IQ-modulator for orthogonal sampling and multi-level high-bandwidth signal generation," *Optics Letters*, 49(9), 2193–2196, 2024.

[148] Y. Mandalawi, S. De, M. I. Hosni, L. Zhou, et al., "Integrated Wideband Wireless Signal Receiver Based On Cascaded Ring Modulators," in *50th International Conference on Infrared, Millimeter, and Terahertz Waves (IRMMW-THz)*, 2025, accepted.

[149] Y. Mandalawi, J. Meier, M. I. Hosni, K. Singh, et al., "Photonics Assisted Analog-to-Digital Conversion of Wide-Bandwidth Signals by Orthogonal Sampling," in *2023 53rd European Microwave Conference (EuMC)*, pages 464–467, 2023.

[150] Y. Mandalawi, J. Meier, K. Singh, M. I. Hosni, et al., "High-Bandwidth Signal Reception with Improved ENOB by Frequency-Time Coherence Photonics Sampling," in *Optica Advanced Photonics Congress 2022, Technical Digest Series*, Optica Publishing Group, 2022, paper SpTu4J.4.

[151] Y. Mandalawi, M. I. Hosni, J. Meier, S. De, et al., "Integrated Ring Modulator Based High-Speed Optical Sampler for Wireless Signals," in *2025 16th German Microwave Conference (GeMiC)*, pages 37–40, Dresden, Germany, 2025.

[152] Y. Mandalawi, M. I. Hosni, K. Singh, J. Meier, et al., "Segmented Mach-Zehnder Modulator for Orthogonal Sampling Based High Bandwidth THz Transmitters," in *2024 15th German Microwave Conference (GeMiC)*, pages 45–48, 2024.

[153] S. De, J. Meier, Y. Mandalawi, K. Singh, et al., "Comb flatness dependence for orthogonally sampled high bandwidth signals," in *Proceedings of SPIE 12994, Terahertz Photonics III*, vol. 12994, page 1299407, 2024, published 18 June 2024.



https://doi.org/10.7795/110.20260421B

[154] S. De, J. Meier, Y. Mandalawi, R. Das, et al., "Orthogonal Sampling with a Single Photodiode," in *2025 Conference on Lasers and Electro-Optics Europe & European Quantum Electronics Conference (CLEO/Europe-EQEC)*, Munich, Germany, 2025, accepted, to be published.

[155] S. De, Y. Mandalawi, and R. Das, "Error Metrics for Photonics Assisted Signal Processing," in T. Kürner, T. Kleine-Ostmann, T. Schneider, D. Humphreys, et al. (editors), *Metrology for THz Communications - Findings from DFG FOR 2863 Metera-com*, Springer Nature, 2025, published on November 28, 2025. Available at: `https://link.springer.com/book/9783032019851`.

[156] T. Schneider, "Toward terabit receivers for optical and wireless communications," *IEEE Communications Magazine*, 61, 169–174, 2023.

[157] C. Schmidt, H. Yamazaki, G. Raybon, et al., "Data converter interleaving: Current trends and future perspectives," *IEEE Communications Magazine*, 58, 19–25, 2020.

[158] A. Khilo, S. J. Spector, M. E. Grein, et al., "Photonic ADC: Overcoming the Bottleneck of Electronic Jitter," *Optics Express*, 20, 4454, 2012.

[159] R. H. Walden, "Analog-to-digital converter survey and analysis," *IEEE Journal on Selected Areas in Communications*, 17, 539–550, 1999.

[160] "IEEE Standard for Terminology and Test Methods for Analog-to-Digital Converters," 2011, approved 25 March 2011.

[161] Optiwave Systems Inc., *OptiSystem: Optical Communication System Design Software*, Ottawa, Canada, 2024, available at `https://optiwave.com`.

[162] S. Gudyriev, C. Kress, H. Zwickel, J. N. Kemal, et al., "Coherent ePIC Receiver for 64 GBaud QPSK in 0.25 µm Photonic BiCMOS Technology," *Journal of Lightwave Technology*, 37(1), 103–109, 2019.

[163] B. A. Moller, L. Jensen, C. Laurent-Lund, and C. Thirstrup, "Silica-Waveguide Thermo-Optic Phase Shifter With Low Power Consumption and Low Lateral Heat Diffusion," *IEEE Photonics Technology Letters*, 5(12), 1415–1418, 1993.

[164] B. J. Offrein, G. L. Bona, R. Germann, R. Dangel, et al., "Polarization-Independent Thermooptic Phase Shifters in Silicon-Oxynitride Waveguides," *IEEE Photonics Technology Letters*, 16(6), 1483–1485, 2004.

[165] S. Rao, E. D. Mallemace, G. Faggio, M. Iodice, et al., "Experimental characterization of the thermo-optic coefficient vs. temperature for 4H-SiC and GaN semiconductors at the wavelength of 632 nm," *Scientific Reports*, 13, 10205, 2023.

[166] B. Enning, "Electrical Waveguide in Mach–Zehnder Modulator Integrated into Ring Resonator for Optical Signal Processing," *Electronics Letters*, 42(1), 49–65, 2006.



https://doi.org/10.7795/110.20260421B

[167] A. Aimone, G. Fiol, M. Gruner, and M. Schell, "Engineered Transfer Function InP Mach–Zehnder Modulator for Bandwidth Enhancement and Nyquist Shaping," *Journal of Lightwave Technology*, 34(8), 1694–1698, 2016.

[168] C.-T. Lin, J. Chen, S.-P. Dai, P.-C. Peng, et al., "Impact of Nonlinear Transfer Function and Imperfect Splitting Ratio of MZM on Optical Up-Conversion Employing Double Sideband With Carrier Suppression Modulation," *Journal of Lightwave Technology*, 26(15), 2449–2459, 2008.

[169] X. Li, J. Yu, J. Xiao, N. Chi, et al., "W-Band PDM-QPSK Vector Signal Generation by MZM-Based Photonic Frequency Octupling and Precoding," *IEEE Photonics Journal*, 7(4), 1–6, 2015.

[170] Y. B. Ezra, A. Zadok, R. Califa, D. Munk, et al., "All-Optical Wavelet-Based Orthogonal Frequency Division Multiplexing System Based on Silicon Photonic Integrated Components," *IET Optoelectronics*, 10(2), 44–50, 2016.

[171] R. Hamerly, D. Gray, C. Rogers, and K. Jamshidi, "Conditions for Parametric and Free-Carrier Oscillation in Silicon Ring Cavities," *Journal of Lightwave Technology*, 36(19), 4671–4677, 2018.

[172] A. Rostami-Khomami and M. Nikoufard, "Hybrid Plasmonic Ring-Resonator Uni-Traveling Carrier PIN-Photodetector on InGaAsP/InP Layer Stack," *IEEE Transactions on Electron Devices*, 67(8), 3221–3228, 2020.

[173] W. Gao, L. Lu, L. Zhou, and J. Chen, "Automatic Calibration of Silicon Ring-Based Optical Switch Powered by Machine Learning," *Optics Express*, 28, 10438, 2020.

[174] N. A. Riza and S. A. Khan, "Wavelength-Tunable Variable Fiber-Optic Attenuator Using Liquid-Crystal-Mirror Hybrid Controls," *IEEE Photonics Technology Letters*, 17(3), 621–623, 2005.

[175] S. De, R. Das, R. Varshney, and T. Schneider, "Thermal Crosstalk Resilient Integrated Optical Attenuator," in *Frontiers in Optics / Laser Science (FiO/LS)*, OSA Technical Digest, Optica Publishing Group, 2020.

[176] K. Maru, K. Tanaka, T. Chiba, H. Nonen, et al., "Dynamic Gain Equalizer Using Proposed Adjustment Procedure for Thermooptic Phase Shifters Under the Influence of Thermal Crosstalk," *Journal of Lightwave Technology*, 22(6), 1523–1532, 2004.

[177] N. C. Harris, D. Carvalho, M. Pant, C. G. Galataras, et al., "Efficient, Compact and Low Loss Thermo-Optic Phase Shifter in Silicon," *Optics Express*, 22, 10487–10493, 2014.

[178] A. Ribeiro, S. Declercq, U. Khan, M. Wang, et al., "Column-Row Addressing of Thermo-Optic Phase Shifters for Controlling Large Silicon Photonic Circuits," *IEEE Journal of Selected Topics in Quantum Electronics*, 26(5), 1–8, 2020.



https://doi.org/10.7795/110.20260421B

[179] C. T. DeRose, A. L. Starbuck, A. T. Pomerene, J. R. Wendt, et al., "Thermal Crosstalk Limits for Silicon Photonic DWDM Interconnects," in *Proceedings of the Optical Interconnects Conference (OI)*, pages 125–126, 2014.

[180] M. Milanizadeh, D. Aguiar, F. Morichetti, and A. Melloni, "Automatic Configuration and Wavelength Locking of Coupled Micro-Ring Resonators in Presence of Thermal Cross-Talk," in *Proceedings of the 20th International Conference on Transparent Optical Networks (ICTON)*, pages 1–4, 2018.

[181] M. Milanizadeh, D. Aguiar, A. Melloni, and F. Morichetti, "Control and Calibration Recipes for Photonic Integrated Circuits," *IEEE Journal of Selected Topics in Quantum Electronics*, 26(5), 1–10, 2020.

[182] M. Jacques, A. Samani, E. El-Fiky, D. Patel, et al., "Optimization of Thermo-Optic Phase-Shifter Design and Mitigation of Thermal Crosstalk on the SOI Platform," *Optics Express*, 27, 10456–10471, 2019.

[183] S. De, Y. Mandalawi, A. Venugopalan, J. Meier, et al., "Experimental Study of Thermal Crosstalk Alleviation in Thermo-Optic Phase Shifters," in *Kleineheubacher Tagung 2025*, 2025, accepted for presentation.

[184] S. De, R. Das, T. Kleine-Ostmann, and T. Schneider, "Athermal Travelling Wave Mach-Zehnder Modulators for Optical Interconnects," in B. Yang, F. Leo, A. Tauke-Pedretti, S. Arafin, et al. (editors), *OSA Advanced Photonics Congress 2021, OSA Technical Digest*, Optica Publishing Group, 2021, paper NeF1B.4.

[185] S. De, R. Das, T. Kleine-Ostmann, and T. Schneider, "Effect of Thermal Crosstalk on Travelling-wave Mach-Zehnder Modulator," in *2021 Conference on Lasers and Electro-Optics Europe & European Quantum Electronics Conference (CLEO/Europe-EQEC)*, pages 1–1, 2021.

[186] S. De, R. Das, K. Singh, Y. Mandalawi, et al., "Thermal Crosstalk Mitigation in a Dual-Drive Mach-Zehnder Modulator," in *2022 International Conference on Numerical Simulation of Optoelectronic Devices (NUSOD)*, pages 27–28, 2022.

[187] S. De, R. Das, K. Singh, Y. Mandalawi, et al., "Thermal Insulation of Silicon Ring Modulators in Densely-Packed Photonic Integrated Circuits," in *Proc. SPIE 12575, Integrated Optics: Design, Devices, Systems and Applications VII*, page 125750C, 2023.

[188] S. De, R. Das, K. Singh, Y. Mandalawi, et al., "Thermal-aware Multi-Quantum Well Laser," in *Frontiers in Optics + Laser Science 2022 (FIO, LS), Technical Digest Series*, Optica Publishing Group, 2022, paper JTu4A.51.

[189] S. De, R. Das, K. Singh, Y. Mandalawi, et al., "Study of Thermal Crosstalk in Avalanche Photodetectors in THz Domain," in *2022 47th International Conference on Infrared, Millimeter and Terahertz Waves (IRMMW-THz)*, pages 1–2, 2022.



https://doi.org/10.7795/110.20260421B

[190] S. De, R. Das, K. Singh, Y. Mandalawi, et al., "Temperature Insensitive Avalanche Photodetectors," in *Optica Advanced Photonics Congress 2022, Technical Digest Series*, Optica Publishing Group, 2022, paper ITu3C.2.

[191] S. De, R. Das, K. Singh, Y. Mandalawi, et al., "Crosstalk Resistant Integrated Uni-Traveling Carrier Photodetector," in *2023 48th International Conference on Infrared, Millimeter, and Terahertz Waves (IRMMW-THz)*, pages 1–2, 2023.

[192] R. C. Heim, S. De, R. Das, K. Singh, et al., "Thermal Crosstalk Alleviated Silicon Microring Switches," in *Conference on Lasers and Electro-Optics/Europe (CLEO/Europe 2023) and European Quantum Electronics Conference (EQEC 2023), Technical Digest Series*, Optica Publishing Group, 2023, paper ck_p_15.

[193] S. De, R. Das, K. Singh, Y. Mandalawi, et al., "Amorphous Silicon Based Crosstalk Resilient Photonic Phase Shifters," in *2023 Conference on Lasers and Electro-Optics Europe European Quantum Electronics Conference (CLEO/Europe-EQEC)*, pages 1–1, 2023.

[194] S. De, R. Das, K. Singh, Y. Mandalawi, et al., "Crosstalk Immune High-Speed Photonic Transmitter-Receiver System," in *2024 15th German Microwave Conference (GeMiC)*, pages 25–28, 2024.

[195] K. Singh, R. Das, A. Venugopalan, S. De, et al., "Real-time reconfigurable on-chip photonic frequency decoder," *Optics Express*, 31(19), 30160–30170, 2023.

[196] K. Singh, R. Das, A. Misra, S. De, et al., "Reconfigurable RF Frequency Sniffer Using Tunable Micro Ring Resonator," in *CLEO 2023, Technical Digest Series*, Optica Publishing Group, 2023, paper SW3O.5.

[197] R. Das, S. De, and T. Schneider, "On-chip Inductive Peaking to Boost the Silicon Modulator Bandwidth," in B. Yang, F. Leo, A. Tauke-Pedretti, S. Arafin, et al. (editors), *OSA Advanced Photonics Congress 2021, Technical Digest*, Optica Publishing Group, 2021, paper NeF1B.2.

[198] C. Qiu, Y. Wang, Y. Chen, Y. Lei, et al., "Design and analysis of a novel graphene-assisted silica/polymer hybrid waveguide with thermal–optical phase modulation structure," *IEEE Photonics Journal*, 11(2), 2019.

[199] S. Zhu, T. Hu, Z. Xu, Y. Dong, et al., "An improved thermo-optic phase shifter with AlN block for silicon photonics," in *Proceedings of the Optical Fiber Communication Conference (OFC)*, pages 1–3, San Diego, CA, USA, 2019.

[200] P. Pintus, M. Hofbauer, and C. L. Manganelli, "PWM-driven thermally tunable silicon microring resonators: Design, fabrication, and characterization," *Laser & Photonics Reviews*, 13(9), 2019.



https://doi.org/10.7795/110.20260421B

[201] M. R. Watts, W. A. Zortman, D. C. Trotter, G. N. Nielson, et al., "Adiabatic resonant microrings (ARMs) with directly integrated thermal microphotonics," in *Proceedings of the Conference on Lasers and Electro-Optics/International Quantum Electronics Conference (CLEO/IQEC)*, Baltimore, MD, USA, 2011, check exact page numbers and publication details if available.

[202] A. Masood, M. Pantouvaki, G. Lepage, P. Verheyen, et al., "Comparison of heater architectures for thermal control of silicon photonic circuits," in *Proceedings of the 10th International Conference on Group IV Photonics (GFP)*, pages 83–84, IEEE, Seoul, South Korea, 2013.

[203] L. Vivien, S. Laval, D. Pascal, E. Cassan, et al., "Comparison Between Strip and Rib SOI Microwaveguides for Intra-Chip Light Distribution," *Optical Materials*, 27, 756–762, 2005.

[204] X. Qi and R. W. Dutton, "Interconnect Parasitic Extraction of Resistance, Capacitance, and Inductance," in J. A. Davis and J. D. Meindl (editors), *Interconnect Technology and Design for Gigascale Integration*, pages 67–109, Springer, Boston, MA, 2003.

[205] R. R. Tummala, E. J. Rymaszewski, and A. G. Klopfenstein (editors), *Microelectronics Packaging Handbook: Semiconductor Packaging*, Springer, New York, NY, 2 ed., 1997, originally published by Chapman & Hall, 1997.

[206] Keysight Technologies, *Advanced Design System (ADS)*, Santa Rosa, CA, USA, 2020, version 2020.

[207] G. T. Reed, D. J. Thomson, F. Y. Gardes, Y. Hu, et al., "High-speed carrier-depletion silicon Mach—Zehnder optical modulators with lateral PN junctions," *Frontiers in Physics*, 2(77), 2014.

[208] Z. Yong, H. Yun, S. Ristic, J. Bovington, et al., "U-shaped PN junctions for efficient silicon Mach—Zehnder and microring modulators in the O-band," *Optics Express*, 25(7), 8425–8439, 2017.

[209] Y. Long, L. Zhou, and J. Wang, "Photonic-assisted microwave signal multiplication and modulation using a silicon Mach–Zehnder modulator," *Scientific Reports*, 6, 20215, 2016.

[210] R. A. de Paula Jr., I. Aldaya, T. Sutili, R. C. Figueiredo, et al., "Design of a silicon Mach-Zehnder modulator via deep learning and evolutionary algorithms," *Scientific Reports*, 13(14662), 2023, open access.

[211] S. M. Sze and K. K. Ng, *Physics of Semiconductor Devices*, Wiley, Hoboken, NJ, USA, 3rd ed., 2006.

[212] S. Akiyama, T. Kato, Y. Enya, M. Ida, et al., "InP-Based Mach–Zehnder Modulator With Capacitively Loaded Traveling-Wave Electrodes," *Journal of Lightwave Technology*, 26(6), 608–615, 2008.



https://doi.org/10.7795/110.20260421B

[213] H. Xu, X. Xiao, X. Li, Y. Hu, et al., "High speed silicon Mach-Zehnder modulator based on interleaved PN junctions," *Optics Express*, 20(13), 15093–15099, 2012.

[214] M. I. Hosni, K. Singh, S. Dev, A. Zarif, et al., "Low Power, Compact Integrated Photonic Sampler Based on a Silicon Ring Modulator," *IEEE Photonics Journal*, 14(4), 1–6, 2022.

[215] M. Bahadori, M. Nikdast, S. Rumley, L. Y. Dai, et al., "Design Space Exploration of Microring Resonators in Silicon Photonic Interconnects: Impact of the Ring Curvature," *Journal of Lightwave Technology*, 36(13), 2767–2782, 2018.

[216] Y. Sun, K. Zhou, Q. Sun, et al., "Room-temperature continuous-wave electrically injected InGaN-based laser directly grown on Si," *Nature Photonics*, 10, 595–599, 2016.

[217] T. Komljenovic et al., "Heterogeneous Silicon Photonic Integrated Circuits," *Journal of Lightwave Technology*, 34(1), 20–35, 2016.

[218] B. R. Koch et al., "Integrated Silicon Photonic Laser Sources for Telecom and Datacom," in *2013 Optical Fiber Communication Conference and Exposition and the National Fiber Optic Engineers Conference (OFC/NFOEC)*, pages 1–3, 2013.

[219] J. E. Bowers, "Laser integration on silicon for photonic integrated circuits," in *Proc. SPIE PC12004, Integrated Optics: Devices, Materials, and Technologies XXVI*, page PC1200402, 2022.

[220] J. Piprek, J. K. White, and A. J. SpringThorpe, "What limits the maximum output power of long-wavelength AlGaInAs/InP laser diodes?" *IEEE Journal of Quantum Electronics*, 38(9), 1253–1259, 2002.

[221] Z. Huang, Y. Kang, M. Morse, M. Lu, et al., "25 Gbps low-voltage waveguide Si–Ge avalanche photodiode," *Optica*, 3(7), 793–798, 2016.

[222] B. Wang and J. Mu, "High-speed Si-Ge avalanche photodiodes," *PhotoniX*, 3, 8, 2022.

[223] H. T. J. Meier, *Design, Characterization and Simulation of Avalanche Photodiodes*, Ph.d. dissertation, ETH Zurich, 2011.

[224] A. Beling, A. S. Cross, M. Piels, J. Peters, et al., "InP-based waveguide photodiodes heterogeneously integrated on silicon-on-insulator for photonic microwave generation," *Optics Express*, 21(22), 25901–25906, 2013.

[225] S. Jia et al., "Integrated dual-laser photonic chip for high-purity carrier generation enabling ultrafast terahertz wireless communications," *Nature Communications*, 13, 1388, 2022.

[226] T. Ishibashi and H. Ito, "Uni-traveling-carrier photodiodes," *Journal of Applied Physics*, 127, 031101, 2020.

[227] A. Beling et al., "InP-based waveguide photodiodes heterogeneously integrated on silicon-on-insulator for photonic microwave generation," *Optics Express*, 21, 25901, 2013.



https://doi.org/10.7795/110.20260421B

[228] F. Yu, K. Sun, Q. Yu, and A. Beling, "High-Speed Evanescently-Coupled Waveguide Type-II MUTC Photodiodes for Zero-Bias Operation," *Journal of Lightwave Technology*, 38(24), 6827–6832, 2020.

[229] D. Maes, "High-speed uni-traveling-carrier photodiodes on silicon nitride," *APL Photonics*, 8, 016104, 2023.

[230] Y. Yuan, Y. Peng, W. V. Sorin, S. Cheung, et al., "A 5 × 200 Gbps microring modulator silicon chip empowered by two-segment Z-shape junctions," *Nature Communications*, 15(918), 2024, open access, Published: 31 January 2024.

[231] W. Bogaerts, P. De Heyn, T. Van Vaerenbergh, K. De Vos, et al., "Silicon microring resonators," *Laser & Photonics Reviews*, 6(1), 47–73, 2012.

[232] N. Sherwood-Droz, H. Wang, L. Chen, B. G. Lee, et al., "Optical 4×4 hitless silicon router for optical Networks-on-Chip (NoC)," *Optics Express*, 16(20), 15915–15922, 2008.

[233] R. C. Heim, "Simulation Study of Thermal Switch using Thermally Active Ring Resonators," 2023, bachelor's thesis, supervised by S. De and K. Singh.

[234] E. Hemsley, D. Bonneau, J. Pelc, R. Beausoleil, et al., "Photon pair generation in hydrogenated amorphous silicon microring resonators," *Scientific Reports*, 6, 38908, 2016.

[235] T. Kuwahara, H. Ito, K. Kawaguchi, Y. Higuchi, et al., "The reason why thin-film silicon grows layer by layer in plasma-enhanced chemical vapor deposition," *Scientific Reports*, 5, 9052, 2015.



https://doi.org/10.7795/110.20260421B

Bundesministerium
für Wirtschaft
und Energie

Die Physikalisch-Technische Bundesanstalt, das nationale Metrologieinstitut, ist eine wissenschaftlich-technische Bundesoberbehörde im Geschäftsbereich des Bundesministeriums für Wirtschaft und Energie.

PTB

Physikalisch-Technische Bundesanstalt
Nationales Metrologieinstitut
ISNI: 0000 0001 2186 1887

Bundesallee 100
38116 Braunschweig

**Presse- und Öffentlichkeitsarbeit**

Telefon: (0531) 592-93 21
Fax: (0531) 592-30 08
E-Mail: presse@ptb.de
www.ptb.de